SCATTERING FROM A COLLECTION OF PERIODIC LINEAR ARRAYS OF ARBITRARILY SHAPED THIN WIRE ELEMENTS EMPHASIZING TRUNCATION EFFECTS OF PLANAR PERIODIC SURFACES

by

Joseph M. Usoff, B.S.E.E., M.S.E.E.
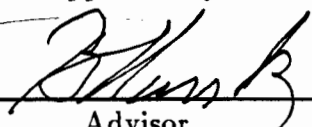
* * * * *

The Ohio State University

1993

Dissertation Committee:

Prof. B. A. Munk

Prof. E. H. Newman

Prof. L. Peters, Jr.

Approved by:

Advisor
Department of Electrical
Engineering

DEDICATION

To my wife Cathy, and my daughter Rebecca.

ACKNOWLEDGEMENTS

I'd like to express my sincerest thanks and deepest appreciation

to all who have helped toward my graduation.

I have learned from so many along the way,

my heart goes out to you all today.

Many thanks to Lyn Snedden whose help in preparation

saved me from a great deal of aggravation.

To those vigilent and dauntless dissertation readers,

I thank Edward Newman and Leon Peters.

My thanks and my love to my father and mother,

you made me who I am more than any other.

To my beautiful daughter and my truly wonderful wife,

I thank you for enriching, fulfilling and sharing my life.

And last to Ben Munk, my advisor, my mentor, my friend,

I hope that our paths cross many times again.

Your insight, invaluable, your counsel, sage,

may you always prosper and every year be vintage.

VITA

March 1, 1960 .... Born in Franklin, PA

June 1982 .... B.S.E.E.,
Carnegie Mellon University,
Pittsburgh, PA

July 1982 – August 1984 .... Engineer, Raytheon Equipment Division
Wayland, Massachusetts

September 1984 – September 1986 ..... Research Associate,
ElectroScience Laboratory,
The Ohio State University,
Columbus, Ohio

September 1986 – June 1989 .... Senior Data Engineer
Dyncorp, Radar Backscatter Division
Alamogordo, NM

July 1989 – present .... Research Associate,
ElectroScience Laboratory,
The Ohio State University,
Columbus, Ohio

PUBLICATIONS

"Phased Array Simulator Measurements of Microstrip Patch Radiators," J.D. Hanfling and J.M. Usoff, IEEE Antennas and Propagation Society Int. Symp. Dig., May 1983, Vol. 1, pp. 178–181.

"Plane Wave Reflection from Microstrip-Patch Arrays — Theory and Experiment," C.C. Lin, J. Schmoys, A. Hessel, J.D. Hanfling and J.M. Usoff, IEEE Trans. on Antennas and Propagation, Vol. AP-33, No. 4, April 1985, pp. 426–435.

"Three Frequency Dichroic Surface for Loral," B. Munk, J. Usoff and S. Schneider, Technical Report 726888-1, ElectroScience Laboratory, The Ohio State University generated under contract AG3001585 for Space Systems/Loral, Palo Alto, CA, March 1993.

FIELDS OF STUDY

Major Field: Electrical Engineering

Electromagnetic Theory .... R. G. Kouyoumjian

Antennas .... R. C. Rudduck
                                     B. A. Munk

Physical Electronics .... F. S. Khan

Communications .... R. T. Compton, Jr.
                                     D. T. Davis

Applied Mathematics .... U. H. Gerlach
                                     J. T. Scheik

TABLE OF CONTENTS

LIST OF FIGURES

CHAPTER I

Introduction

1.1 Problem Statement

The scattering from structures that are infinite and periodic along a single linear axis will be studied. The number and position of the linear arrays is arbitrary and the coupling between arrays is calculated rigorously. The basic building block is a thin wire V-dipole element as shown in Figure 1. This element was chosen since a wide variety of scatterers can be constructed from it without being restricted to being planar or of a particular orientation. To keep the basic element general, the effects of unequal leg length, arbitrary orientation, overlap, lumped loads, finite conductivity, and thin dielectric coatings have been included.

The solution is implemented using the moment method with piecewise sinusoidal basis and testing functions. Self and mutual impedances are defined and found for infinite periodic linear arrays of elements. The resulting general Ohmic equation is solved for the current coefficients and the fields at a large radial distance from the array axis are found for the total configuration and any partial subsets that are of interest.

1.2 Background

What is presented herein is a part of an ongoing progression of work undertaken at The Ohio State University ElectroScience Laboratory studying electromagnetic

1
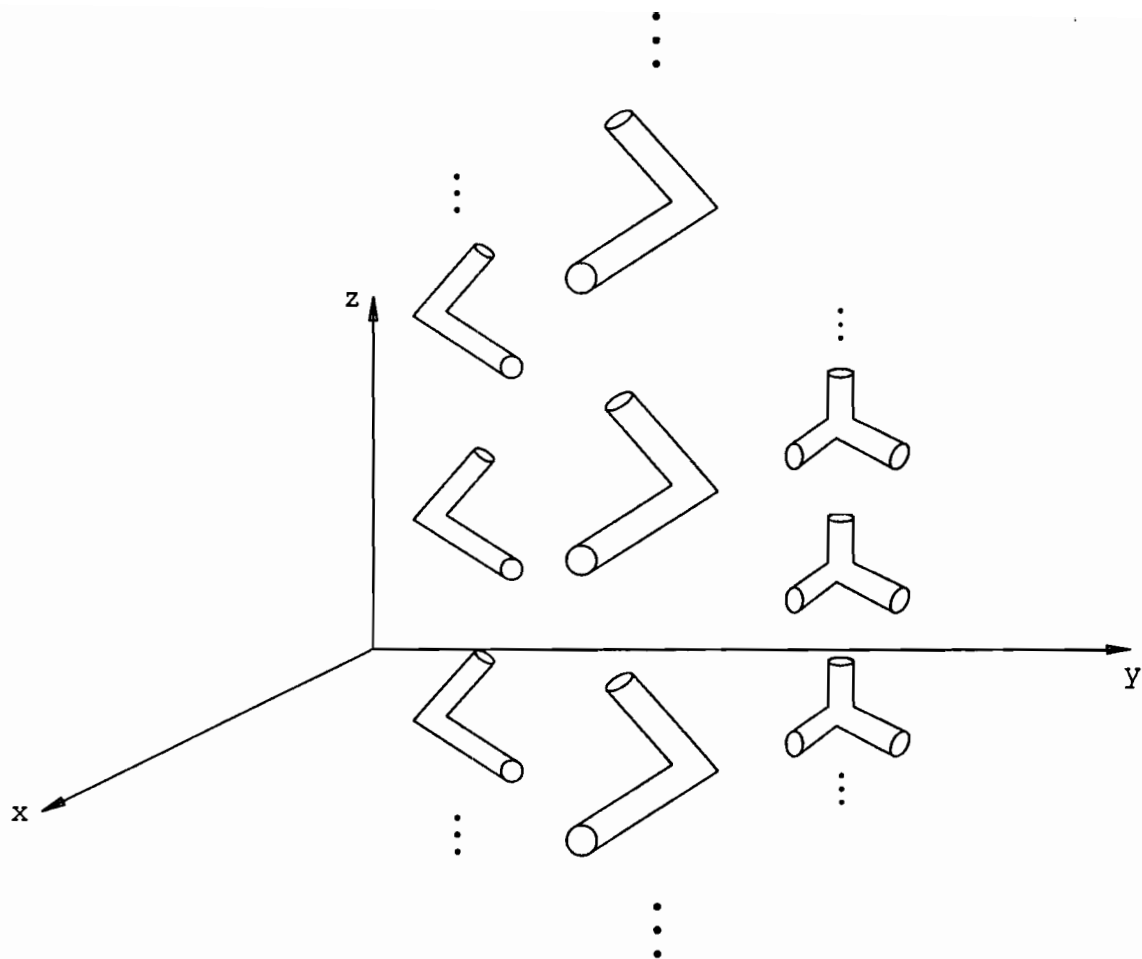
Figure 1: Fundamental elements with arbitrary orientation. Each dipole consists of two segments, each of which has variable parameters of wire radius, wire length, wire conductivity, lumped loads at the ends of the segment and a dielectric coating. Various elements may overlap or be separated as shown above.

2

scattering and radiation from periodic structures. There has been a continuous evolution in the depth and breadth of the analytical capabilities resulting in a steadily improving understanding of the physical mechanics of the workings of periodic structures. Earlier work in this lineage started with infinite planar arrays of dipoles or slots [1, 2], then added multiple layers [3, 4, 5] and included dielectric slabs [6, 7, 8]. This work on planar elements culminated in the development of an eminently useful computer code called PMM [9, 10] which is capable of handling most planar design problems.

More recently the focus has been on periodic infinite linear arrays, which is a natural progression, as they can be utilized to study the effects of truncating or curving planar arrays. By using the PMM program, a broad spectrum of planar structures can be modeled, but finite arrays, curved arrays and nonparallel planar arrays have not been included. It is also a progression that parallels the development of more powerful, more readily available, computing platforms since the analysis of a multitude of columns of elements is much more computer intensive than analyzing an infinite planar structure.

Hughes [11] studied the scattering from straight dipoles parallel to the array axis. He was also the originator of a computer program [12] which has seen extensive use in modeling a variety of truncated, multilayer planar structures and singly curved structures. Simon [13] studied dipole arrays conformal to an infinitely long dielectric-clad PEC circular cylinder allowing for the dipoles to be oriented along a helical arc. Strickler [14] used the Hughes code to study the variation in impedance across a finite by infinite antenna array backed by a groundplane, emphasizing practical design ideas. Most recently, Skinner [15] studied scattering from arrays of dipoles transverse to the array axis. Skinner also considered axial linear slot arrays in infinite groundplanes in order to model the interaction between antenna arrays and radomes.

3

This is not to say that work on periodic surfaces is not being done elsewhere. Mittra [16, 17] provides an overview of various analysis techniques used on frequency selective surfaces and includes an extensive bibliography. There has also been a recent paper by Cwik [18] dealing directly with truncation and curvature concerns, but the analysis is limited in that it only includes infinite PEC strips.

Hughes [11] handled axially oriented straight dipoles and Skinner [15] analyzed transversely oriented straight dipoles. There are certain applications which use these types of elements, but in general, it would be an improvement if a more practical building block were provided. An arbitrarily oriented, independent leg length, V-dipole is such an element. It can be used to build a wire model of a very wide diversity of scattering targets. It can be used to model planar elements as PMM [10] does, non-planar elements such as those analyzed by English [19] and Lin [20] or even new classes of three-dimensional elements. Such generalization has a price of greater computational demands, but it is a price that must be paid to model more elaborate elements than limited orientation straight dipoles.

1.3 Organization

The main body of the dissertation is broken into four chapters. The first chapter lays out the theory of the analytical techniques to be used. It focuses on concerns specific to V-dipoles and infinite periodic linear arrays of V-dipoles. More general concepts have been relegated to appendices for those readers who are interested in the development of the equations provided.

The next three chapters explore the implications of the theory presented by providing examples and comparative studies. The first of these starts with the simplest cases of a single infinite column of elements. Four different element types

4

are given, the element and array parameters are varied, and the results are presented, highlighting the implications of each variation.

The next chapter focuses on truncated planar frequency selective surfaces. Such surfaces are currently seeing extensive use and are a primary application of periodic surfaces. A comparison is made between modeling such surfaces rigorously using the theory provided here, a simple diffraction model, physical optics and an infinite array approximation which is analogous to periodic physical optics.

A sample design approach is given in the next chapter. The design is centered on a truncated planar surface where the goal is to minimize the backscattered field at a given frequency and angle of incidence. This example provides a problem where the truncation effects have become the primary concern and highlights the effects of varying the element parameters on an overall design.

The main body is followed by a conclusions chapter which summarizes the previous chapters, then provides some ideas for possible future directions.

CHAPTER II

Theory

The analytical approach taken for the problem at hand is rooted in previous work done by Richmond [21] and Munk [8, 7]. Richmond used a V-dipole element as a building block to construct thin wire models of antennas and a wide variety of scatterers including wire frame models of some large elaborate targets. His approach to modeling the wire scatterers and the approximations made along the way have been fully embraced here. In fact, some of the core subroutines used in finding the self and mutual impedances between elements have been taken directly from Richmond's thin wire code [22].

Munk showed that it can be very advantageous to transform the spatial coordinates to a spectral domain when dealing with periodic structures. This approach has at its heart a principle found in Huygen's *Treatise on Light* [23] which was written in 1661! Huygens correctly postulated that light is a wave and of more relevance here, that a multitude of sources emitting spherical waves, each of which may be "infinitely feeble", can generate strong "principal" waves in specific directions. It can be much easier and much more efficient to work with the resultant "principal" waves than to analyze each "infinitely feeble" one. Also, the periodicity allows the invocation of Floquet's theorem [24] whereby the characteristics of a single element of an infinite array of identical elements will be the same as all others elements in the array with only a linear phase variation.

An infinitely long column of scatterers lies somewhere in the middle ground between analyzing each element individually in the spatial domain as Richmond does and analyzing a single element of a two dimensionally infinite array in the spectral domain as Munk does. For plane wave incidence, Floquet currents can be assumed along the infinite dimension and it has been found that it is advantageous to use a mixture of spatial domain analysis and spectral domain analysis to find the scattered fields.

The analysis is initiated utilizing Schelkunoff equivalent currents [25] and Rumsey's reaction concept [26]. Appendix A shows how these two concepts are combined to generate an integral equation. This integral equation can now be applied to the geometry of interest which in this case is a thin wire. The thin wire is chosen since it is a very practical building block to construct models out of and also since it allows for making approximations that simplify the analysis enormously, yielding tractable computations. A brief outline of the thin wire approximation is given in Appendix B. For those requiring more detailed information, Richmond [21] and the course notes by Newman [27] (which unfortunately have not been published as a text) are both excellent sources. Also, additional details specific to V-dipoles will be presented in the next section.

As a final introductory note, the geometry of an array of V-dipoles was presented in the introduction in Figure 1. It is important that hereafter, a coordinate system be defined and consistently adhered to, to obviate any unnecessary careless errors. The coordinate system chosen is presented in Appendix C for ease of reference in the following sections.

2.1 Mutual Impedance for Single Elements

First, consider finding the scattered fields from a single V-dipole. The V-dipole is constructed of two monopoles which may be of different length and of different orientation. It is assumed to meet all of the thin wire approximation criteria given in Appendix B. Such an element is shown at the top of Figure 2. Schelkunoff's equivalent current principle is now applied as shown in the middle of Figure 2. A null field exists in the center of the elements and the elements have been replaced with their equivalent currents on the surface and the ambient medium in the interior. A test filament of current is now placed on the axis of one of the legs as shown at the bottom of Figure 2. There are now four different sources involved: 1) the incident field source, 2) the surface currents on leg a, 3) the surface currents on leg b, and 4) the test filament. The first three sources will be lumped together and considered one source and its reaction with the test source will be found.

$$
\begin{aligned}
\langle i + a + b, t \rangle &= \langle i, t \rangle + \langle a, t \rangle + \langle b, t \rangle \\
&= \int_0^A \overline{E}^i \cdot \overline{I}^t \, dl + \int_0^A \overline{E}^a \cdot \overline{I}^t dl + \int_0^A \overline{E}^b \cdot \overline{I}^t dl \\
&= \int_0^A \left(\overline{E}^i + \overline{E}^a + \overline{E}^b \right) \cdot \overline{I}^t dl \\
&= 0
\end{aligned}
\tag{2.1}
$$

This result is zero since the total field, $\overline{E}^i + \overline{E}^a + \overline{E}^b$, is zero interior to the elements. Now rearranging the above and applying reciprocity results in:

$$
-\langle t, a \rangle - \langle t, b \rangle = \langle i, t \rangle \tag{2.2}
$$

$$
-\int_{S_a} \left(\overline{E}^{ta} \cdot \overline{J}^s_a - \overline{H}^{ta} \cdot \overline{M}^s_a \right) ds - \int_{S_b} \left(\overline{E}^{ta} \cdot \overline{J}^s_b - \overline{H}^{ta} \cdot \overline{M}^s_b \right) ds = \int_0^A \overline{E}^i \cdot \overline{I}^{ta} dl \tag{2.3}
$$

8
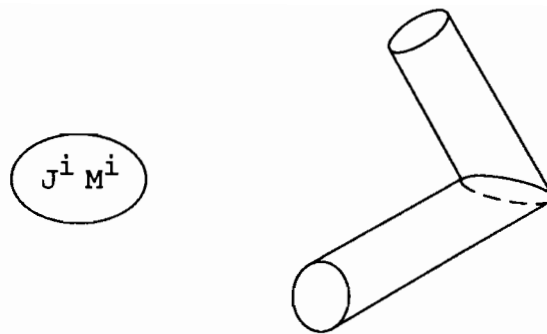
Original Problem
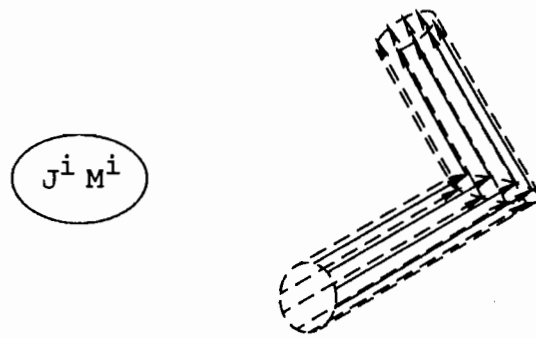
Equivalent Currents
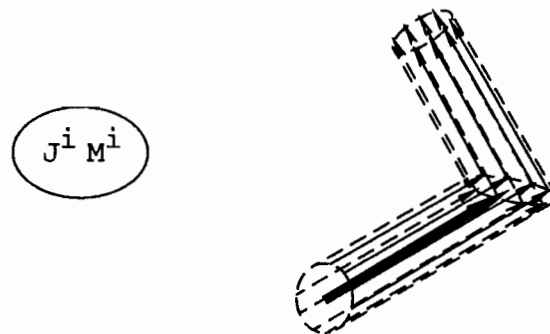
Equiv. Currents + Test Filament

Figure 2: Equivalent currents and test filament for a V-dipole.

The thin wire approximations are now applied yielding:

$$-\int_0^{L_a} I_a(l)\left[E_l^{ta} - Z_{sa}H_\phi^{ta}\right]dl - \int_0^{L_b} I_b(l)\left[E_l^{ta} - Z_{sb}H_\phi^{ta}\right]dl = \int_0^A \overline{E}^i \cdot \overline{I}^{ta}dl \quad (2.4)$$

where

$$\overline{E}^{ta}, \overline{H}^{ta} \;\; = \;\; \text{fields from test filament } a \quad\quad (2.5)$$

The definitions of all of the variables in this equation are identical to those given in Appendix B. This process is repeated by placing a test filament on the axis of leg b, yielding:

$$-\int_0^{L_a} I_a(l)\left[E_l^{tb} - Z_{sa}H_\phi^{tb}\right]dl - \int_0^{L_b} I_b(l)\left[E_l^{tb} - Z_{sb}H_\phi^{tb}\right]dl = \int_0^B \overline{E}^i \cdot \overline{I}^{tb}dl \quad (2.6)$$

where

$$\overline{E}^{tb}, \overline{H}^{tb} \;\; = \;\; \text{fields from test filament } b \quad\quad (2.7)$$

The current must be continuous where the monopoles meet, implying:

$$I_a(0) \;\; = \;\; I_b(0) = I(0) \quad\quad (2.8)$$

$$I^{ta}(0) \;\; = \;\; I^{tb}(0) = I^t(0) \quad\quad (2.9)$$

Combining the above results yields:

$$I(0)\left\{-\int_0^{L_a} \frac{I_a(l)}{I(0)}\left[E_l^{ta} - Z_{sa}H_\phi^{ta}\right]dl - \int_0^{L_b} \frac{I_b(l)}{I(0)}\left[E_l^{ta} - Z_{sb}H_\phi^{ta}\right]dl \right.$$

$$\left. -\int_0^{L_a} \frac{I_a(l)}{I(0)}\left[E_l^{tb} - Z_{sa}H_\phi^{tb}\right]dl - \int_0^{L_b} \frac{I_b(l)}{I(0)}\left[E_l^{tb} - Z_{sb}H_\phi^{tb}\right]dl \right\}$$

$$= \int_0^A \overline{E}^i \cdot \overline{I}^{ta}dl + \int_0^B \overline{E}^i \cdot \overline{I}^{tb}dl \quad\quad (2.10)$$

10

A linear $\hat{p}$-directed wire antenna that has a current $I^t(l)$ under transmitting conditions will, upon exposure to an electric field, observe an induced voltage at its terminals given by [28]:

$$V = \frac{1}{I^t(\bar{R}_0)} \int\limits_{element} \bar{E} \cdot \hat{p} I^t(l) dl \qquad (2.11)$$

where

$$\bar{R}_0 = \text{position of the element terminals} \qquad (2.12)$$

Now Equation (2.10) can be written as:

$$I Z_{11} = V \qquad (2.13)$$

where

$$I = I(0) \qquad (2.14)$$

$$Z_{11} = \frac{1}{I^t(0)} \left\{ -\int\limits_0^{L_a} \frac{I_a(l)}{I(0)} \left[E_l^t - Z_{sa} H_\phi^t \right] dl - \int\limits_0^{L_b} \frac{I_b(l)}{I(0)} \left[E_l^t - Z_{sb} H_\phi^t \right] dl \right\} \qquad (2.15)$$

$$V = \int\limits_0^A \overline{E}^i \cdot \frac{\overline{I}^{ta}(l)}{I^t(0)} dl + \int\limits_0^B \overline{E}^i \cdot \frac{\overline{I}^{tb}(l)}{I^t(0)} dl \qquad (2.16)$$

$$E_l^t = E_l^{ta} + E_l^{tb} \qquad (2.17)$$

$$H_\phi^t = H_\phi^{ta} + H_\phi^{tb} \qquad (2.18)$$

The units of the above are as one would expect, I in amps, Z_{11} in ohms and V in volts. The self impedance of a single V-dipole is defined by Z_{11}. The current is found simply by

$$I = V/Z_{11} \qquad (2.19)$$

which is then used to find the scattered fields.

The next step in solving for the current is to choose a current distribution for the test filament and for the surface currents. The current distribution of choice will be the piecewise sinusoid as shown in Figure 3. The justification for this choice was stated clearly and succinctly by Richmond [21]. "The sinusoidal dipole is probably the only finite line source with simple closed-form expressions for the near zone fields. Furthermore, the mutual impedance between two sinusoidal dipoles is available in terms of exponential integrals, and the piecewise-sinusoidal function is evidently close to the natural current distribution on a perfectly conducting thin wire." Appendix D gives the formulas for the near zone fields of a sinusoidal filament. This appendix is taken directly from Richmond and is repeated here for completeness due to its significance. (It should be noted that the origin of this choice of basis function actually predates Richmond significantly. Pocklington [29] first discovered the sinusoidal nature of the current on a wire. Schelkunoff [28, 30] delved deeply into the origin and nature of the currents on antennas and used a piecewise sinusoid current distribution in his analysis of filamentary wire antennas.)

It is convenient to define a normalized basis function $\overline{F}(l)$ that matches the distribution shown in Figure 3 as:

$$\overline{F}(l) = \begin{cases} \hat{p}(a) \frac{\sin \beta(A-l)}{\sin \beta A}, & 0 \leq l \leq A \\ \hat{p}(b) \frac{\sin \beta(\beta-l)}{\sin \beta B}, & 0 \leq l \leq B \end{cases} \qquad (2.20)$$

Using this current distribution the self impedance and induced voltage can be written more compactly as:

$$Z_{11} = -\frac{1}{I^t(0)} \int_{element} F(l) \left[E_l^t - Z_s H_\phi^t \right] dl$$

$$V = \int_{filament} \overline{E}^i \cdot \overline{F}(l) dl \qquad (2.21)$$

where it is implied that Z_{11} actually consists of four separate integrals as in Equation (2.10) and V actually consists of two separate integrals along each leg.
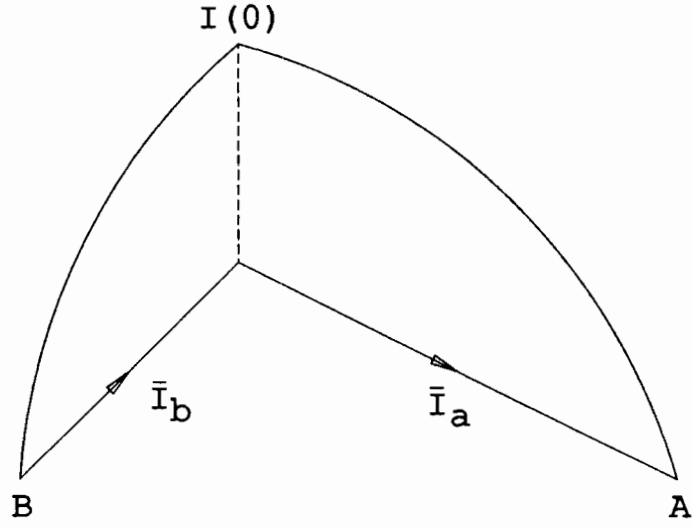
$$\bar{I}_a(l) = \hat{p}^{(a)} I(0) \frac{\sin \beta(A-l)}{\sin \beta A} \quad , \quad 0 \le l \le A$$

$$\bar{I}_b(l) = \hat{p}^{(b)} I(0) \frac{\sin \beta(B-l)}{\sin \beta B} \quad , \quad 0 \le l \le B$$

— or —

$$\bar{I}_a(l) = \hat{p}^{(a)} I(0) \frac{\cos \beta l - \cos \beta A}{1 - \cos \beta A} \quad , \quad 0 \le l \le A$$

$$\bar{I}_b(l) = \hat{p}^{(b)} I(0) \frac{\cos \beta l - \cos \beta B}{1 - \cos \beta B} \quad , \quad 0 \le l \le B$$

Figure 3: Current for a bent mode.

13
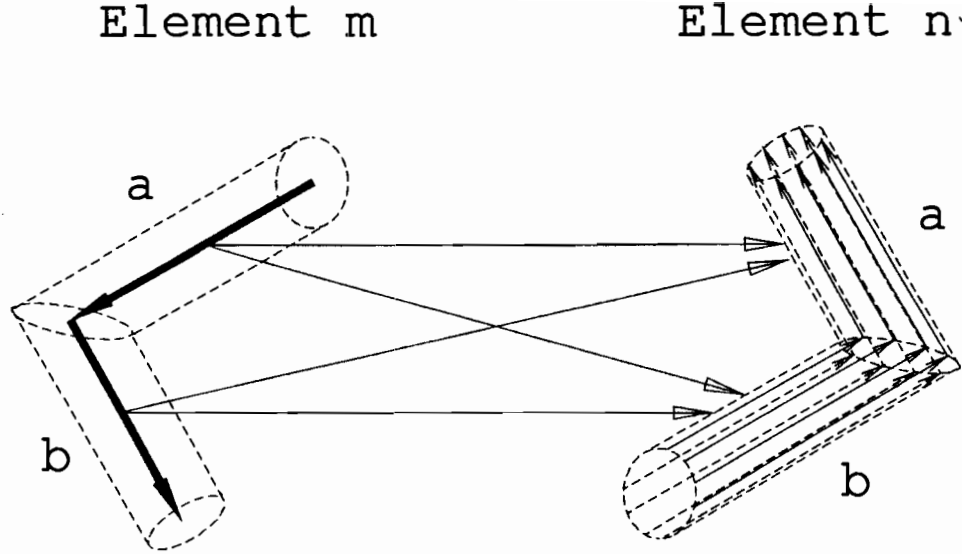
Element m   Element n

Figure 4: The mutual impedance between elements m and n consists of four terms, filament a to surface a + filament a to surface b + filament b to surface a + filament b to surface b.

A mutual impedance between two dipoles can now be similarly defined as:

$$Z_{mn} = -\frac{1}{I^{tm}(0)} \int\limits_{element\ n} F_n(l) \left[E_l^{tm} - Z_s H_\phi^{tm} \right] dl \qquad (2.22)$$

where it is also implied that Z_{mn} actually consists of four separate integrals as shown in Figure 4.

The integral over the surface is not usually completed in practice but is instead approximated with a line integral. The impedance can be sensitive to the position at which the line integral is taken. The positions used here are shown in Figure 5 and are adopted from Richmond [21]. The self impedance is found by approximating the surface current with a filament dipole that is displaced a wire radius away from

14
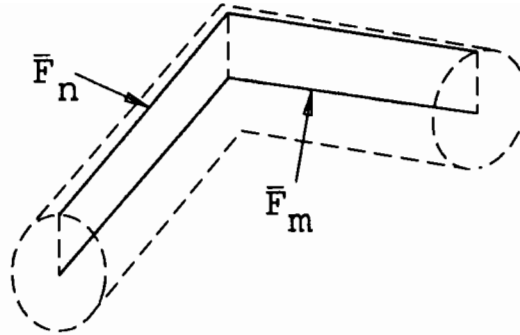
Self Impedance and Overlapping Modes
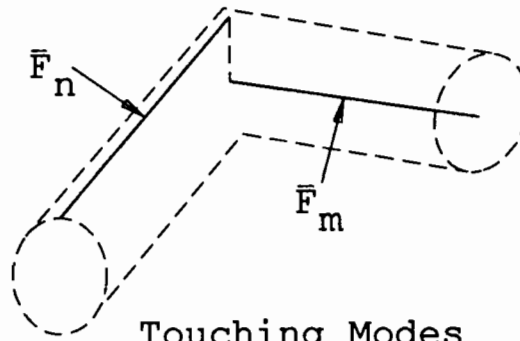
Touching Modes
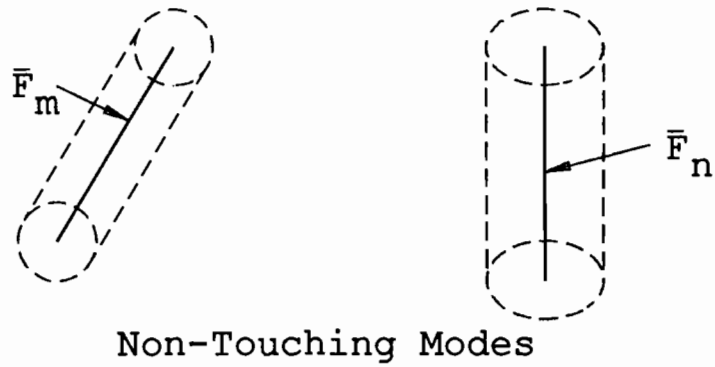
Non-Touching Modes

Figure 5: Position of approximating line integrals.

15

the center test filament in a direction orthogonal to the plane defined by the test filament dipole. This same approach is used for touching and overlapping modes as shown in Figure 5. For modes that do not touch, the integration around the surface is equivalent to replacing the surface current with a filament on the axis of the element.

A wire structure can now be built of N V-dipole elements resulting in N equations:

$$\sum_{n=1}^{N} I_n Z_{mn} = V_m , \qquad m = 1, 2, \ldots, N \qquad (2.23)$$

or in matrix form:

$$[Z][I] = [V] \qquad (2.24)$$

which can then be solved for the unknown current coefficients.

If each V-dipole is now replaced by an infinite linear array of V-dipoles, the same approach will be taken in finding the induced voltage and mutual impedance but the impedance will be defined between arrays of elements instead of between individual elements. The same approximations that were used above will be used hereafter. First, the field from an array of current filaments will be derived.

2.2 Fields of an Infinite Periodic Column of V-dipoles

Upon making the appropriate approximations, the thin wires are reduced to arrays of filamentary currents. Appendix E shows how the fields from an array of straight filaments of current are formulated using Hertzian elements and the concept of vector potential. It also shows that the spectral domain is reached via the application of Poisson's sum transformation to the spatial domain result for Hertzian elements. The electric field from an array of monopoles or "a" leg of a V-dipole,

16

E^a, using the coordinate references and notation from Appendices C is given for the spatial domain in component form as:

$$\overline{E}^a(x,y,z) = \frac{-\eta}{4\pi} \sum_{m=-\infty}^{\infty} e^{-j\beta m D_z s_z} \int_0^A dl_a I^{(a)}(l_a)\frac{e^{-j\beta R_m^{(a)}}}{R_m^{(a)2}}$$

$$\left\{ \hat{x}\left[\gamma_a\left(p_{ax}\epsilon_y^2 + p_{ax}\epsilon_z^2 - p_{ay}\epsilon_x\epsilon_y - p_{az}\epsilon_x\epsilon_z\right) - 2p_{ax}\xi_a\right]\right.$$

$$+\hat{y}\left[\gamma_a\left(p_{ay}\epsilon_x^2 + p_{ay}\epsilon_z^2 - p_{ax}\epsilon_x\epsilon_y - p_{az}\epsilon_y\epsilon_z\right) - 2p_{ay}\xi_a\right]$$

$$\left. +\hat{z}\left[\gamma_a\left(p_{az}\epsilon_x^2 + p_{az}e_y^2 - p_{ax}\epsilon_x\epsilon_z - p_{ay}\epsilon_y\epsilon_z\right) - 2p_{az}\xi_a\right]\right\} (2.25)$$

where

$$m = \text{spatial summation index} \tag{2.26}$$

$$s_z = \text{direction cosine with respect to the } z \text{ axis} \tag{2.27}$$

$$\gamma_a = j\beta R_m^{(a)} + 3 + \frac{3}{j\beta R_m^{(a)}} \tag{2.28}$$

$$\xi_a = 1 + \frac{1}{j\beta R_m^{(a)}} \tag{2.29}$$

$$\beta = \text{propagation constant} \tag{2.30}$$

$$D_z = \text{periodic spacing} \tag{2.31}$$

$$x,y,z = \text{field point} \tag{2.32}$$

$$x',y',z' = \text{source point} \tag{2.33}$$

$$R_m^{(a)} = \sqrt{(x-x')^2 + (y-y')^2 + (z-z'-mD_z)^2} \tag{2.34}$$

$$\epsilon_x = \frac{x-x'}{R_m^{(a)}} \tag{2.35}$$

$$\epsilon_y = \frac{y-y'}{R_m^{(a)}} \tag{2.36}$$

$$\epsilon_z = \frac{z-z'-mD_z}{R_m^{(a)}} \tag{2.37}$$

$$\hat{p}_a = \text{element direction vector} = \hat{x}p_{ax} + \hat{y}p_{ay} + \hat{z}p_{az} \tag{2.38}$$

17

Alternatively in the spectral domain this same field is given as:

$$\overline{E}^a(x,y,z) = \frac{-\eta}{4D_z} \sum_{n=-\infty}^{\infty} e^{-j\beta r_z z} \int_0^A dl_a\, I^{(a)}(l_a) e^{j\beta r_z z'}$$

$$\left\{ \hat{x} \left[p_{ax} \left(\beta r_\rho^2 \frac{(y-y')^2}{\delta^2} H_0^{(2)} - \frac{r_\rho}{\delta} \left(\frac{2(y-y')^2}{\delta^2} - 1 \right) H_1^{(2)} + \beta r_z^2 H_0^{(2)} \right) \right.\right.$$

$$+ p_{ay} \left(-\beta r_\rho^2 \frac{(x-x')(y-y')}{\delta^2} H_0^{(2)} + 2 r_\rho \frac{(x-x')(y-y')}{\delta^3} H_1^{(2)} \right)$$

$$\left. + p_{az} \left(j\beta r_z r_\rho \frac{(x-x')}{\delta} H_1^{(2)} \right) \right]$$

$$+ \hat{y} \left[p_{ax} \left(-\beta r_\rho^2 \frac{(x-x')(y-y')}{\delta^2} H_0^{(2)} + 2 r_\rho \frac{(x-x')(y-y')}{\delta^3} H_1^{(2)} \right) \right.$$

$$+ p_{ay} \left(\beta r_\rho^2 \frac{(x-x')^2}{\delta^2} H_0^{(2)} - \frac{r_\rho}{\delta} \left(\frac{2(x-x')^2}{\delta^2} - 1 \right) H_1^{(2)} + \beta r_z^2 H_0^{(2)} \right)$$

$$\left. + p_{az} \left(j\beta r_z r_\rho \frac{(y-y')}{\delta} H_1^{(2)} \right) \right]$$

$$+ \hat{z} \left[p_{ax} \left(j\beta r_z r_\rho \frac{(x-x')}{\delta} H_1^{(2)} \right) \right.$$

$$\left.\left. + p_{ay} \left(j\beta r_z r_\rho \frac{(y-y')}{\delta} H_1^{(2)} \right) + p_{az} \beta r_\rho^2 H_0^{(2)} \right] \right\}$$

$$(2.39)$$

where

$$n = \text{spectral summation index} \qquad (2.40)$$

$$\delta^2 = (x-x')^2 + (y-y')^2 \qquad (2.41)$$

$$H_0^{(2)} = H_0^{(2)}\left(\beta r_\rho \delta \right) \qquad (2.42)$$

$$H_1^{(2)} = H_1^{(2)}\left(\beta r_\rho \delta \right) \qquad (2.43)$$

$$r_z = s_z + n \frac{\lambda}{D_z} \qquad (2.44)$$

$$r_\rho = \sqrt{1 - r_z^2} \qquad (2.45)$$

18

The question of which domain to use is not easily answered. The currents will be expanded using the piecewise sinusoidal basis function of Figure 3.

Using a sinusoidal current distribution enables the integral in Equation (2.25) to be completed in closed form. This gives it an apparent advantage over Equation (2.39) which does not have a closed form expression for its integral. Unfortunately, the summation in (2.25) is over each element radiating a spherical wave which may be considered "infinitely feeble" at points far removed from the array axis. Thus, even though the integral can be completed in closed form, it may (and will) take many more terms to converge to the solution than Equation (2.39). The number of terms that it takes to converge is dependent upon how far the field point is from the array axis. Very near the array axis, the series is dominated by the $m = 0$ and nearby terms, which is to say that the field at that point comes primarily from the closest elements of the array. It was found that even quite close to the array, a small fraction of a wavelength, a large number of terms, hundreds to thousands, are still required to reach a reasonable level of convergence. Fortunately this series is very amenable to certain acceleration techniques. The Shank's transform [31] in particular has proven to be very successful in reducing the number of terms to a reasonable number. Appendix H provides an overview of the transform and an example of its success. Using this transform, the number of terms necessary for convergence drops dramatically, particularly for cases where the convergence criteria is set very fine.

Equation (2.39) suffers in that the integral must be done numerically when in the near field. Hence, even if only a small number of terms in the series is needed for convergence, the integrand must be evaluated many times in doing the integration. This hampers its effectiveness when the field point is close to the array. As the field point moves away from the array, the number of terms needed in the summation

drops as the evanescent modes quickly die out and the Hankel functions can be replaced by simpler approximations. Appendix F shows how the integral can be completed in closed form when in the "far field." (An infinite array does not really have a far field. The term is used here to indicate that the field point is of sufficient radial distance from the array axis, that the approximations used in Appendix F are valid.)

Summing this up, Equation (2.25) can be integrated in closed form and convergence degrades as the field point moves away from the array axis. Equation (2.39) is integrated numerically in the near field and its convergence improves as the field point moves away from the array axis. Therefore, at some radial distance, it becomes advantageous to switch from using one approach to the other. This distance unfortunately appears to be a function of the element geometry, i.e. the element pattern factor plays its role also. The crossover point is currently a part of the input file and is chosen by experimenting with the geometry of interest. Experience thus far has shown it to be on the order of a few wavelengths, typically.

2.3   Induced Voltage and Mutual Impedance for Arrays of Elements

The induced voltage in an infinite periodic linear array of elements is found in the same manner as with a single element. A single element of the array is chosen as a reference element and the induced voltage found. The process need not be repeated for the other elements of the array since they are related to the reference element by Floquet's theorem [24]. This does assume, however, that the incident wave imparts a linear phase taper along the array axis. Possible sources of interest here include: incident plane waves, infinite line sources whose axes are parallel to

the array axis and other infinite periodic linear arrays whose axes are parallel to the array in question's axis.

When finding the mutual impedance between arrays, Equation (2.22) still applies. The only difference is that now the field from the test filament becomes the field from an infinite linear array of test filaments. The mutual impedance Z_{mn} is still composed of four terms:

$$Z_{mn} = Z_{mn}^{a,a} + Z_{mn}^{a,b} + Z_{mn}^{b,a} + Z_{mn}^{b,b} \tag{2.46}$$

as was shown in Figure 4. In the following paragraphs the explicit equations will be given for the mutual impedance for the spatial and spectral domains. Written out in entirety they are quite long and involved, therefore only the mutual impedance between the two "a" legs for perfectly conducting wires will be shown for the sake of clarity.

Combining Equations (2.22) and (2.25), with some recombination of terms, yields the mutual impedance between two monopoles in the spatial domain as:

$$Z_{12}^{a,a} = \frac{\eta}{4\pi} \sum_{m=-\infty}^{\infty} e^{-j\beta m D_x s_z} \int_0^{A_2} dl_{2a} \frac{I^{(2a)t}(l_{2a})}{I^{(2)t}(\overline{R}^{(2)})} \int_0^{A_1} dl_{1a} \frac{I^{(1a)}(l_{1a})}{I^{(1)}(\overline{R}^{(1)})} \frac{e^{-j\beta R_m^{(1a)}}}{R_m^{(1a)2}}$$
$$\left[\gamma_{1a} \left(c_y \epsilon_y^2 + c_x \epsilon_x^2 + c_z \epsilon_z^2 - c_{xy}\epsilon_x\epsilon_y - c_{xz}\epsilon_x\epsilon_z - c_{yz}\epsilon_y\epsilon_z \right) - 2\xi_{1a}c_{tot} \right] \tag{2.47}$$

where

$$c_y = p_{ax}^{(1)}p_{ax}^{(2)} + p_{az}^{(1)}p_{az}^{(2)} , \ c_x = p_{ay}^{(1)}p_{ay}^{(2)} + p_{az}^{(1)}p_{az}^{(2)} \tag{2.48}$$

$$c_z = p_{ax}^{(1)}p_{ax}^{(2)} + p_{ay}^{(1)}p_{ay}^{(2)} \tag{2.49}$$

$$c_{tot} = p_{ax}^{(1)}p_{ax}^{(2)} + p_{ay}^{(1)}p_{ay}^{(2)} + p_{az}^{(1)}p_{az}^{(2)} \tag{2.50}$$

$$c_{xy} = p_{ay}^{(1)}p_{ax}^{(2)} + p_{ax}^{(1)}p_{ay}^{(2)} , \ c_{xz} = p_{ax}^{(1)}p_{az}^{(2)} + p_{az}^{(1)}p_{ax}^{(2)} \tag{2.51}$$

$$c_{yz} = p_{az}^{(1)}p_{ay}^{(2)} + p_{ay}^{(1)}p_{az}^{(2)} \tag{2.52}$$

21

$$\epsilon_x = \frac{x-x'}{R_m^{(1a)}}, \epsilon_y = \frac{y-y'}{R_m^{(1a)}}, \epsilon_z = \frac{z-z'-mD_z}{R_m^{(1a)}} \tag{2.53}$$

$$\gamma_{1a} = j\beta R_m^{(1a)} + 3 + \frac{3}{j\beta R_m^{(1a)}} \tag{2.54}$$

$$\xi_{1a} = 1 + \frac{1}{j\beta R_m^{(1a)}} \tag{2.55}$$

$$R_m^{(1a)} = \sqrt{(x-x')^2 + (y-y')^2 + (z-z'-mD_z)^2} \tag{2.56}$$

$$x',y',z' = \text{point on leg a of the reference element in array 1} \tag{2.57}$$

$$x,y,z = \text{point on leg a of the reference element in array 2} \tag{2.58}$$

$$p_{ax},p_{ay},p_{az} = \text{direction vector of leg a} \tag{2.59}$$

$$I^{(1)}(\overline{R}^{(1)}) = \text{current at the terminals of array 1} \tag{2.60}$$

$$I^{(2)t}(\overline{R}^{(2)}) = \text{current at the terminals of array 2 under transmitting conditions}$$

$$\tag{2.61}$$

The equations for $Z_{12}^{a,b}$, $Z_{12}^{b,a}$ and $Z_{12}^{b,b}$ are identical to the above equation with substitution of leg b for leg a where appropriate.

No particular basis functions have been assumed in the above equations for the mutual impedance. As was stated in the previous section, if a piecewise sinusoidal basis function is used, the inner integral may actually be completed in closed form (see Appendix D) and the outer integral is given in terms of exponential integrals.

In the spatial domain, the mutual impedance is obtained by finding the voltage induced in the reference element of one array by all of the elements in another array adding them one at a time until the series converges. In the spectral domain, the approach is somewhat different. The mutual impedance is still obtained through the voltage induced in the reference element of one array by all of the elements in another array, but the effect of each element is not summed one at a time. Instead

22

the Poisson sum transformation is first applied as it was in Equation (2.39). The summation is now over the propagating and evanescent composite fields of the second array. Combining Equations (2.22) and (2.39) yields for the <u>spectral</u> domain:

$$
\begin{aligned}
Z_{12}^{a,a} \;=\; & \frac{\eta}{4D_z} \sum_{n=-\infty}^{\infty} e^{-j\beta r_z (z_2^{(2)} - z_2^{(1)})} \\[4pt]
& \cdot \int_0^{A_2} dl_{2a} \frac{I^{(2a)t}(l_{2a})}{I^{(2)t}(\overline{R}^{(2)})} e^{-j\beta r_z p_{az}^{(2)} l_{2a}} \int_0^{A_1} dl_{1a} \frac{I^{(1a)}(l_{1a})}{I^{(1)}(\overline{R}^{(1)})} e^{j\beta r_z p_{az}^{(1)} l_{1a}} \\[4pt]
& \cdot \left[\left(p_{ax}^{(1)} p_{ax}^{(2)} \frac{(y-y')^2}{\delta^2} + p_{ay}^{(1)} p_{ay}^{(2)} \frac{(x-x')}{\delta^2} \right) \beta r_\rho^2 H_0^{(2)} \right. \\[4pt]
& + \left(p_{ax}^{(1)} p_{ax}^{(2)} - p_{ay}^{(1)} p_{ay}^{(2)} \right) \left(\frac{(x-x')^2 - (y-y')^2}{\delta^2} \right) \frac{r_\rho}{\delta} H_1^{(2)} \\[4pt]
& + \left(p_{ax}^{(1)} p_{ax}^{(2)} + p_{ay}^{(1)} p_{ay}^{(2)} \right) \beta r_z^2 H_0^{(2)} \\[4pt]
& + \left(p_{ay}^{(1)} p_{ax}^{(2)} + p_{ax}^{(1)} p_{ay}^{(2)} \right) \left(\frac{(x-x')(y-y')}{\delta^2} \right) \left(-\beta r_\rho^2 H_0^{(2)} + \frac{2r_\rho}{\delta} H_1^{(2)} \right) \\[4pt]
& + \left(\left(p_{az}^{(1)} p_{ax}^{(2)} + p_{ax}^{(1)} p_{az}^{(2)} \right) \frac{(x-x')}{\delta} + \left(p_{az}^{(1)} p_{ay}^{(2)} + p_{ay}^{(1)} p_{az}^{(2)} \right) \frac{(y-y')}{\delta} \right) \\[4pt]
& \left. \cdot j\beta r_z r_\rho H_1^{(2)} + p_{az}^{(1)} p_{az}^{(2)} \beta r_\rho^2 H_0^{(2)} \right]
\end{aligned}
\tag{2.62}
$$

where

$$
H_0^{(2)} \;=\; H_0^{(2)} \left(\beta r_\rho \delta \right)
\tag{2.63}
$$

$$
H_1^{(2)} \;=\; H_1^{(2)} \left(\beta r_\rho \delta \right)
\tag{2.64}
$$

$$
\delta^2 \;=\; (x-x')^2 + (y-y')^2
\tag{2.65}
$$

$$
r_z \;=\; s_z + n\frac{\lambda}{D_z}
\tag{2.66}
$$

$$
r_\rho \;=\; \sqrt{1 - r_z^2}
\tag{2.67}
$$

The equations for $Z_{12}^{a,b}$, $Z_{12}^{b,a}$ and $Z_{12}^{b,b}$ again are identical to the above equation with substitution of leg b for leg a where appropriate.

23

The above equations are used to fill the impedance matrix when perfectly conducting, unloaded dipoles are involved. The addition of finite conductivity, lumped loads and thin dielectric coatings will only alter the matrix terms involving the self impedance terms and those which have overlapping elements in the approximations used here. Appendix G contains the details of how each of these variations is handled.

The voltage vector elements are found using Equation (2.21). For plane wave incidence the electric field is given as:

$$\overline{E} \;=\; \overline{E}^i e^{j\beta \overline{R}' \cdot \hat{s}} = \overline{E}^i e^{j\beta(x' s_x + y' s_y + z' s_z)} \tag{2.68}$$

Using the piecewise-sinusoidal basis function (2.20), the induced voltage can be found in closed form and is given by:

$$V \;=\; e^{j\beta w}\overline{E}^i \cdot \left\{ \hat{p}_a \frac{1}{2\beta \sin \beta A}\left[e^{j\beta A}\frac{\left(e^{j\beta(t_a-1)A}-1\right)}{(t_a-1)} - e^{-j\beta A}\frac{\left(e^{j\beta(t_a+1)A}-1\right)}{(t_a+1)}\right] \right.$$
$$\left. + \hat{p}_b \frac{1}{2\beta \sin \beta B}\left[e^{-j\beta B}\frac{\left(e^{-j\beta(t_b-1)B}-1\right)}{(t_b-1)} - e^{j\beta B}\frac{\left(e^{-j\beta(t_b+1)B}-1\right)}{(t_b+1)}\right] \right\} \tag{2.69}$$

where

$$w \;=\; x_2 s_x + y_2 s_y + z_2 s_z \tag{2.70}$$

$$x_2, y_2, z_2 \;=\; \text{position of terminals of element 2} \tag{2.71}$$

$$t_a \;=\; p_{ax} s_x + p_{ay} s_y + p_{az} s_z \tag{2.72}$$

$$t_b \;=\; p_{bx} s_x + p_{by} s_y + p_{bz} s_z \tag{2.73}$$

$$\hat{p}_a, \hat{p}_b \;=\; \text{direction vectors of legs a and b} \tag{2.74}$$

$$\overline{E}^i \;=\; E_\theta \hat{\theta} + E_\phi \hat{\phi} \tag{2.75}$$

Alternatively it may be desirable to have a line source provide the incident field in which case:

$$\overline{E}^i = \begin{cases} \hat{z}E_e^i H_0^{(2)}\big(k|\bar{\rho}-\bar{\rho}'|\big) & \text{for electric line source} \\ \hat{\phi}E_m^i \frac{\partial}{\partial\rho}H_0^{(2)}\big(k|\bar{\rho}-\bar{\rho}'|\big) & \text{for magnetic line source} \end{cases} \quad (2.76)$$

This incident field is then substituted into Equation (2.21) and the integral completed numerically.

One interesting aspect of the impedance equations is that they are related to the incident field only through s_z, the incident direction with respect to the array axis, and the frequency. This can be used advantageously in computing the scattered fields. If s_z and the frequency are fixed, the direction of the incident field can be altered without recalculating the impedance matrix. Conversely, if s_z or the frequency is varied, the impedance matrix must be recalculated for each change.

2.4 Implementation

A computer code was written utilizing the equations of the previous section. For the spatial domain, the mutual impedance between individual V-dipole elements has been previously programmed by Richmond [22]. Richmond's thin wire code has been in use for many years and has been thoroughly tested and validated proving its robustness. Rather than writing routines that yield identical results to those of Richmond. I have used some of the base subroutines from the thin wire code directly. This also helps in validating the spectral domain results by direct comparison with the spatial domain results.

The series is accelerated in the spatial domain using the Shanks transform as shown in Appendix H. An attempt was also made to use the transform of Wynn [32] as suggested by Singh [33] but this did not prove to be successful. It was also found

that neither the Wynn transform nor a first order Shanks transform were successful in accelerating the spectral domain summation. This did not prove to be bothersome, however, since the spectral domain solution is not utilized until only a few terms of the series are necessary.

In running the program, the geometry and physical parameters of the scattering structure are entered, the source type and, if necessary, location are entered and then the type of pattern is chosen which dictates what other inputs are necessary. The pattern choices currently are a bistatic scattering pattern, whereby the scattered fields are found over a specified range of phi for a fixed input angle and frequency, a monostatic scattering pattern, whereby s_z and the frequency are fixed and the backscattered fields are found over a specified range of phi, and a frequency sweep, whereby the frequency varies over a specified range and the scattered field is found at a fixed angle for a fixed input angle.

For s_z not equal to zero, a monostatic pattern does not really exist. Since the array is infinite along the z axis, there is no scattered field pattern with theta per se, except for a singular spike in the specular direction. When s_z is not zero, the program automatically finds the fields in the specular direction with respect to the z axis.

The following chapters present results for a variety of geometries illustrating the importance and usefulness of this analysis.

CHAPTER III

Single Columns and Dielectric Coatings

In the design of periodic surfaces it is common practice to utilize dielectric layers to control grating lobes, minimize scan angle variations and simply to hold the structure together. The analysis of a planar two-dimensionally infinite structure in a stratified media is straight forward when completed in the spectral domain. A finite number of plane waves bouncing among a finite number of planar surfaces is mostly a problem of bookkeeping. If the problem is changed to having only a one-dimensionally infinite periodic structure the analysis becomes more involved due to the non-planar waves being emitted, though it is tractable if the dielectric layers remain planar and infinite [34, 35]. If the dielectric layers are not planar or are truncated, the analysis becomes much more difficult and will probably result in rather large computational demands if, for example, a full moment method for volumetric equivalent currents solution were implemented. The benefits of dielectric are very compelling however and a physical structure must be supported somehow.

Richmond [21] showed that thin dielectric coatings on thin wires can be incorporated in the analysis of thin wire structures very easily. His approach is given analytically in Appendix G and this chapter will show some calculated results utilizing thin dielectric coatings. It is hoped that thin coatings will yield at least some of the benefits of dielectric layers and provide a reasonable approximation to having the elements on a thin dielectric sheet. It is also possible to conceive of structures,

such as arrays of wire antennas, that may well be self supporting via their feeds and could benefit from the use of dielectric coatings.

The effects of element spacing and wire radius will also be presented here as they go hand in hand with dielectric coating concerns.

3.1 Axially Oriented Straight Dipoles

The first case to be considered is a single column of axial dipoles as in Figure 6. Each of the dipoles is modeled with three overlapping elements or modes and the lengths of the dipoles will be adjusted such that they resonate at 3.0 GHz with and without dielectric coatings. Resonance will be determined by the imaginary part of the scan impedance going to zero. The scan impedance is found by simply dividing the voltage induced in an element due to the incident field by its resulting current. For each of the plots presented in this chapter, the scan impedance of the center element of the dipole is given and as the length of the dipole is changed, the length of the center element is changed proportionately as shown in Figure 6. The effect of varying the array spacing, D_z, will also be studied. The excitation is a plane wave incident at an angle orthogonal to the array axis.

Figure 7 contains four curves. The rightmost one, A, is for elements with no dielectric coating, spacing $D_z = 4.8$ cm, wire radius $= .02$ cm and an ambient medium of free space. This radius corresponds to AWG-26 wire. The resulting length for resonance at 3.0 GHz is 4.56 cm. The leftmost curve, D, is for elements with no dielectric coating, spacing $D_z = 2.4$ cm, wire radius $= .01$ cm, length $= 2.28$ cm and an ambient medium with a relative dielectric constant of 4.0. This can be thought of as a coating that is infinite in extent. This element is scaled by a factor of 2 in every dimension to allow for the ambient medium. Those two cases

z

ℓ

D_z

Wire radius=0.02cm

y

x

3 Modes

End view

r_w=wire radius

r_d=dielectric coating radius

ℓ/4

ℓ/4

ℓ/4

ℓ/4

r_d

r_w
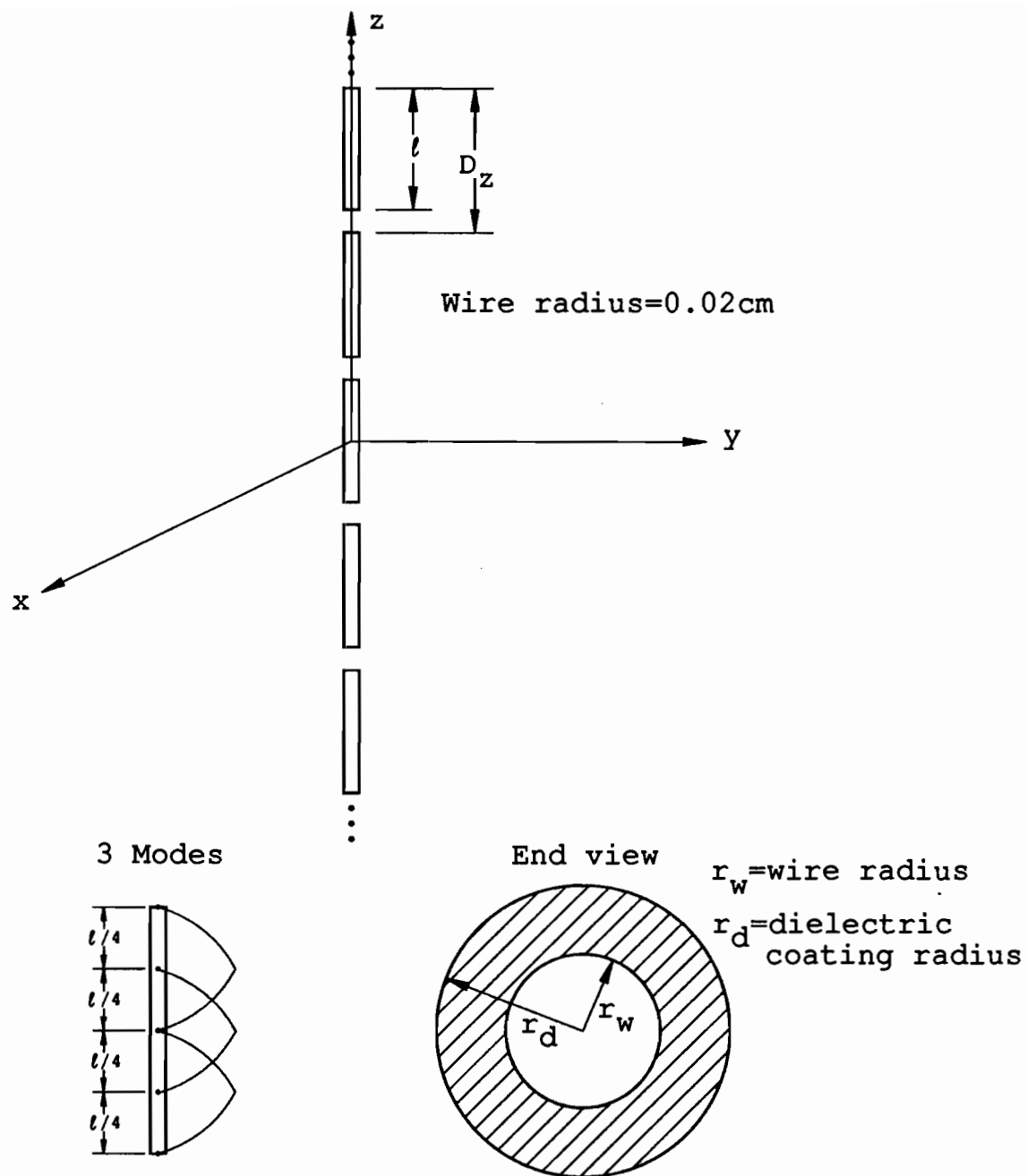
Figure 6: Single column of axially oriented straight dipoles with a dielectric coating.

Case	l(cm)	D_z(cm)	r_w(cm)	r_d(cm)	ϵ_{coat}	ϵ_{amb}
A	4.56	4.8	.02	NA	NA	1.0
B	4.28	4.8	.02	.04	4.0	1.0
C	3.99	4.8	.02	.08	4.0	1.0
D	2.28	2.4	.01	NA	NA	4.0
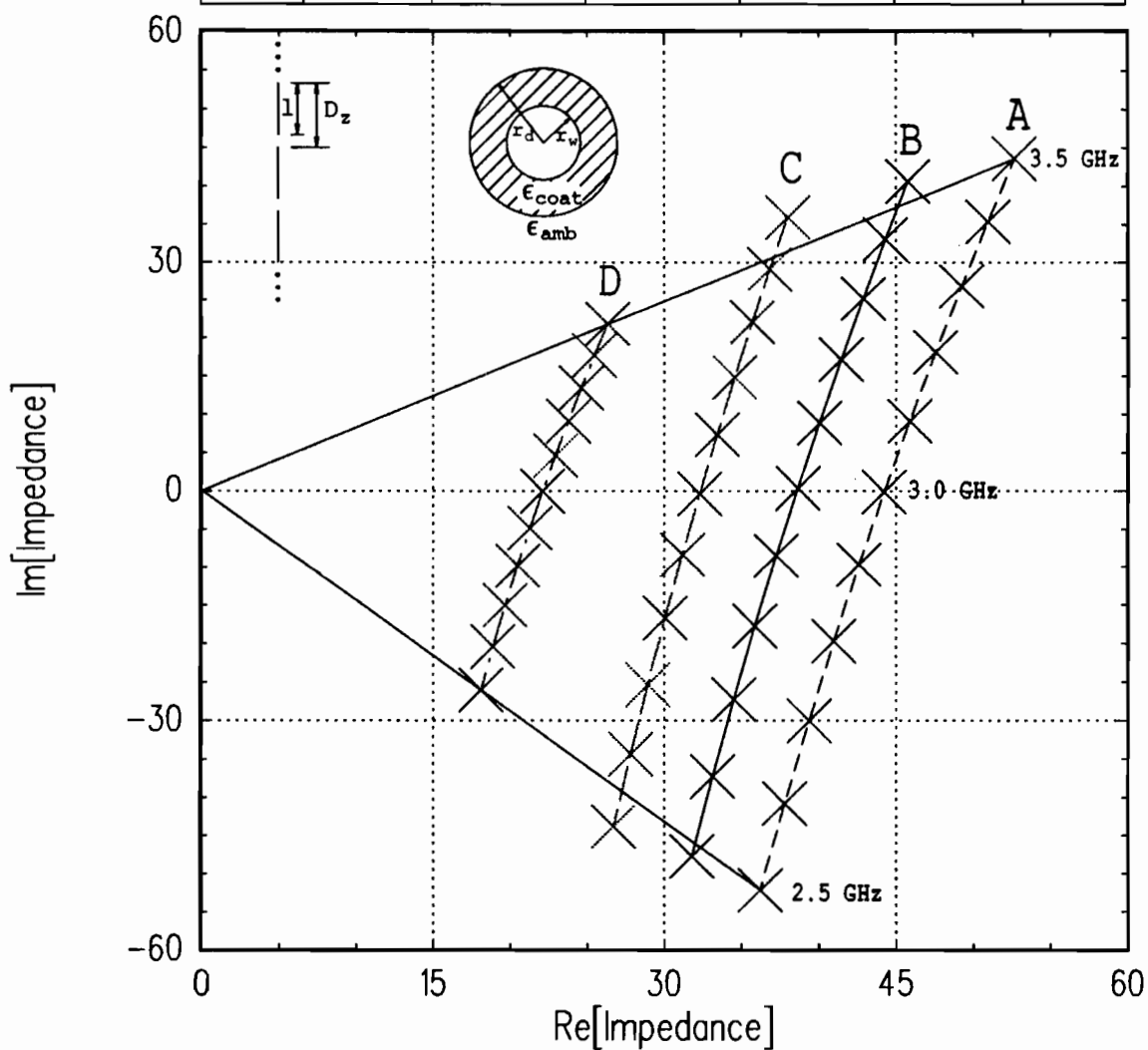
Figure 7: Scan impedance of a single column of axially oriented straight dipoles with a dielectric coating for fixed D_z.

will be the extremes of adding a dielectric coating with a relative dielectric constant of 4.0.

The two remaining curves, B and C are for elements with dielectric coatings of radius .04 cm and .08 cm. The array spacing was held constant at $D_z = 4.8$ cm as it was without a dielectric coating. The results are consistent with what would be intuitively expected. The impedance of the elements with the thicker coating lie closer to the ambient dielectric case and their length, 3.99 cm, is shorter than that of the thinner case, 4.28 cm. The shortening of the elements is advantageous in that the elements may now be packed closer together, delaying the onset of grating lobes.

In Figure 8 the two extreme curves are repeated for comparison and the spacing, D_z, is altered for the two cases with a dielectric coating. For the thinner coating, radius = .04 cm, the spacing is reduced to $D_z = 4.4$ cm and for the thicker coating, radius = .08 cm, the spacing is reduced to 3.9 cm. The result is that the real part of the impedance is seen to increase and the variation of impedance with frequency is seen to decrease when comparing Figures 7 and 8.

The bandwidth is determined by the variation of the impedance. An envelope of constant bandwidth is shown on each of the previous figures as a straight line connecting corresponding frequency points on the extreme curves, which have the same bandwidth, and the origin. Adding the dielectric coating, without decreasing the spacing, yields shorter elements but results in less bandwidth as seen in Figure 7. Decreasing the spacing restores the bandwidth as seen in Figure 8. This is also seen in Figure 9 which shows the total scattered fields for the coated and uncoated cases in free space. The top plot corresponds to Figure 8 and the bottom to Figure 7. It is seen that decreasing the spacing on the coated elements restores the bandwidth to that of the uncoated elements.

Case	l(cm)	D_z(cm)	r_w(cm)	r_d(cm)	ϵ_{coat}	ϵ_{amb}
A	4.56	4.8	.02	NA	NA	1.0
B	4.17	4.4	.02	.04	4.0	1.0
C	3.70	3.9	.02	.08	4.0	1.0
D	2.28	2.4	.01	NA	NA	4.0
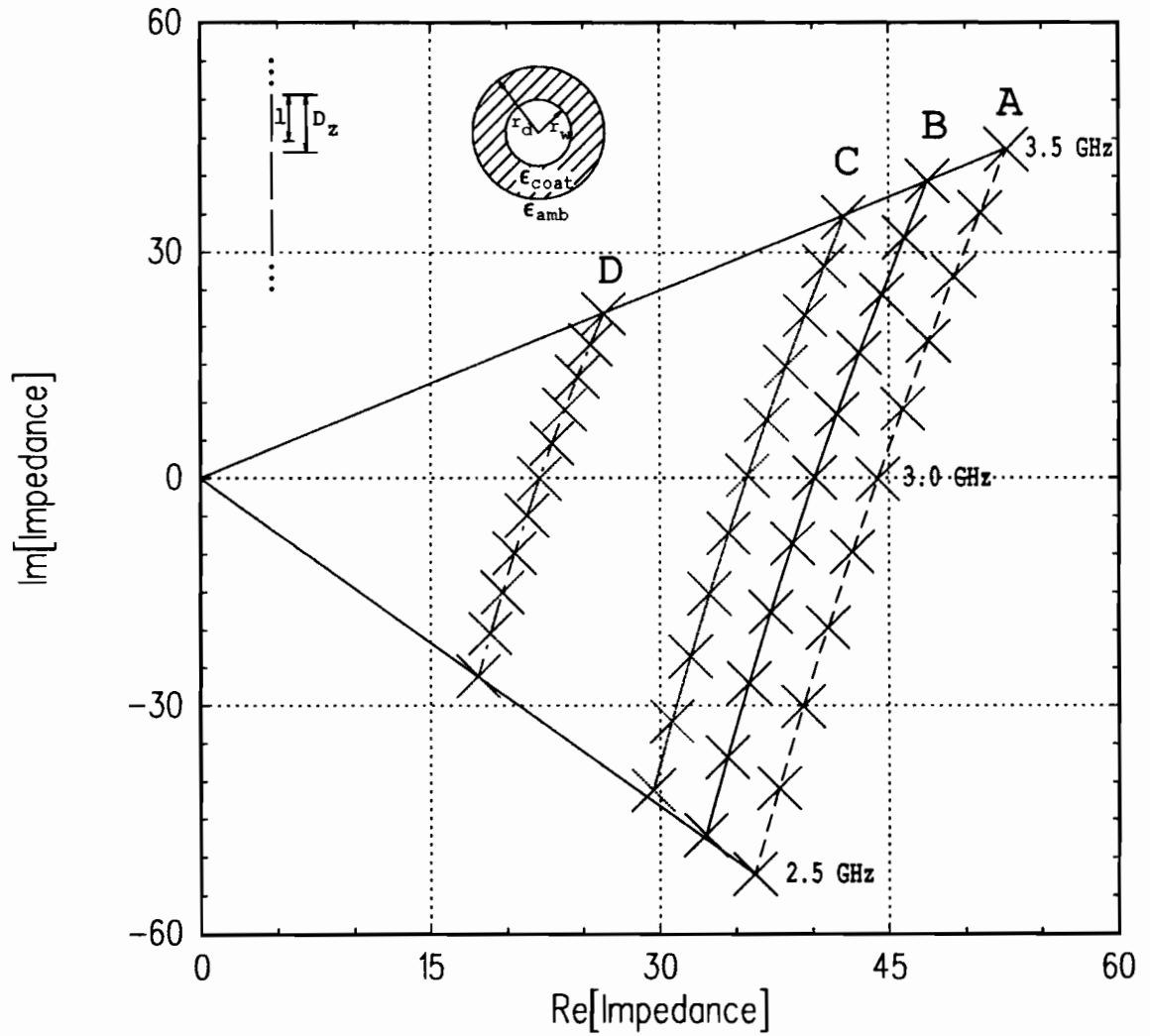
Figure 8: Scan impedance of a single column of axially oriented straight dipoles with a dielectric coating for variable D_z.

Figure 9: Backscattered field versus frequency for a single column of dielectric coated axial dipoles. D_z is allowed to vary in the top plot and is held fixed in the bottom plot.

33

Decreasing the spacing, D_z, was seen to increase the bandwidth. For straight axial dipoles there is a limit on how close the elements can be and yet maintain the length necessary to resonate at 3.0 GHz. Figure 10 shows three curves for spacings of $D_z = 4.6$ cm, $D_z = 4.8$ cm and $D_z = 5.4$ cm. The bandwidth is seen to increase with decreasing spacing and the element length necessary to maintain the desired resonance is seen to decrease. The closer the elements are together, the stronger the coupling between them. The ends of the elements appear to be loaded, in effect making them longer. Hence, the smaller the spacing between axially oriented elements, the shorter they need to be.

Another parameter that directly affects the bandwidth is the wire radius. The result of varying the radius of the uncoated wire is shown in Figure 11. The bandwidth is seen to vary significantly with variation of wire radius. The fatter the wire, the greater the bandwidth. This can only be applied up to the thin wire limit here however, and there are no guarantees that once that limit is exceeded, that other phenomena might not supercede this trend.

3.2   Transversely Oriented Straight Dipoles

The above analysis is now repeated for elements transverse to the array axis as shown in Figure 12. The rightmost curve, A, of Figure 13 is for elements with no dielectric coating, spacing $D_z = 3.0$ cm, wire radius $= .02$ cm and an ambient medium of free space. The leftmost curve, B, is for elements with no dielectric coating, spacing $D_z = 1.5$ cm, wire radius $= .01$ cm and ambient medium with a 4.0 relative dielectric constant. These two cases will be the extremes of adding a dielectric coating with a relative dielectric constant of 4.0 for the transverse oriented case.
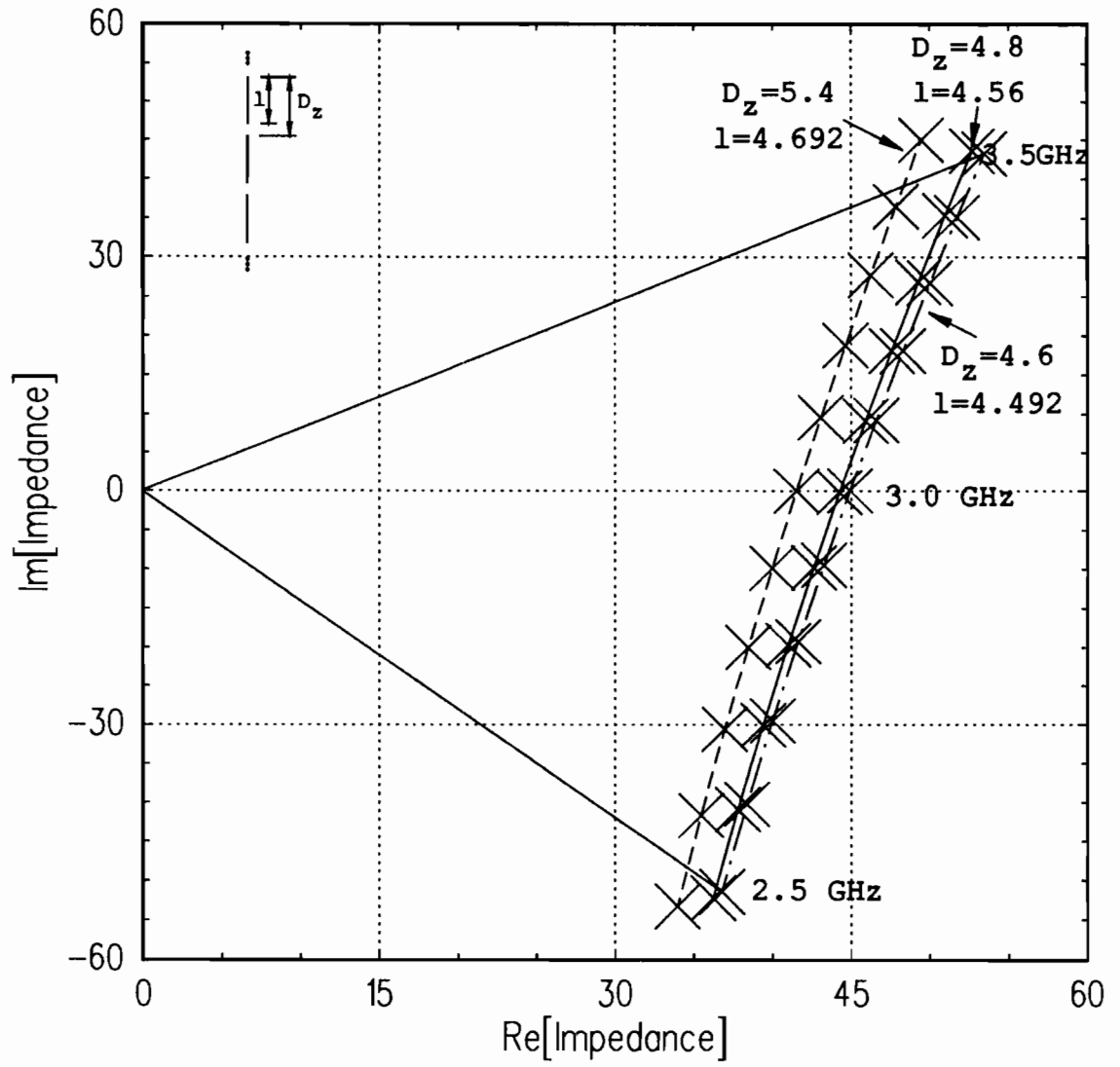
Figure 10: Scan impedance of a single column of uncoated axial dipoles as D_z is varied.

Figure 11: Scan Impedance of a single column of uncoated axial dipoles as the wire radius is varied.
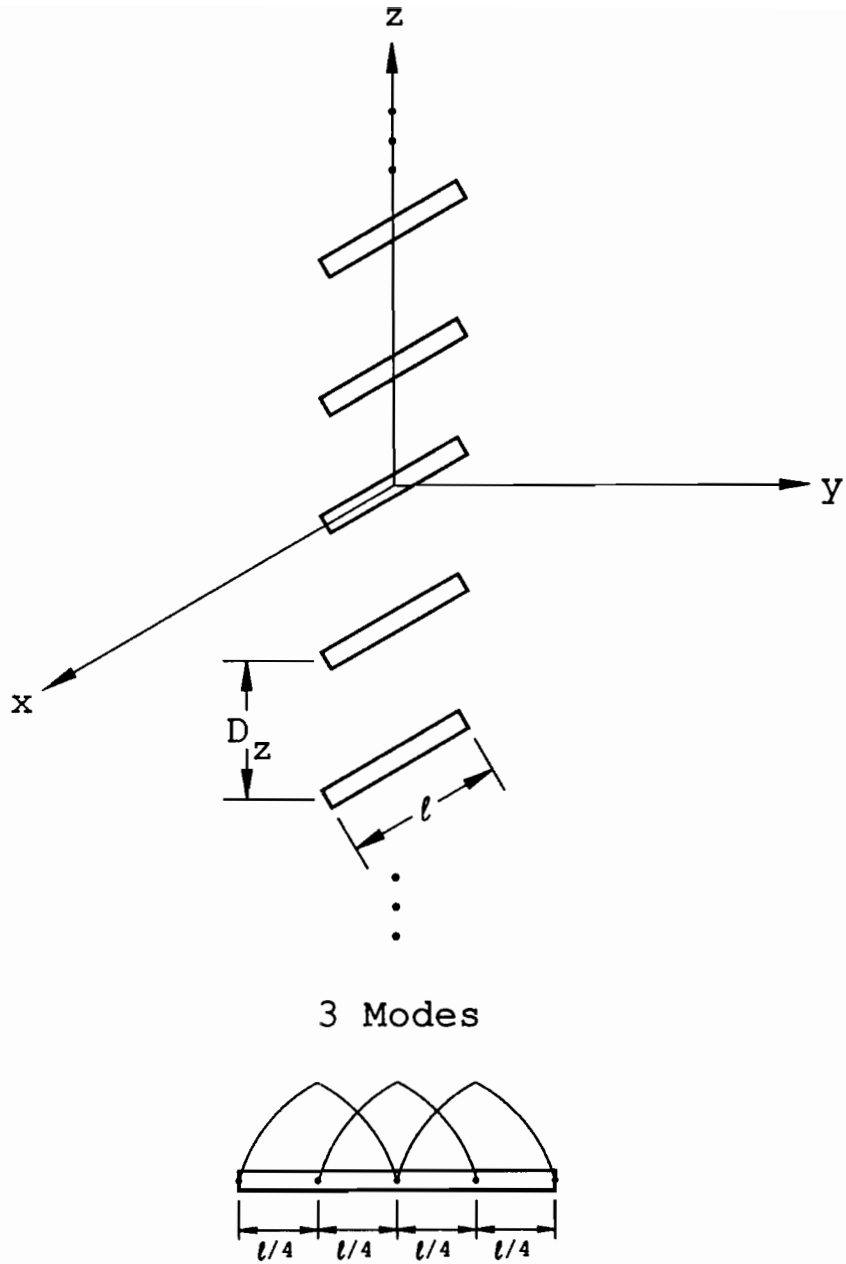
Figure 12: Single column of transversely oriented straight dipoles with a dielectric coating. The dipoles shown are parallel to the x axis, but in general, transversely oriented elements may have any orientation parallel to the x-y plane.

Case	l (cm)	D_z(cm)	r_w(cm)	r_d(cm)	ϵ_{coat}	ϵ_{amb}
A	5.24	3.0	.02	NA	NA	1.0
B	4.84	3.0	.02	.04	4.0	1.0
C	4.40	3.0	.02	.08	4.0	1.0
D	2.62	1.5	.01	NA	NA	4.0
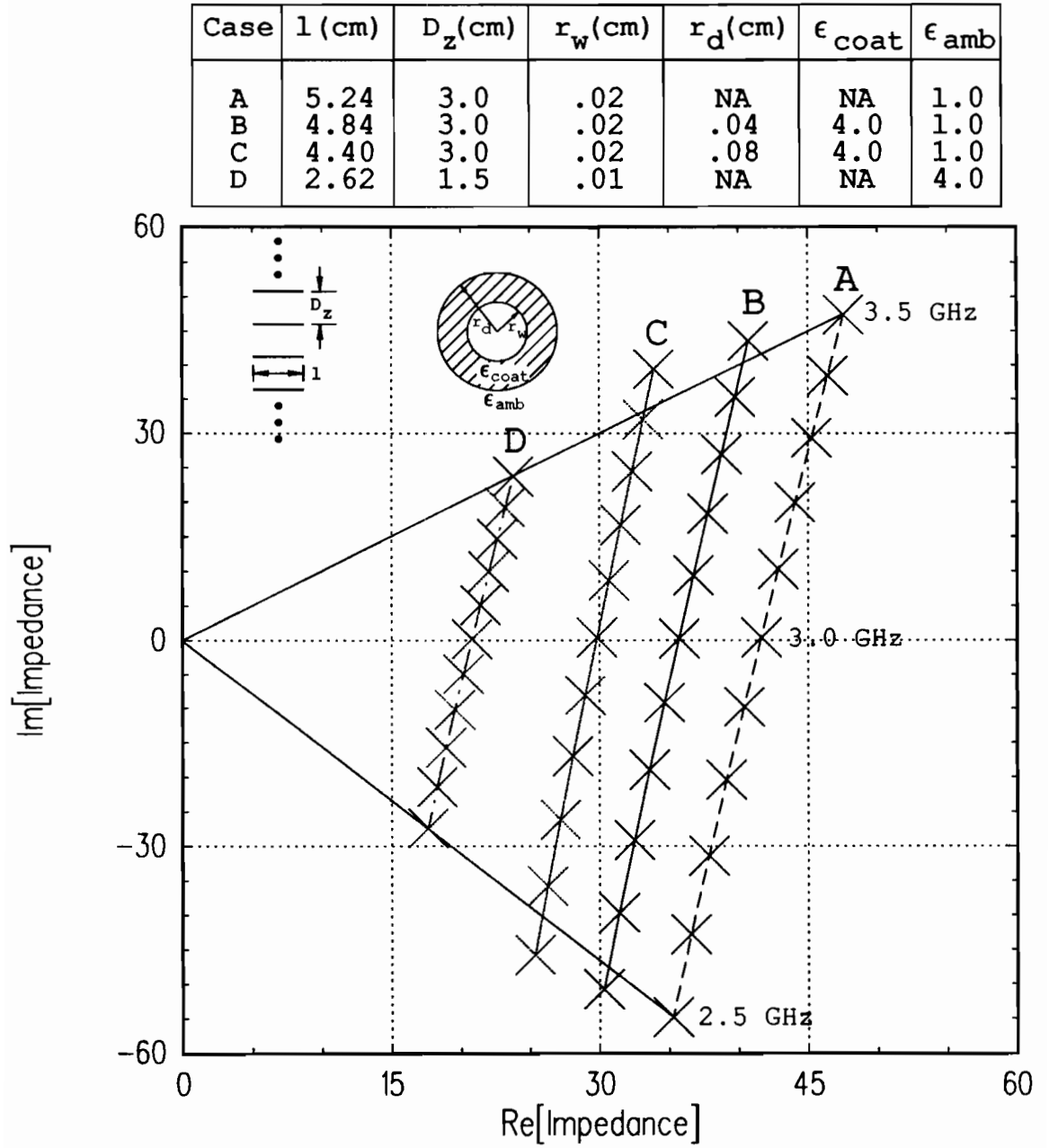
Figure 13: Scan impedance of a single column of transverse straight dipoles with a dielectric coating for fixed D_z.

38

The other two curves, B and C, are for elements in free space with dielectric coatings of radius .04 cm and .08 cm. The array spacing was held constant at $D_z = 3.0$ cm, the same as for the uncoated free space case. Again, the elements with the thicker coating look more like the ambient 4.0 case and are shorter, with a length of 4.4 cm, while ones with the thinner coating have a length of 4.84 cm. These are compared to the uncoated elements which have a length of 5.24 cm. Again, without altering the element to element spacing, the bandwidth decreases with increasing coating thickness. The benefits of dielectric coating are not evident in a single column of transversely oriented elements. However, if multiple columns are placed side by side, the decreased element length can be used to place the columns closer together.

The array spacing, D_z, for the coated elements was decreased yielding the results shown in Figure 14. The spacing for the .04 cm coating is reduced to 2.8 cm which increases the bandwidth, shifts the curve toward the uncoated case and requires a slightly longer element. The spacing for the .08 cm coating is reduced to 2.5 cm which has the same effects as reducing the .04 cm coating spacing. The increase in required length with decreased spacing is opposite to the axial case where the required length decreased with decreased spacing. A plot of the magnitude of the scattered fields versus frequency is shown in Figure 15 for the variable and fixed D_z cases.

Figure 16 shows the effects of varying the spacing D_z for uncoated transverse elements. As was true above for the coated elements, decreasing the spacing yields an increase in bandwidth and an increase in the required element length. Unlike the axial elements, decreasing the element spacing for the transverse case results in a required increase in element length to compensate.

| Case	l(cm)	D_z(cm)	r_w(cm)	r_d(cm)	ϵ_{coat}	ϵ_{amb}
A	5.24	3.0	.02	NA	NA	1.0
B	4.88	2.8	.02	.04	4.0	1.0
C	4.49	2.5	.02	.08	4.0	1.0
D	2.62	1.5	.01	NA	NA	4.0
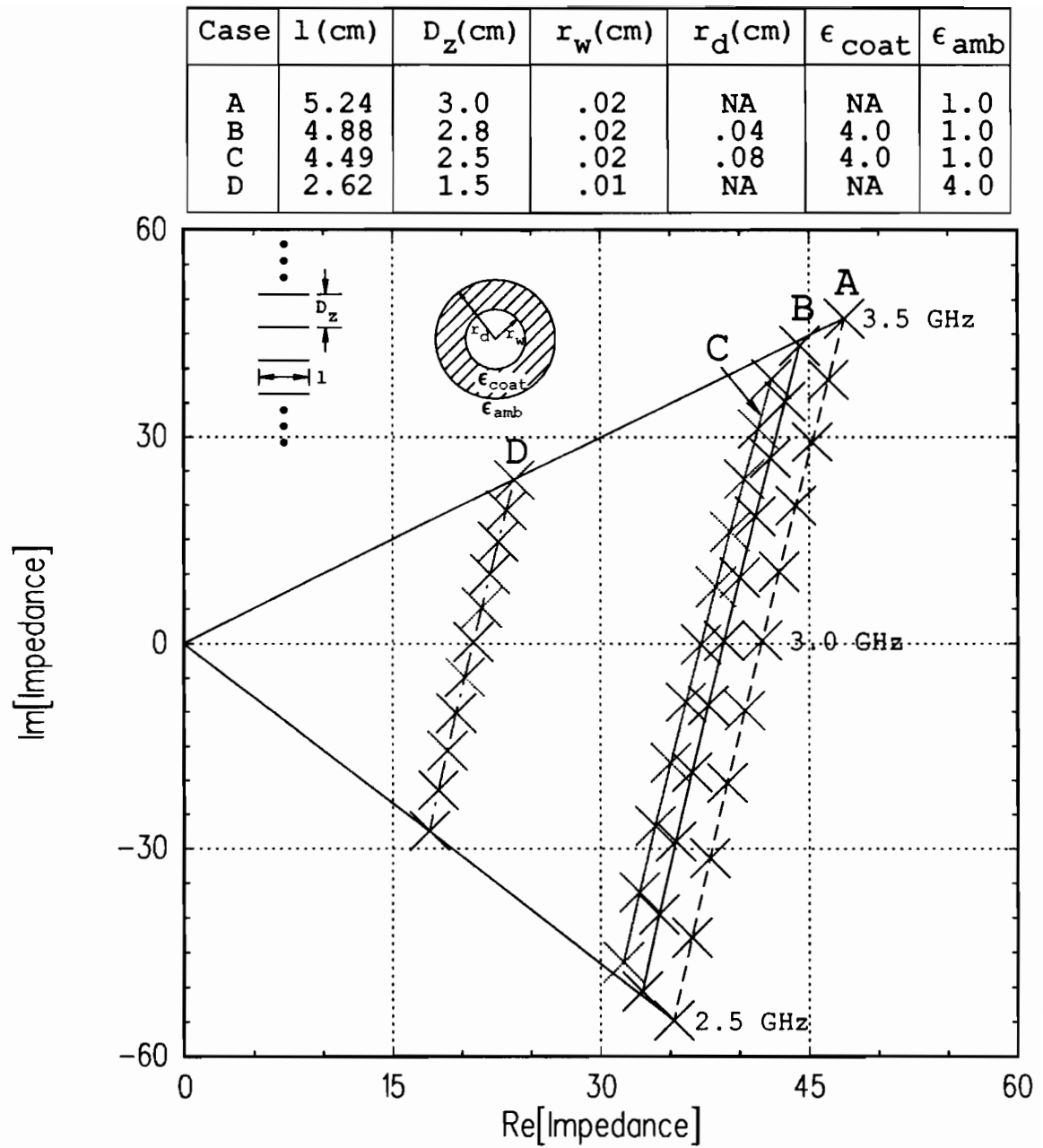
Figure 14: Scan impedance of a single column of transverse straight dipoles with a dielectric coating for variable D_z.
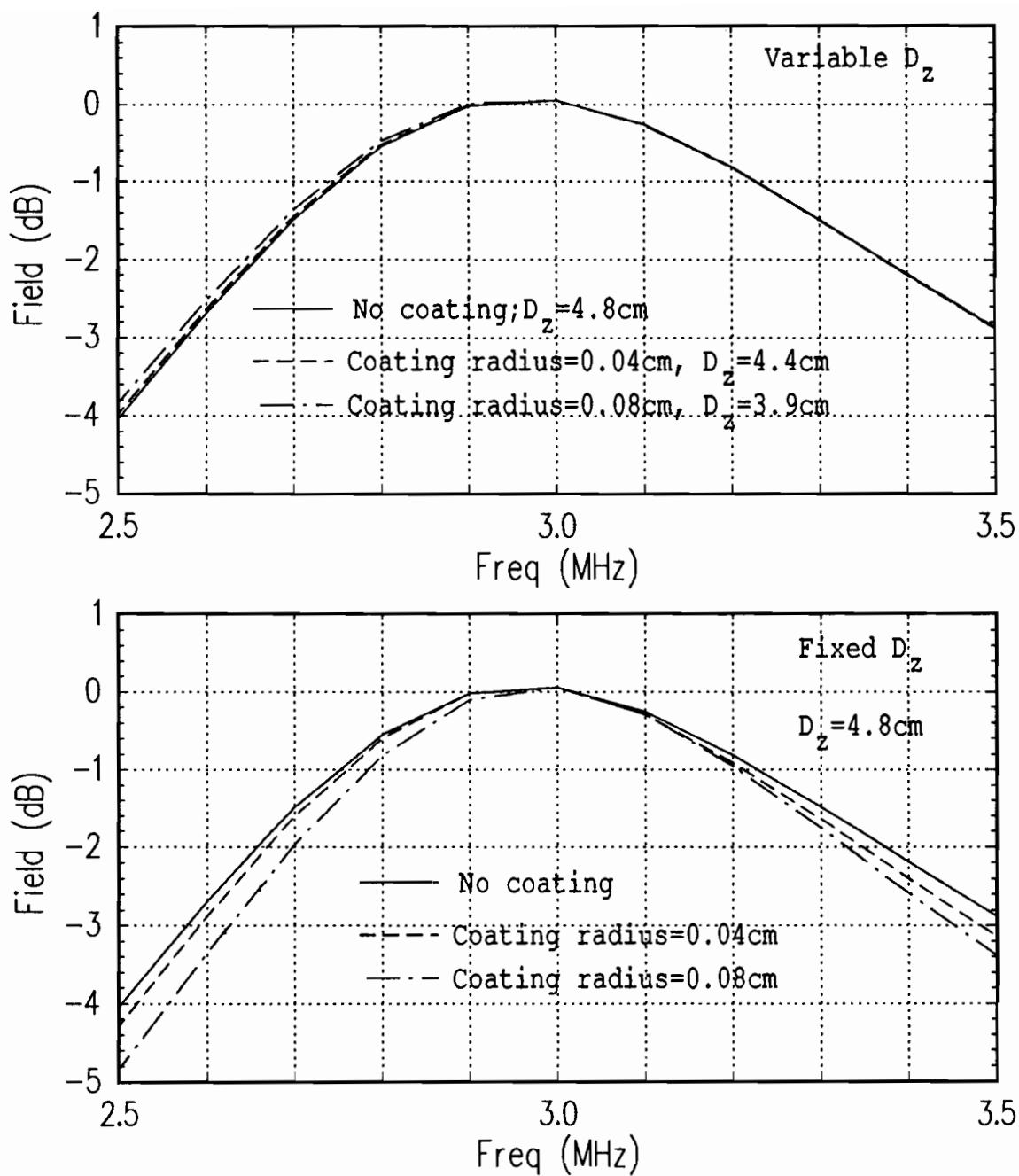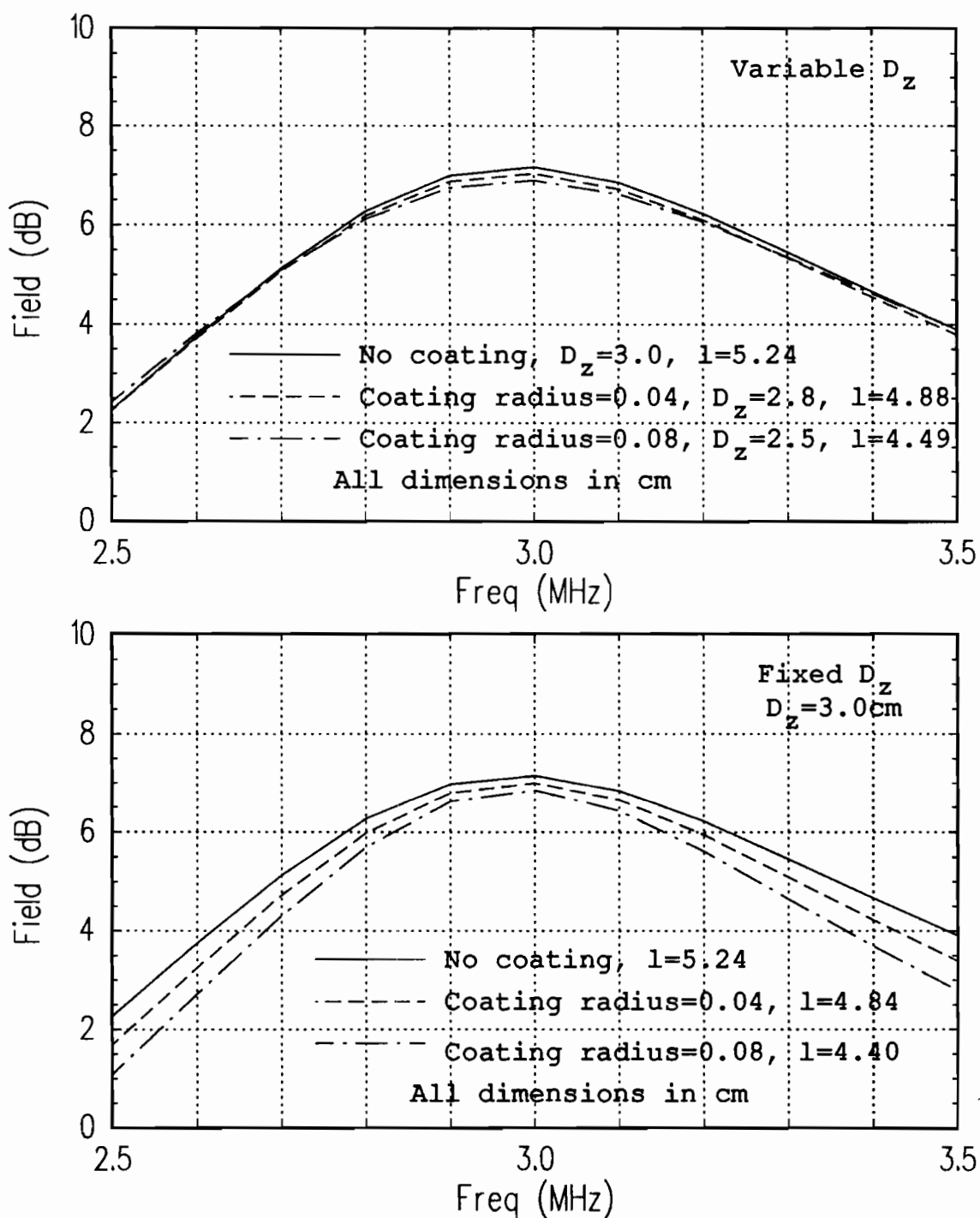
Figure 15: Backscattered field versus frequency for a single column of dielectric coated transverse dipoles.
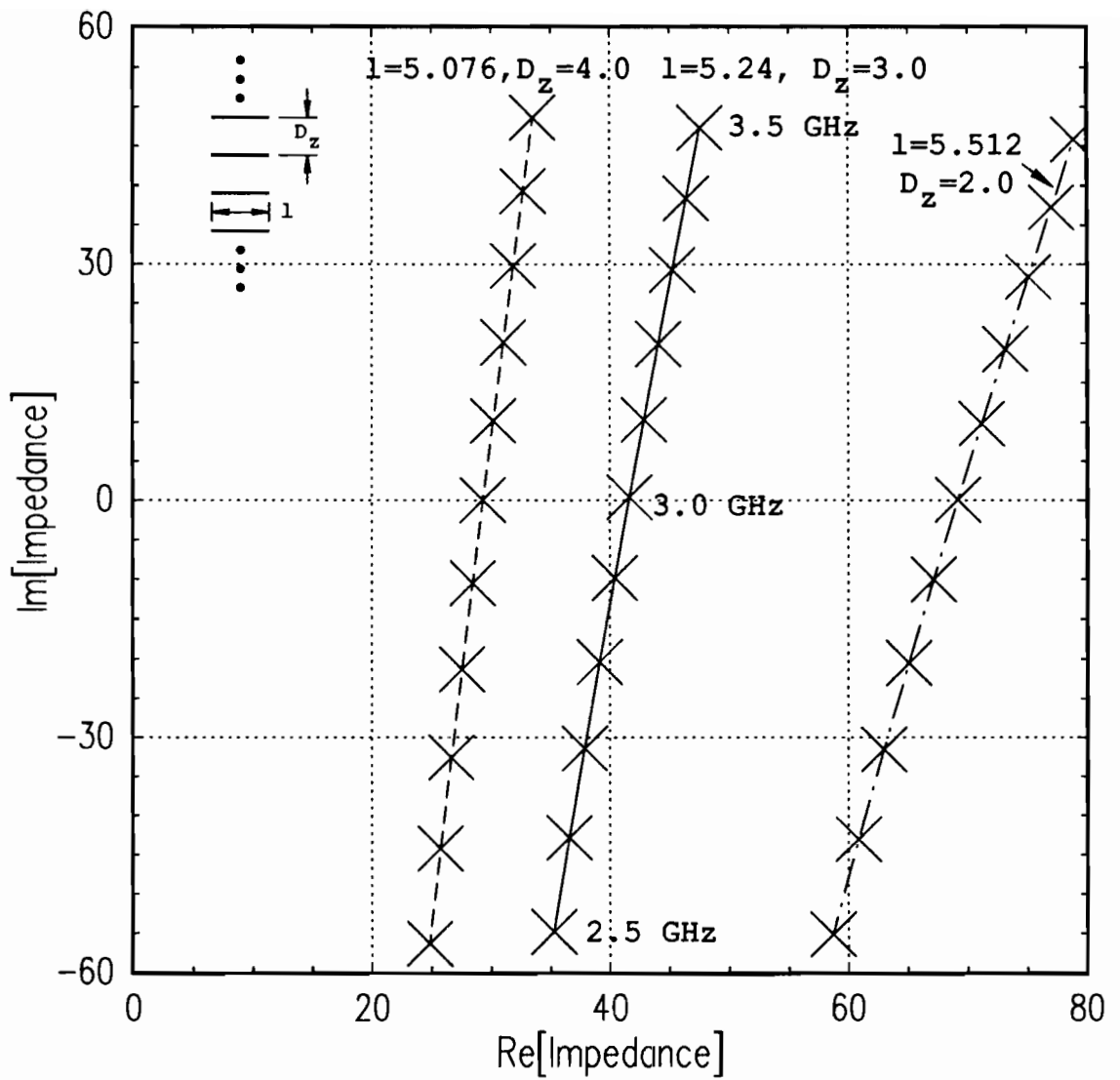
Figure 16: Scan impedance of a single column of uncoated transverse dipoles for varied D_z.

Figure 17 shows the effect of varying the element radius for the transverse case. As in the axial case, increasing the element radius increases the bandwidth.

3.3 Bent Dipoles

The next geometry under consideration is a column of dipoles bent at a 90 degree angle as shown in Figure 18. The elements lie in the y-z plane and a plane wave is incident along the y axis. The scan impedance for this geometry is shown in Figure 19 for four cases as before. The extreme cases are again for an uncoated element in free space, with a spacing of $D_z = 2.5$ cm here, and an uncoated element in ambient 4.0 with all its proportions and spacing halved. The two center curves have dielectric coatings of $\epsilon_r = 4.0$ with radii of .04 cm and .08 cm as indicated.

Figure 20 shows the effects of reducing the element spacings of the coated elements as indicated on the plot. The required lengths decrease with decreased spacing suggesting that end loading is dominant as in axial dipoles.

The slope of the impedance curve also appears to be quite different from that seen in the axial and transverse cases. A possible cause of this may be that in the first two cases the phase of the induced voltage is uniform across the element, but for this case there is a phase variation across the element for the incident angle shown. To test this, the uncoated element was rerun for a plane wave incident along the x axis ($\phi_{in} = 0$ degrees) yielding uniform phase across the element. The results are shown in Figure 21 along with the $\phi_{in} = 90$ degrees case previously shown. The impedance variation now appears to be similar to the axial and transverse cases and the resonant frequency has shifted between $\phi_{in} = 0$ degrees and $\phi_{in} = 90$ degrees as indicated by the length change required to maintain resonance at 3 GHz.
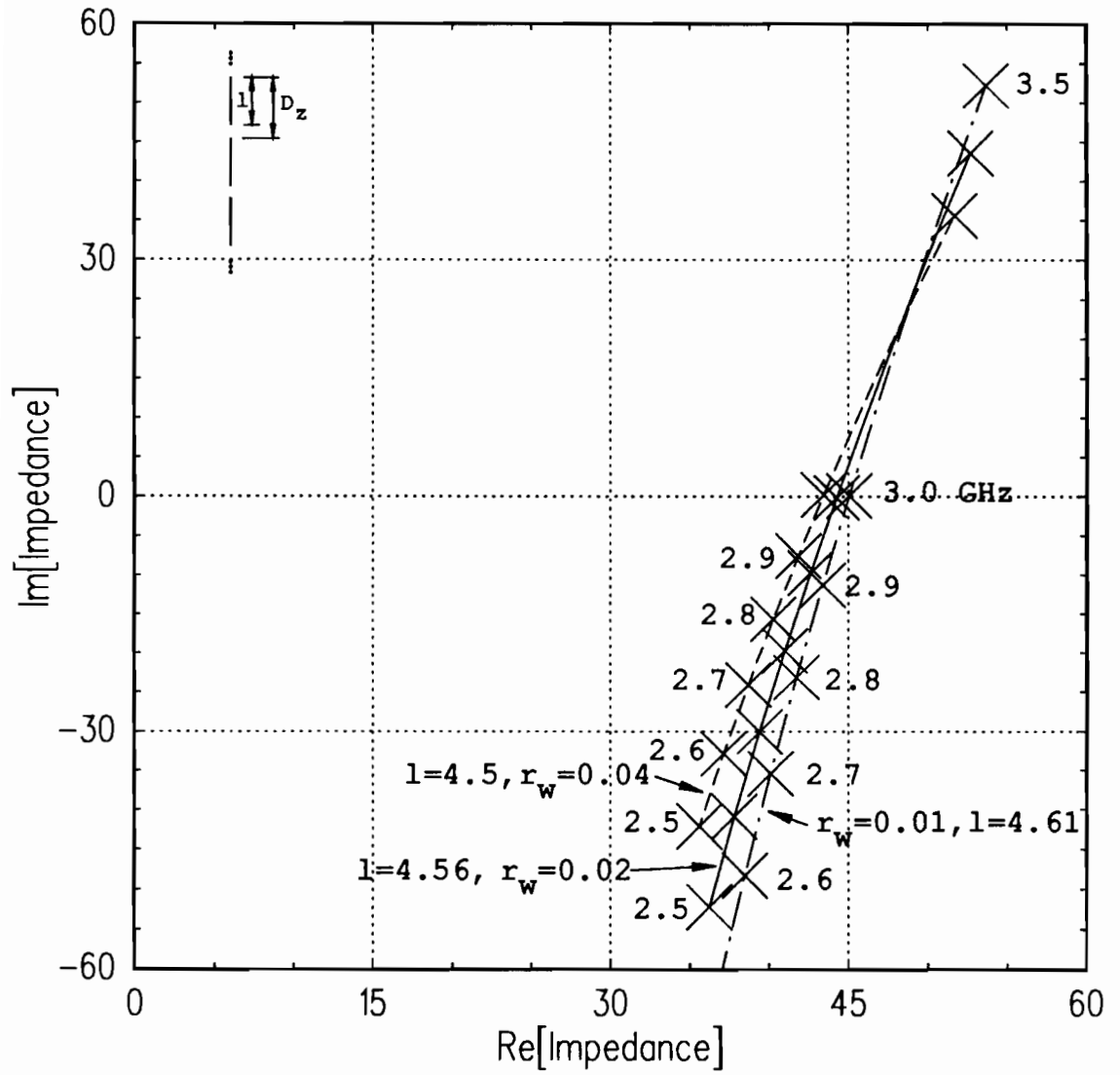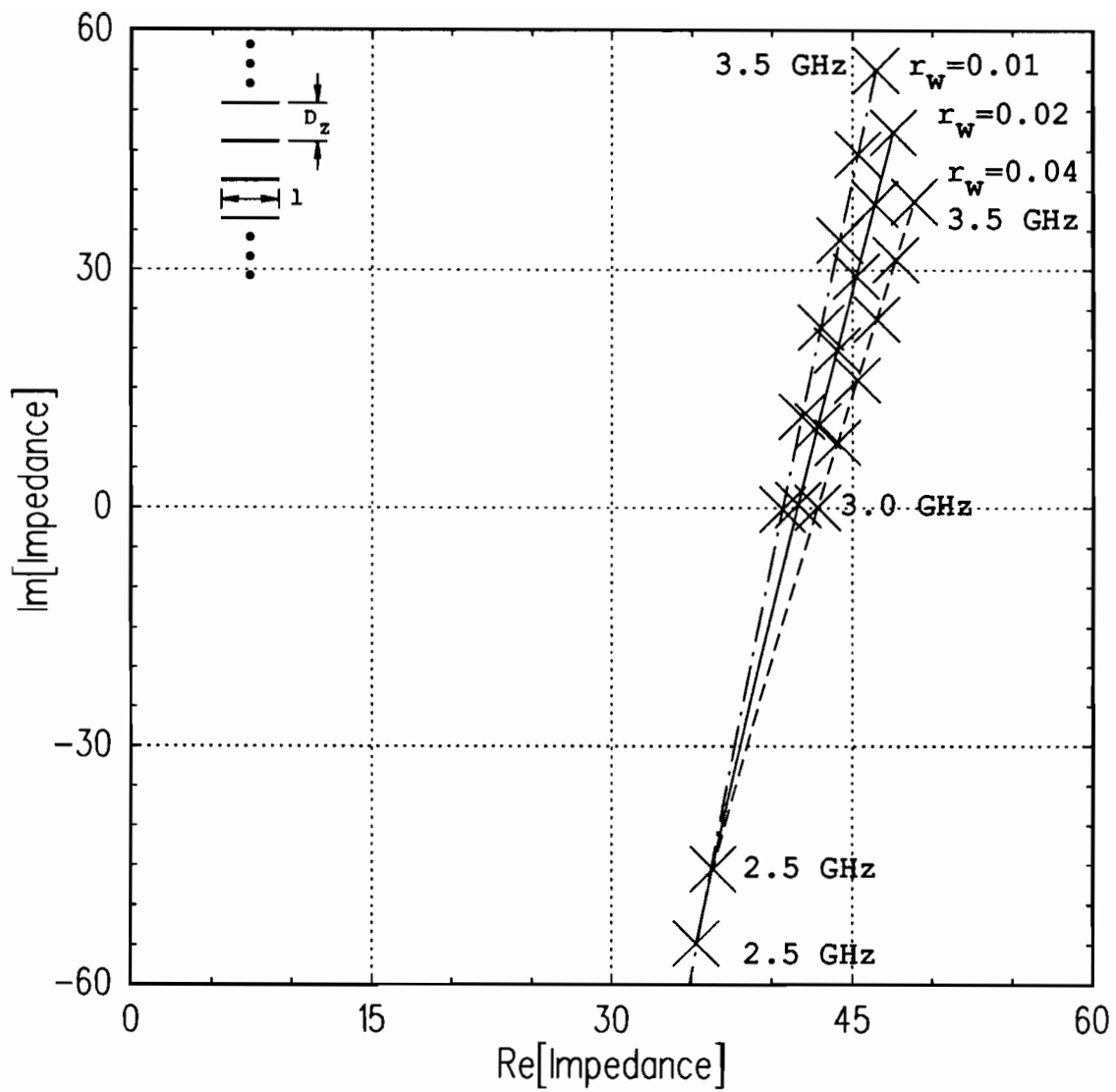
Figure 17: Scan impedance of a single column of uncoated transverse dipoles as the wire radius is varied.
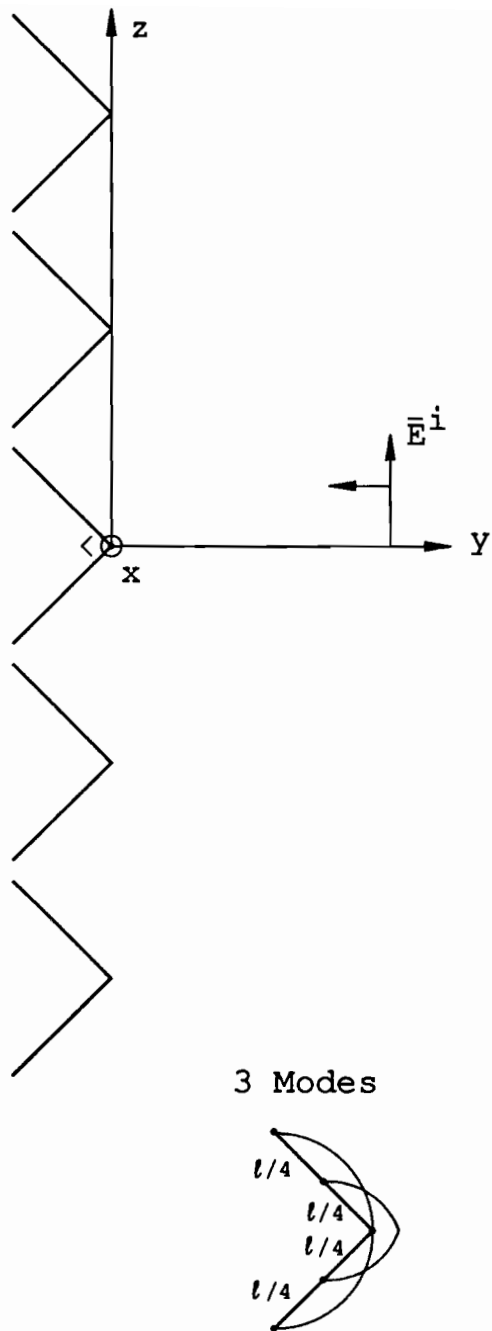
Figure 18: Single column of 90 degree bent dipoles with a dielectric coating.

45

Case	l (cm)	D_z(cm)	r_w(cm)	r_d(cm)	ϵ_{coat}	ϵ_{amb}
A	4.60	3.5	.02	NA	NA	1.0
B	4.31	3.5	.02	.04	4.0	1.0
C	3.96	3.5	.02	.08	4.0	1.0
D	2.30	1.75	.01	NA	NA	4.0
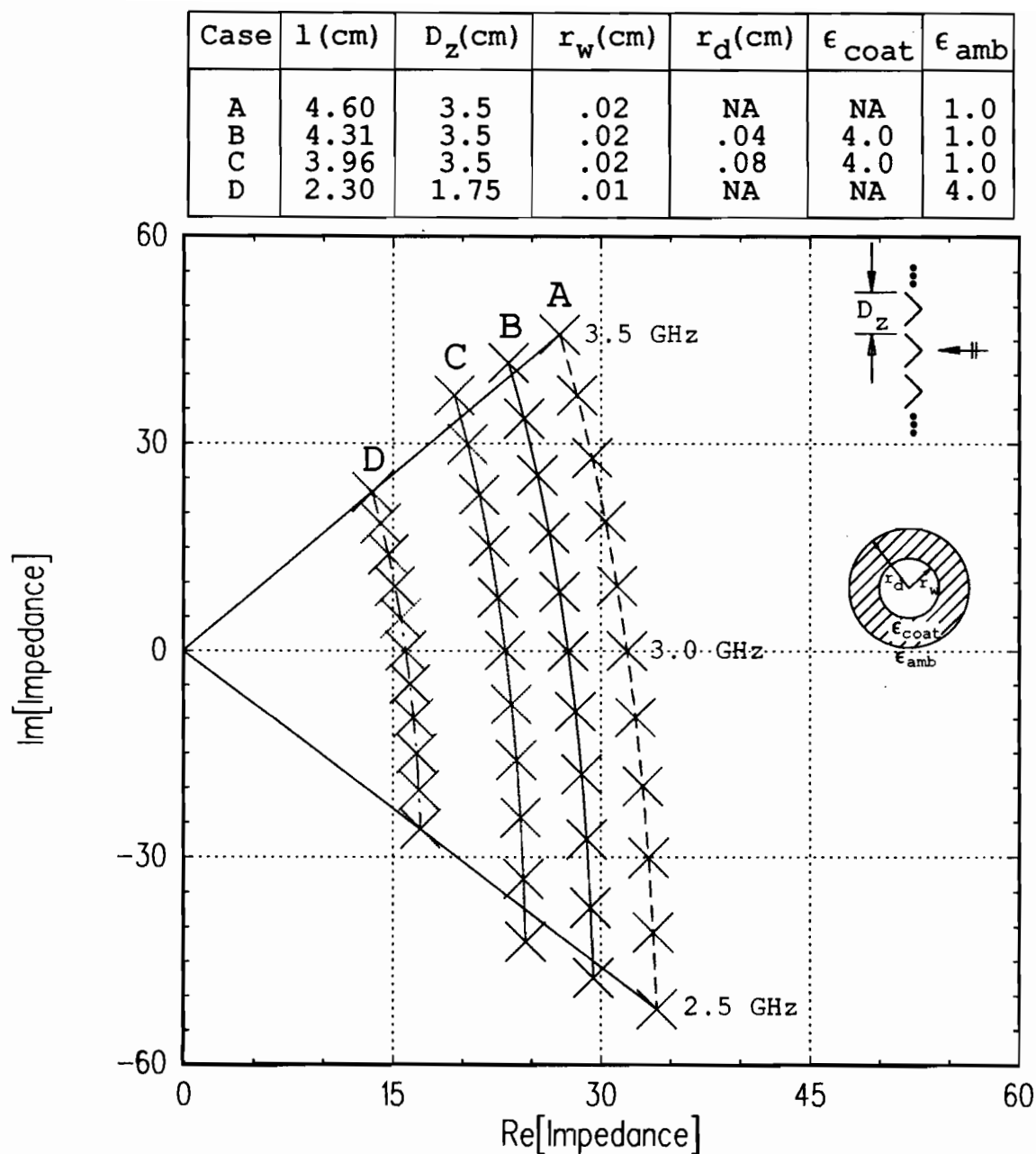
Figure 19: Scan impedance of a single column of 90 degrees bent dipoles with a dielectric coating for fixed D_z and edge-on incidence.

46

Case	l (cm)	D_z (cm)	r_w (cm)	r_d (cm)	ϵ_{coat}	ϵ_{amb}
A	4.60	3.5	.02	NA	NA	1.0
B	4.20	3.2	.02	.04	4.0	1.0
C	3.75	2.9	.02	.08	4.0	1.0
D	2.30	1.75	.01	NA	NA	4.0
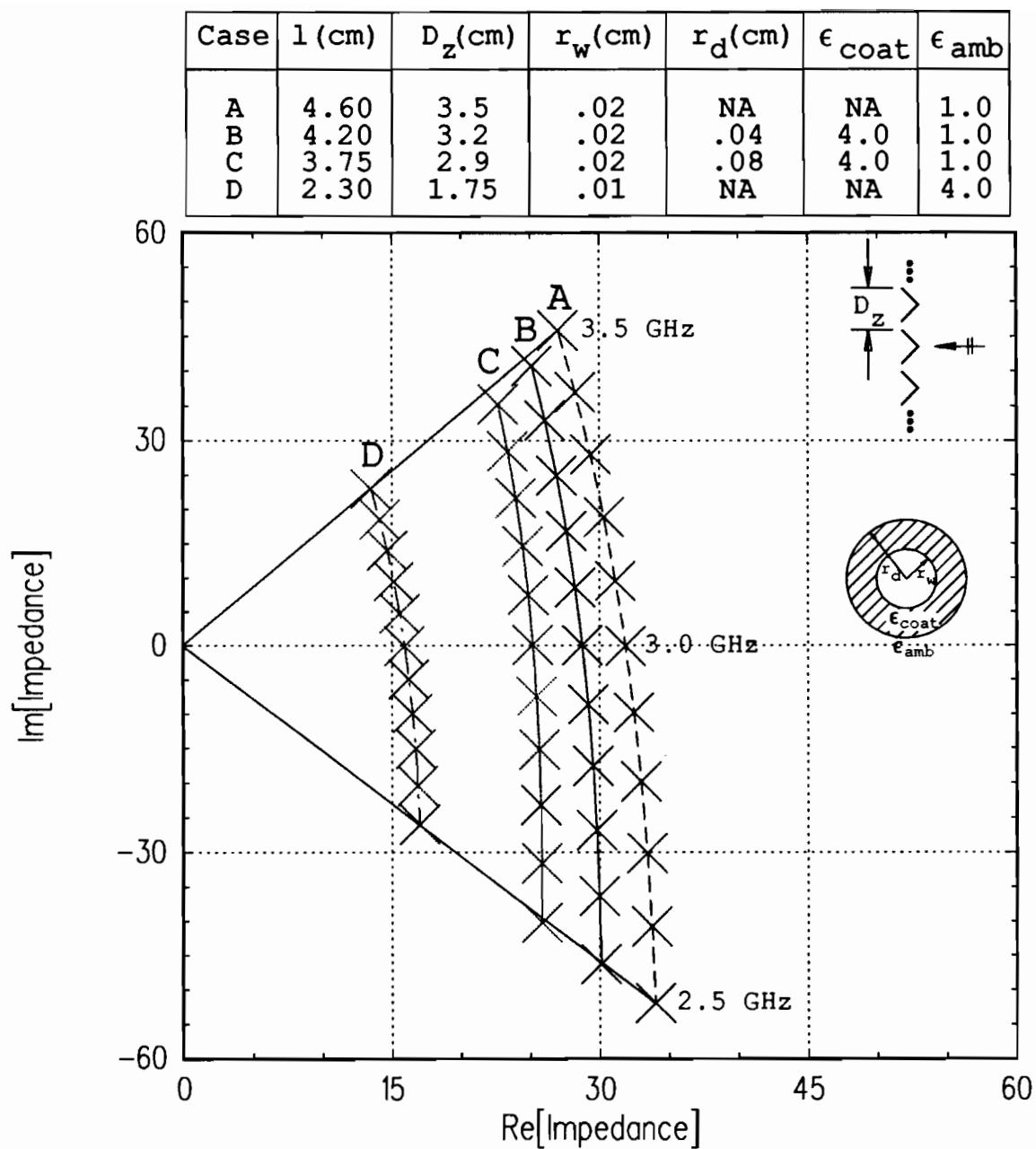
Figure 20: Scan impedance of a single column of 90 degree bent dipoles with a dielectric coating for variable D_z and edge-on incidence.
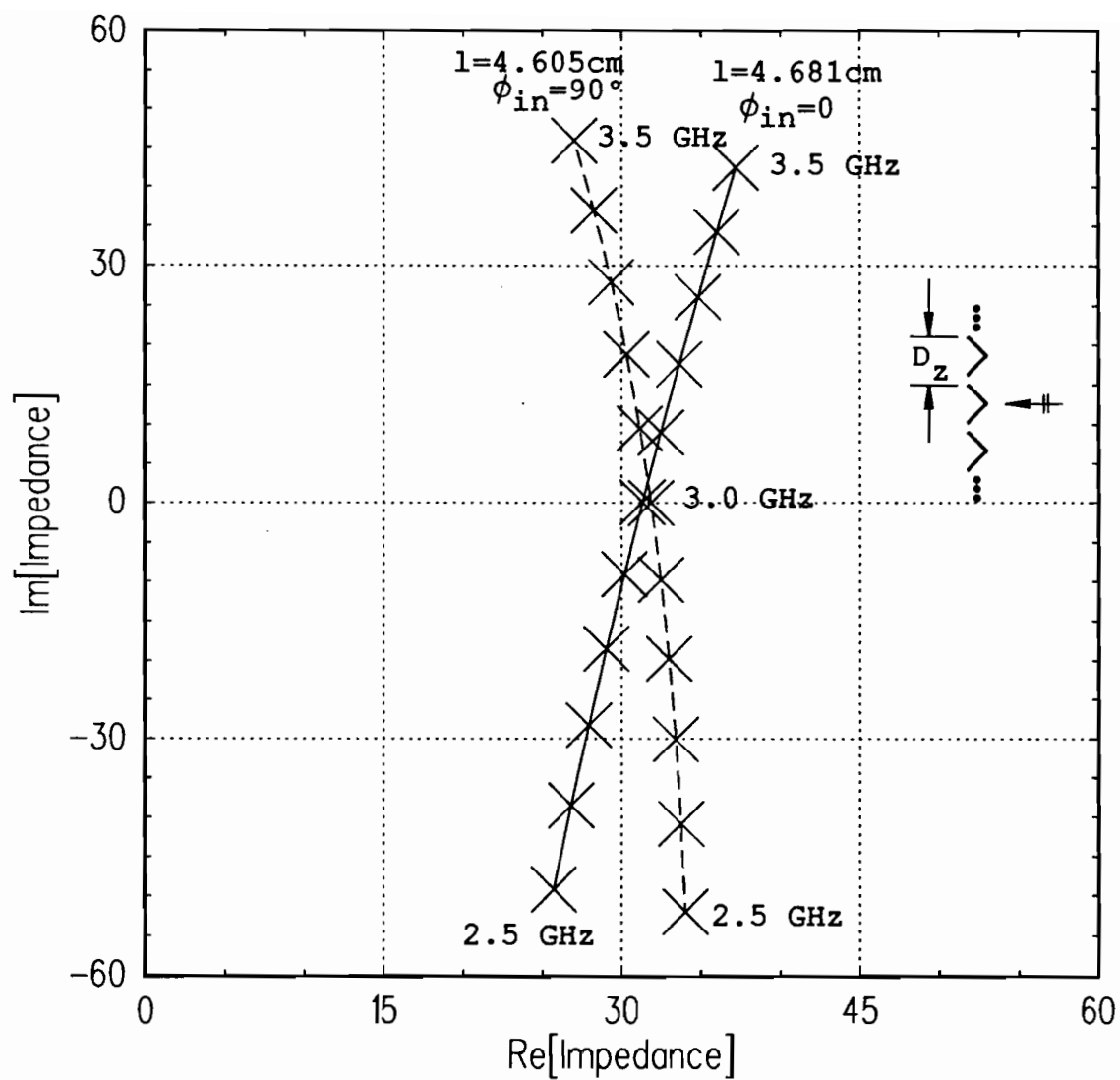
Figure 21: Scan impedance for a single column of uncoated 90 degree bent dipoles for edge-on (90 degrees) and broadside (0 degrees) incidence.

3.4 Square Loops

The next element chosen to be investigated is the square loop shown in Figure 22. This element combines the features of the axially oriented dipoles and the transverse oriented dipoles in a single element. In practice, loops are often chosen for their relative insensitivity to the polarization of the incident wave. These polarization characteristics however may suffer when the loop is not an isolated element or not a member of an array which is two-dimensionally infinite.

The scan impedance as seen at the center of a transverse side and as seen at the center of an axial side will be examined. This is accomplished by breaking the loop into 8 elements or modes as shown at the bottom of Figure 22. Two elements are highlighted and it is the scan impedance of these two elements that will be shown. The incident field is assumed to be a plane wave travelling in the $-\hat{y}$ direction which is orthogonal to the plane of the loops. If a constant spacing of $D_z = 3.0$ cm is held, it is not possible to have both modes resonate at the desired frequency of 3.0 GHz while maintaining a square shape. Figure 23 shows the scan impedance for the two modes for three different loop sizes. The top plot element dimensions are set to have the axially oriented mode resonate at 3.0 GHz. This results in a side length of 2.47 cm. The middle plot element dimensions are set to have the transverse mode resonate at 3.0 GHz, resulting in a side length of 2.73 cm. The bottom plot element dimensions are set to be halfway between the top and middle choice or 2.6 cm. This results in having the axial mode resonate below 3.0 GHz and the transverse mode above. These dimension choices result in the back scattered fields shown in Figure 24. The top plot gives the backscattered fields versus frequency for a plane wave incident normal to the plane of the loops with polarization along the array axis or theta direction. The bottom plot is under similar conditions except for the polarization
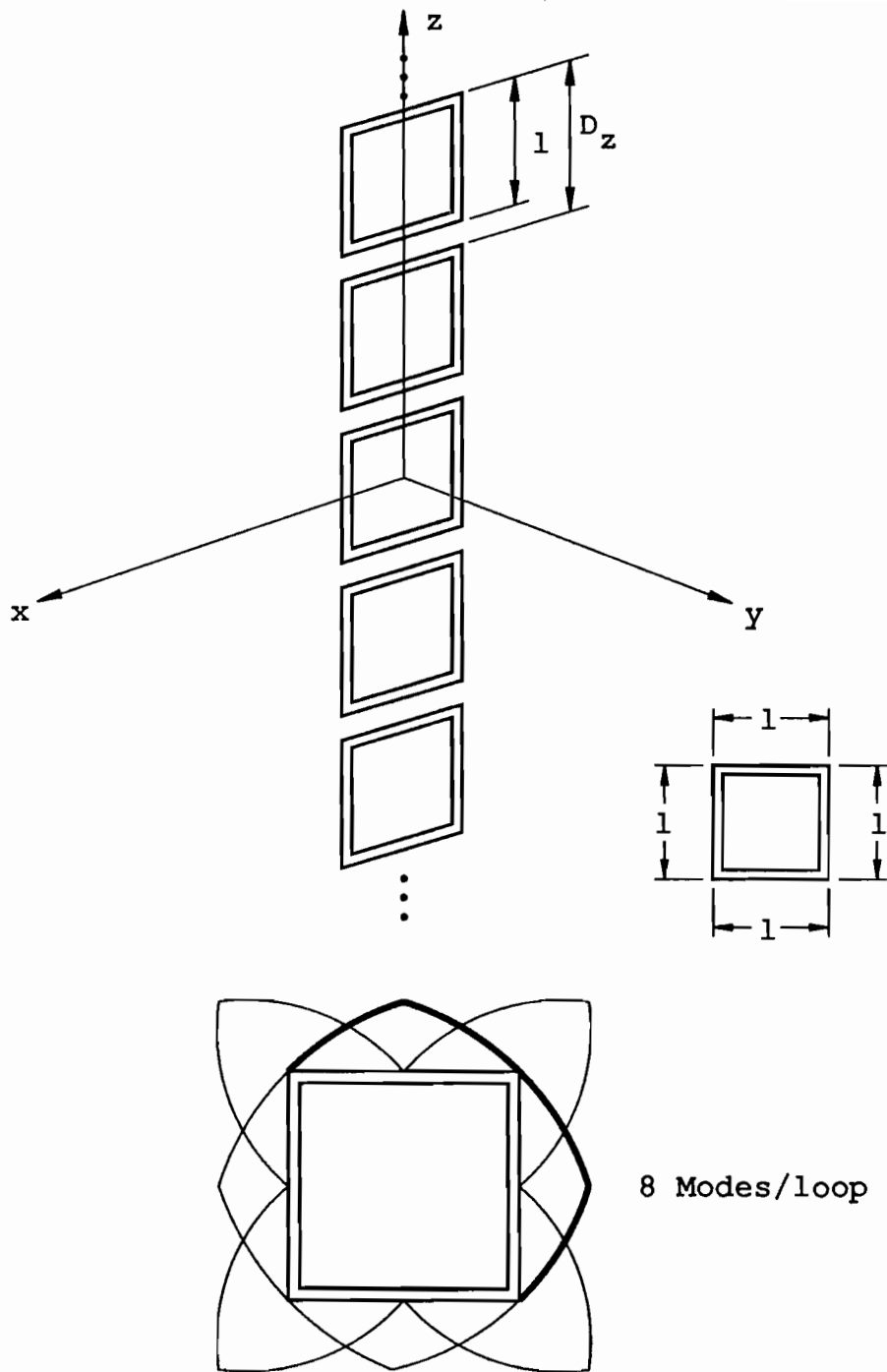
Figure 22: Single column of square loop elements.
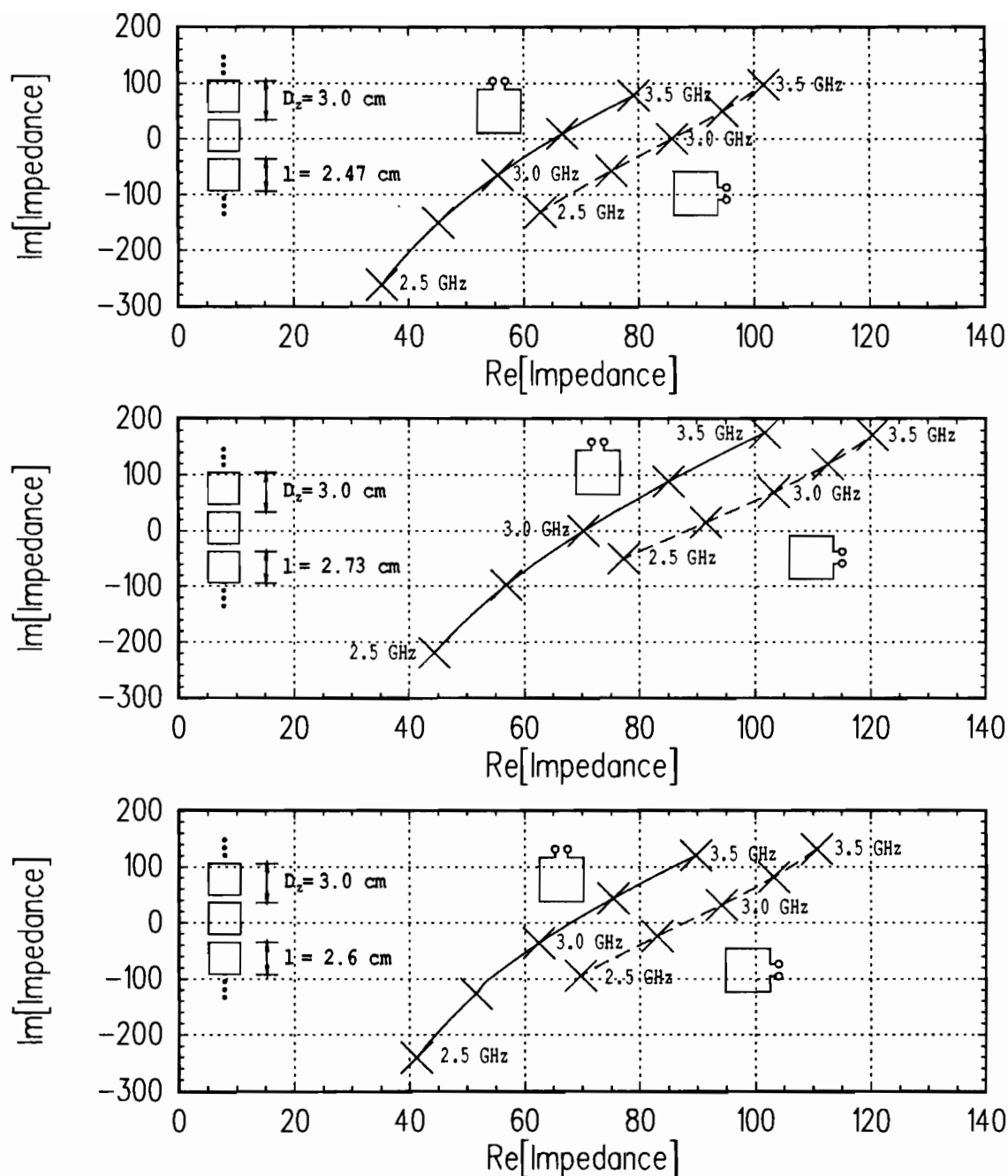
Figure 23: Scan impedance for axial and transverse modes on a single column of uncoated square loops. Top: side length = 2.47 cm. Middle: side length = 2.73 cm. Bottom: side length = 2.6 cm.
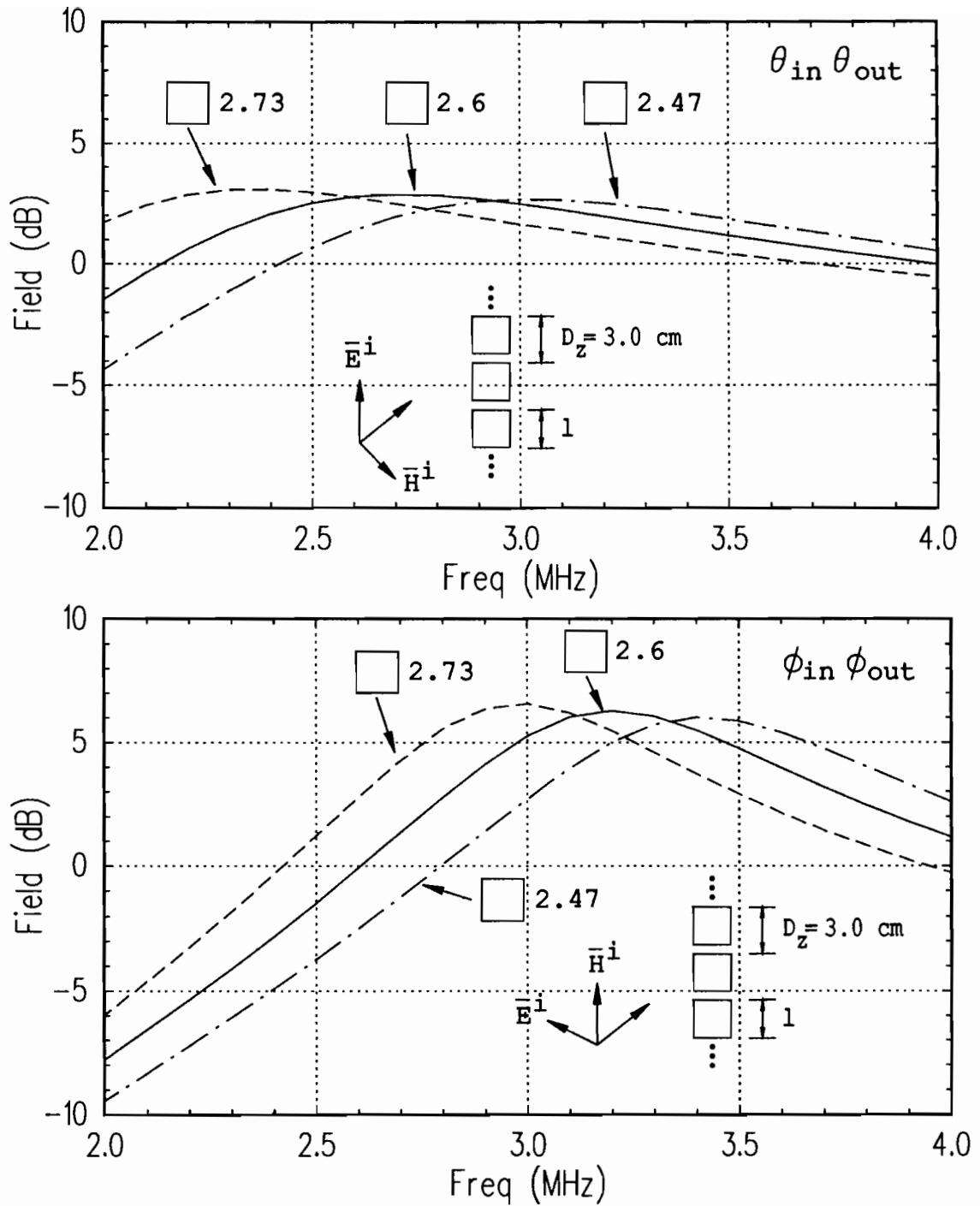
Figure 24: Backscattered field versus frequency for a single column of square loops with the side lengths as shown. Plane wave incidence broadside to the loops with θ polarization on top and ϕ polarization on the bottom.

now being in the phi direction. As expected, the smallest loop peaks at 3.0 GHz for theta polarization, the largest loop peaks at 3.0 GHz for phi polarization and the middle sized loop peaks between the other two. It is also noted that scattered field magnitude is higher for phi polarization. This is also seen in comparing the scattered fields from a column of axially oriented elements to those transverse. A column of axial elements does not have as large of a physical or electrical cross section as a column of transverse elements resonant at the same frequency. This is verified in comparing Figure 9 to Figure 15. For square loops, the physical cross section is obviously the same but apparently the electrical cross section is smaller for theta polarization than for phi polarization.

Choosing a square element with a length between what was determined above for theta and phi polarization is one possible compromise. Another might be to alter the shape of the loop from square to rectangular. The loop sizes above suggest that lengthening the transverse side and shortening the axial side might yield the desired results. Figure 25 repeats the results in Figure 24 and adds the results for a rectangular loop that is 3.2 cm long on the transverse side and 2.2 cm long on the axial side. For theta polarization, the peak is now closer to the desired resonant point of 3.0 GHz and the scattered field magnitude has increased, at the price of a loss in bandwidth. For phi polarization, the peak has not moved significantly from that of the 2.6 cm square loop and the magnitude has increased only slightly, but the bandwidth is seen to increase.

These results are consistent with the previous results for straight axial and transverse dipoles. For theta polarization, placing the axial components farther apart increases the effective cross section; shortening the axial component raises the resonant frequency; and increasing the gap between elements lowers the bandwidth. For phi polarization, increasing the length of the transverse component increases the

53
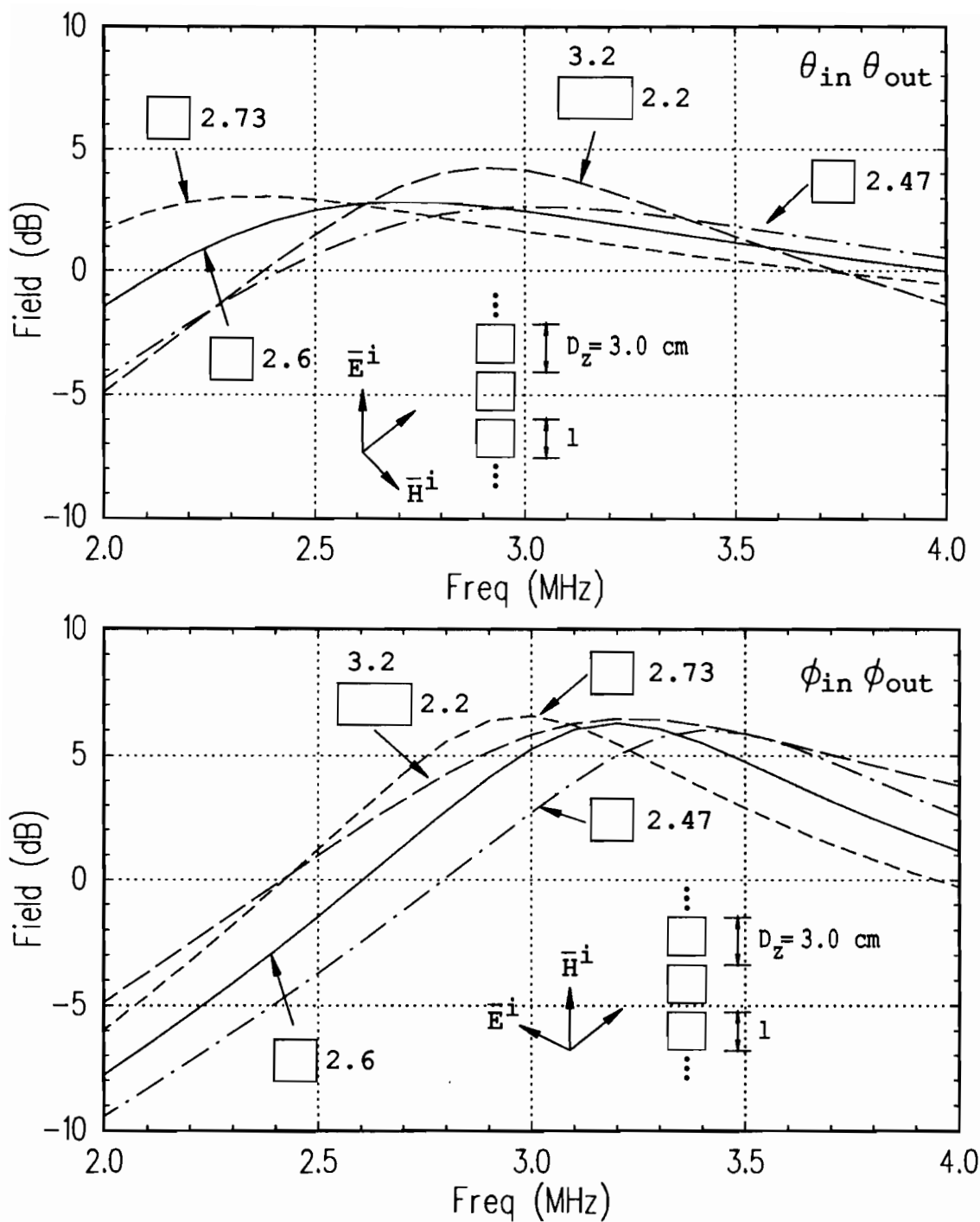
Figure 25: Backscattered field versus frequency for a single column of square loops of various sizes and a rectangular loop. Plane wave incidence broadside to the loops.

54

effective cross section slightly and increases the element to element coupling more so than the wider gap decreases it. The greater coupling and increase in length effectively cancel each other in regard to shifting the resonant frequency but an increase in bandwidth results.

In varying the lengths of the rectangle's sides, it becomes apparent that altering one length affects the results for both polarizations. The rectangle can be made still wider and shorter, yielding peak fields that are closer between the two polarizations, but this will result in a greater disparity between the bandwidths of the two polarizations.

Another possible method for reconciling the resonant frequency difference between the two polarizations may be to add a dielectric coating to two of the loop legs. Lengthening the transverse legs and shortening the axial legs was shown above to yield improved results, so a natural inclination might be to put a coating on the transverse legs of the smaller square loop with $l = 2.47$ in the preceding plots, thus having "electrically larger" transverse legs and appropriate length axial legs. This will not provide the desired results, however, if only a thin dielectric coating is used. A better choice is to use the small, $l = 2.47$ cm, square loop but coat the axial legs.

Figure 26 shows the backscattered field versus frequency for an uncoated square loop ($l = 2.47$ cm), the same loop with its axial legs coated and the same loop with its transverse legs coated. The coating has a radius of .08 cm with a relative dielectric constant of 4.0 on a wire that is .02 cm in radius. The angle of incidence is broadside to the plane of the loops and the results for both co-polarizations are given. Coating the transverse legs shifts the curve slightly lower in frequency for phi polarization, which is in the desired direction, but it shifts the curve substantially lower for theta polarization which was not desired. Coating the axial legs shifts the curve slightly
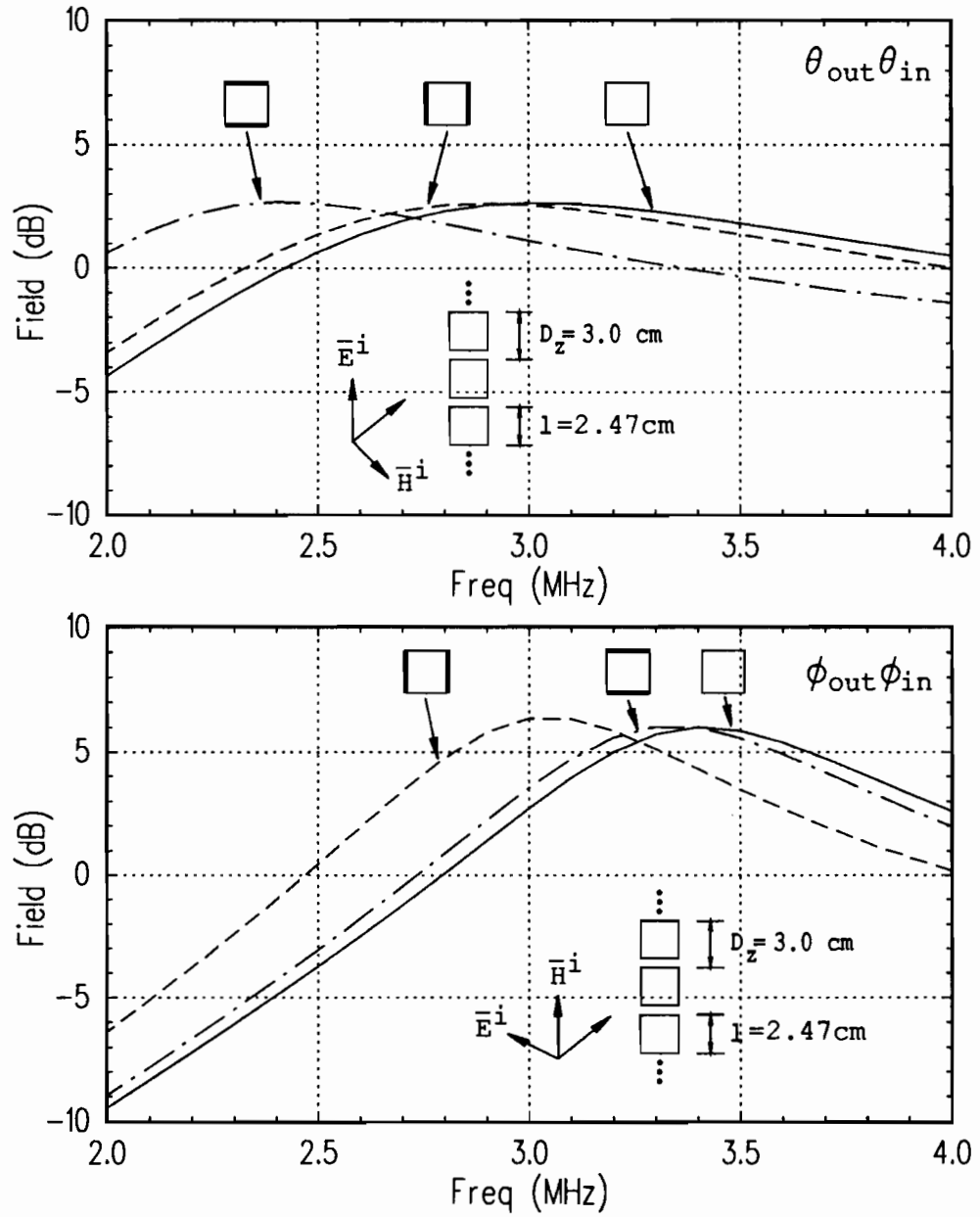
Figure 26: Backscattered field versus frequency for a single column of square loops that have two legs coated with dielectric.

56
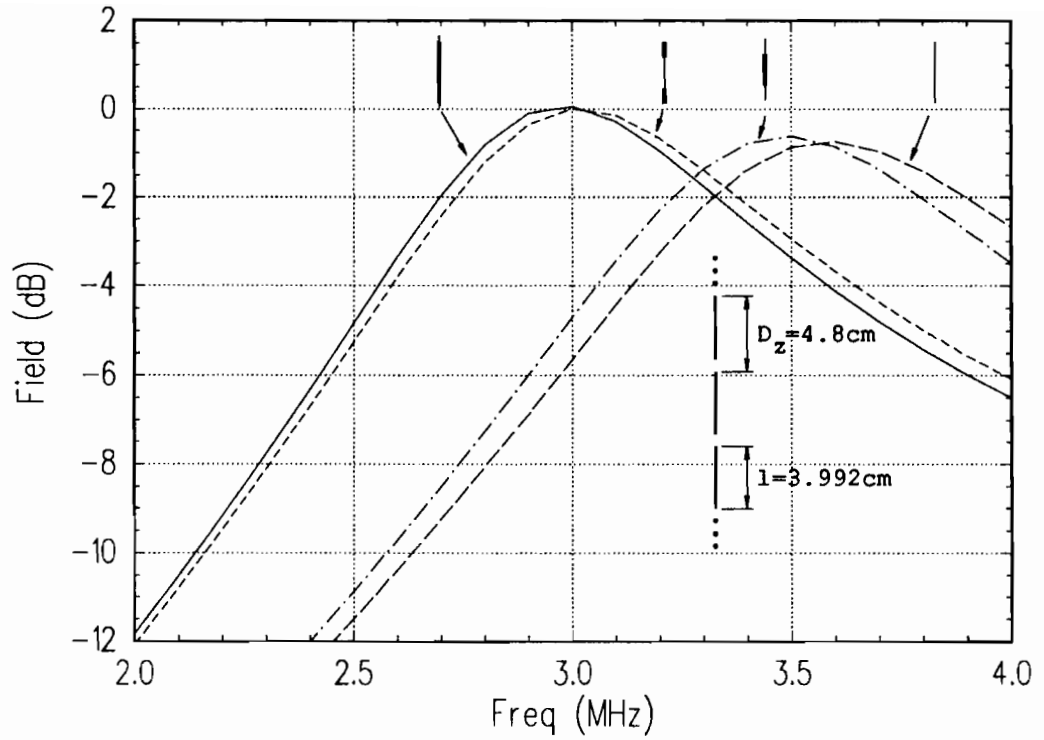
Figure 27: Backscattered field versus frequency for a single column of coated axial dipoles.

lower for theta polarization and shifts the curve substantially lower to the desired frequency for phi polarization.

To discover why this seemingly counter-intuitive result arises, it is helpful to return to the simpler case of straight axial elements. Figure 9 shows results for coated wires. The curve for the $l = 3.992$ coated wire is repeated in Figure 27 and three additional cases are included. One is for an uncoated wire, which peaks around 3.6 GHz; one is for an element that is coated over a length $l/2$ in the center of the element, which peaks near 3.5 GHz; and the last one is for an element that has a length $l/4$ coated on each end, which has a peak near 3.0 GHz. The parts of the coating near the ends of the dipole are seen to have the biggest effect of lowering the

frequency at which the peak occurs. This is a result of the coated thin wire model given in Appendix G which shows that for this case where a piecewise sinusoidal basis function is used, the coating results in a significant capacitive load on the end modes and a much smaller capacitive load on the center element. Applying the above results to the square loop, it is now seen that applying a dielectric coating to the axially oriented legs is equivalent to loading the center of the axially oriented straight dipole for theta polarization and equivalent to loading the ends for phi polarization.

Figure 28 shows backscattered field vs. frequency comparing the midsized square loop, rectangular loop and loaded small square loop for co- and cross-polarizations. No cross-polarization curves are seen for the loaded square loop as they are below -80 dB. The rectangular and loaded square loops are both seen to be superior to the midsized square loop but the choice between those two options would depend upon design criteria and construction concerns.

3.5   Chapter Summary

This chapter concentrated on the effects of coupling within a single column of elements and the effects of dielectric coatings. For straight axially oriented dipoles it was seen that minimizing the interelement spacing, D_z, results in increased bandwidth and shorter elements. For straight dipoles transverse to the array axis, the bandwidth increases as the interelement spacing decreases but the elements became longer. For both axial and transverse elements, increasing the wire radius results in a smaller variation of the imaginary part of the scan impedance with frequency and an increased variation of the real part. For axial elements, increased wire radius requires shorter elements to maintain a resonant frequency and for transverse elements the length must be increased.
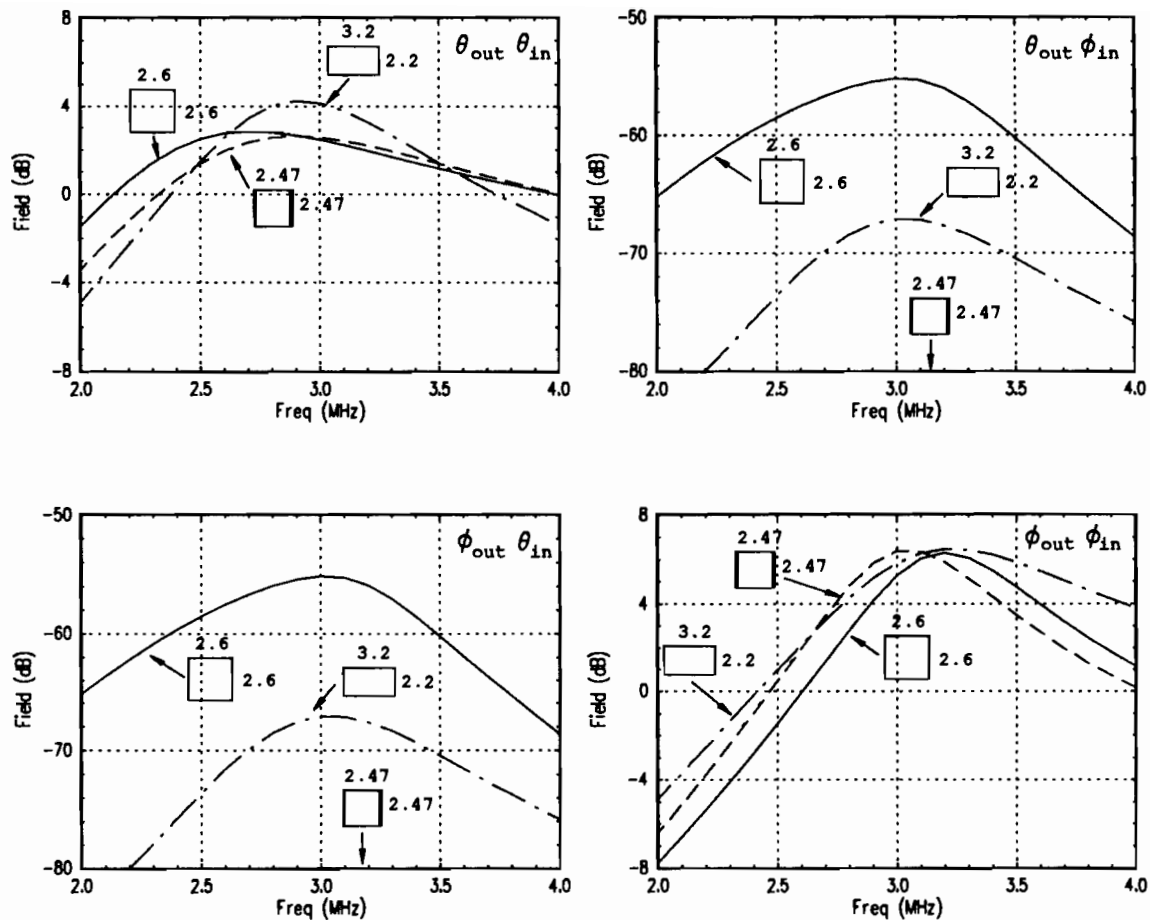
Figure 28: Backscattered field versus frequency for a single column of square loops, rectangular loops and loaded square loops. Includes both co- and cross-polarizations.

59

An array of dipoles bent at 90 degrees lying in the y-z plane was seen to react to interelement spacing variation much the same as axially oriented straight dipoles for a plane wave incident along the y axis. The slope of the scan impedance curved in the complex plane goes from positive to negative as the angle of incidence goes from along the x axis, or broadside to the plane of the bent dipoles, to along the y axis, or edge on to the array of bent dipoles.

An array of square loops was examined next. Square loop elements exhibit characteristics of both axial and transverse elements and couple both aspects together. It was shown that a column of square loops with identical sides has a resonant frequency that is dependent upon the polarization of the incident wave. This can be compensated for by making the loops rectangular or by placing a dielectric coating on the axially oriented legs.

The effect of placing a thin dielectric coating on a thin wire element was shown. The net result is that the element length is decreased to maintain resonance. It is further shown that this end result comes about via capacitive loading which is strongest near the ends of the resonant length. This should be distinguished from increasing the electrical length of the element uniformly along the coated length due to a change in propagation constant. If the latter were true, the positioning of a partial coating along the wire length would not affect the results, but it was shown that was not the case.

The above information is important in its own right for single column designs but it is also of use in designing with multiple columns, as for example in designing a finite planar array. The columns at the edge of a finite array are in a different environment from those in the center and some of the attributes unique to single columns of elements will start to appear at the edge. A square loop in a square grid will respond to both polarizations equally in the center of a large array, but those

60

elements at the edge of the array will not. A straight dipole length that was set in the center of the array to be resonant at a given frequency will yield resonance at a different frequency for edge elements. The study of single columns of elements provides clues as to what the proper course of action to take may be.

CHAPTER IV

Truncated Frequency Selected Surfaces

In the design of an FSS it is commonly desirable to have the surface be highly reflective in one frequency band and highly transmissive in another. When the surface is highly reflective it should have the characteristics of a solid conductor and hence the truncated FSS should then resemble a conducting strip. To test this hypothesis, the scattering from several simple geometries will be found and compared to three approximate solutions.

The first approximation will maintain the array geometry but the currents on the elements will be forced to match those of a two dimensionally infinite surface. The currents will in actuality be found using PMM [10] with a linear phase taper added for incidence angles other than broadside. The second approximation will be to use a diffraction solution for a solid PEC strip. UTD diffraction coefficients will be used and only first order diffractions will be considered. The third approximation will be a physical optics (PO) solution for a PEC strip.

The arrays will be composed of straight perfectly conducting wires with a radius of .02 cm. Unless otherwise noted, the wire lengths have been adjusted such that they resonate at 3.0 GHz when in a doubly infinite grid. The arrays are infinite in the z direction and bistatic patterns in the x-y plane are given for incident angles of 90 degrees (broadside), 45 degrees and 30 degrees.

The UTD and PO results have been normalized such that the peak value of the UTD curve matches that of the rigorous solution (Trunc) and the PO results have

been normalized to the forced uniform current approximation (Inf). The plotted results will be distinguished by the line type; Trunc = solid, UTD = dot-dash, Inf = short dash, and PO = long dash.

4.1 Axially Oriented Dipoles

The first geometry under consideration is shown in Figure 29. It consists of 31 columns of axially oriented straight dipoles spaced 3 cm apart for a total width of 90 cm or 9 wavelengths at 3 GHz. The elements are numbered from 1 to 31 with 1 being the trailing edge and 31 being the leading edge for incidence angles less than 90 degrees.

The resulting current magnitudes are shown in Figure 30. At broadside the currents are very similar between Trunc and Inf except for the currents near the edge. At 45 degrees incidence the overall current level is lowered and elements farther in from the leading edge (element 31) vary. As the incident angle is lowered to 30 degrees the overall current is again lowered and elements farther yet into the array appear to vary. It should also be noted that the current "flips" from decreasing in magnitude at the leading edge for broadside incidence to increasing in magnitude at the leading edge at off angles.

To see the impact of these current variations, the bistatic scattered fields are calculated and plotted in Figure 31 along with the Inf, UTD and PO approximations.

The top plot in Figure 31 shows the results of the four solutions for 90 degrees incidence (broadside). The Trunc and UTD results are virtually indistinguishable under these conditions as are the Inf and PO curves. The Inf and PO approximations both assume uniform currents across the array and it is therefore not surprising that they track one another. The Trunc and Inf curves vary in that the nulls are
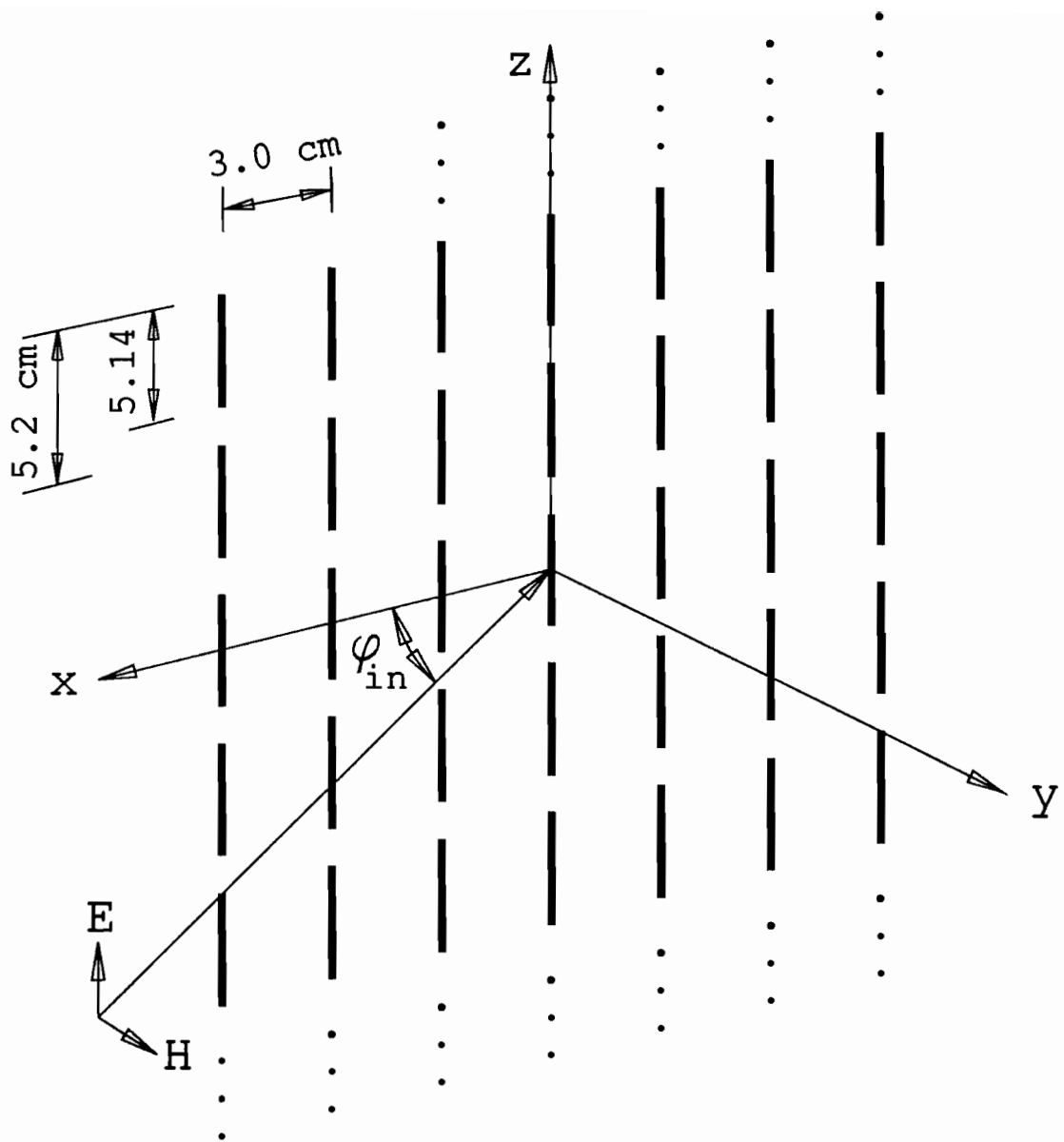
Figure 29: Array of axially oriented dipoles.
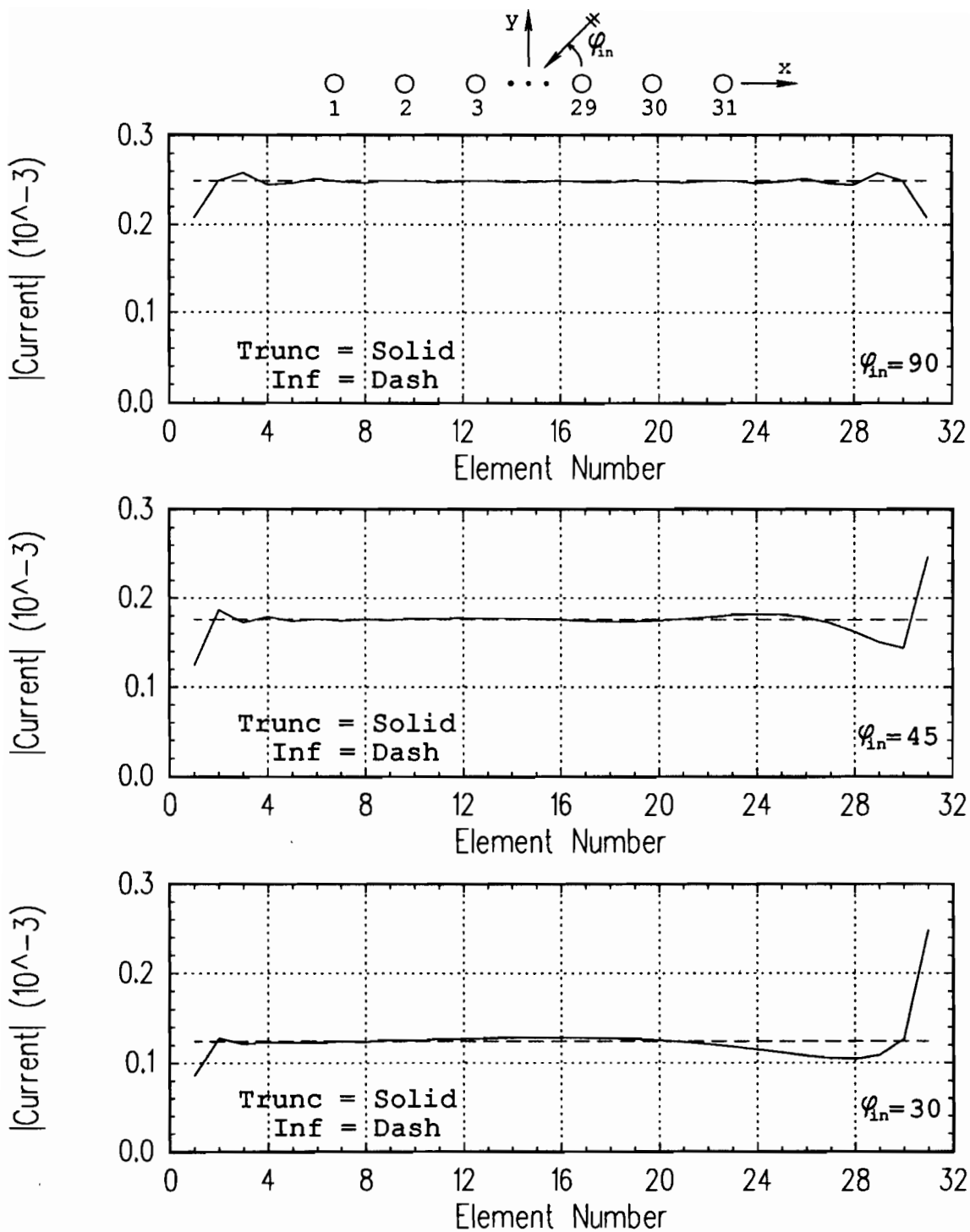
Figure 30: Axial dipole array currents — freq = 3.0 GHz, 31 columns, width = 90 cm = 9.0λ.

65
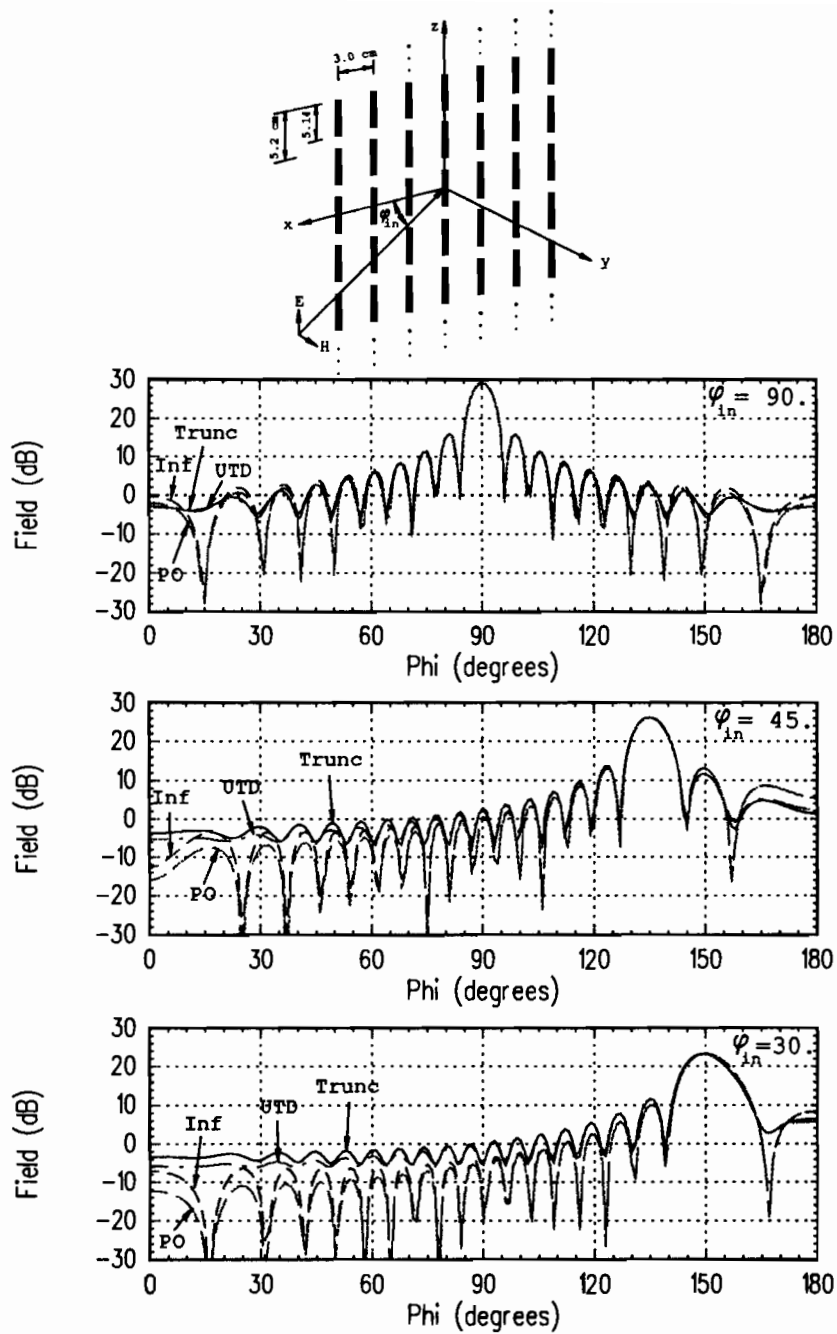
Figure 31: Bistatic scattering pattern — freq = 3.0 GHz, array of 31 columns, width = 90 cm = 9.0λ, UTD strip = 9.15λ, PO strip = 9.3λ.

66

not as pronounced in Trunc as in Inf and close examination of the null locations appears to indicate that the Inf array is effectively slightly larger. These observations correspond to having an array with a uniform current distribution (Inf) and an array with a distribution that is tapered at the edge (Trunc). The array apparently quite closely resembles a solid strip when at resonance with broadside incidence. The width of the strip however is in question. The strip width was varied until the strip scattering solution lobing structures matched those of the array. The resulting strip width proved to be 9.15 wavelengths for the UTD case and 9.3 wavelengths for the PO case. Both of these indicate a width wider than the actual physical width of 9 wavelengths, as one would expect from physical reasoning.

As the angle of incidence is decreased, the Trunc and Inf solutions diverge more as was to be expected from examining the currents. The UTD solution however still yields a very respectable approximation down at 30 degrees incidence even though only single diffraction terms have been retained.

The array is now reduced to only 11 columns for a total width of 3 wavelengths retaining the geometry given in Figure 29. The currents are now as seen in Figure 32. Greater variation is seen between the Trunc and Inf cases across the array but the trends are the same as in the 9 wavelength case. To make the comparison between the 3 wavelength wide case and the 9 wavelength wide case more readily apparent, Figure 33 is a plot of the Trunc currents for the 11 column case (solid), the left most (trailing edge) 6 columns of the 31 column case (dotted), and the right most (leading edge) 6 columns of the 31 column case (dot-dash). (Note that the element numbers indicated for the leading edge columns of the larger array are no longer correct on this plot.) The only variation is for those elements toward the middle on the trailing edge for angles off of broadside. For a strip width of 3 wavelengths the trailing edge

67

appears to have no effect on the leading edge for this polarization and the leading edge's effects do not appear to extend all of the way to the trailing edge.

The resulting bistatic scattering patterns are shown in Figure 34. These results pretty much track those given for the 9 wavelength case, but one other variation is now seen. The angle at which the scattered field peak occurs is now seen to be slightly different between Trunc and Inf at 45 and 30 degrees incidence. Note however that the UTD approximation still holds up quite well, even including the scattered peak shift. The equivalent UTD strip width is 3.18 wavelengths and the equivalent PO strip width is 3.3 wavelengths for this case.

4.2 Transversely Oriented Dipoles

The next geometry under consideration is shown in Figure 35. It is made up of 33 columns of transverse straight dipoles in a triangular grid with a total width of 94.2 cm tip to tip. The grid was changed from rectangular to triangular to alleviate grating lobe problems.

The resulting current magnitudes are shown in Figure 36. The element numbers now seem to indicate a larger array than was stated. The reason for this is that it is necessary to have three modes per element for this polarization to allow for phase variation across the element as the angle of incidence varies from broadside. Thus the first dipole of the array consists of elements 1, 2 and 3. The second dipole of the array consists of elements 4, 5 and 6. This continues to the 33rd dipole being made up of elements 97, 98 and 99. What is shown in Figure 36 is a plot of the magnitude of the center element of each dipole, i.e. the current magnitude of elements 2, 5,..., 98 are plotted. (A comparison was made between one and three modes for the axially

68
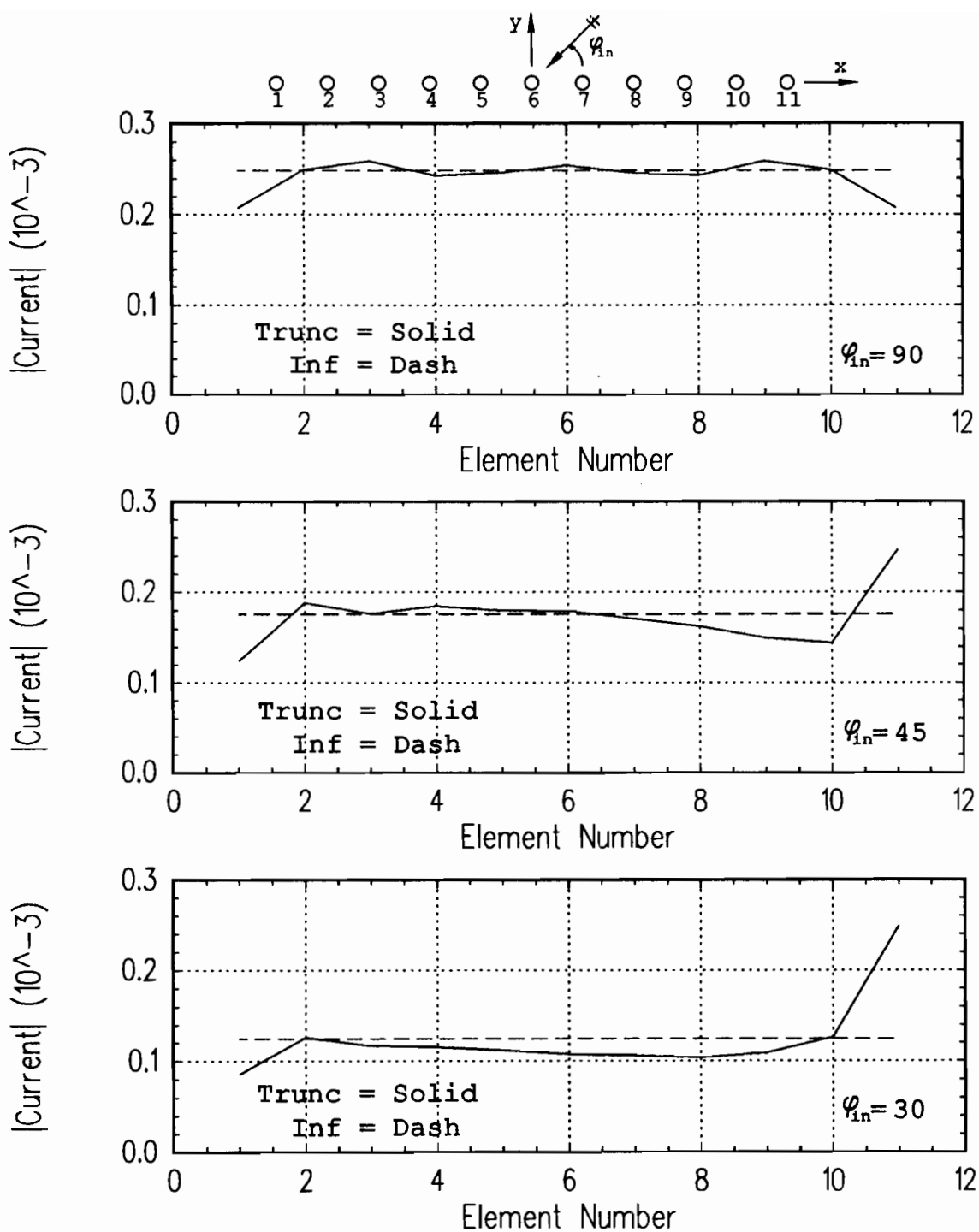
Figure 32: Axial dipole array currents — freq = 3.0 GHz, 11 columns, width = 30 cm = 3.0λ.

69
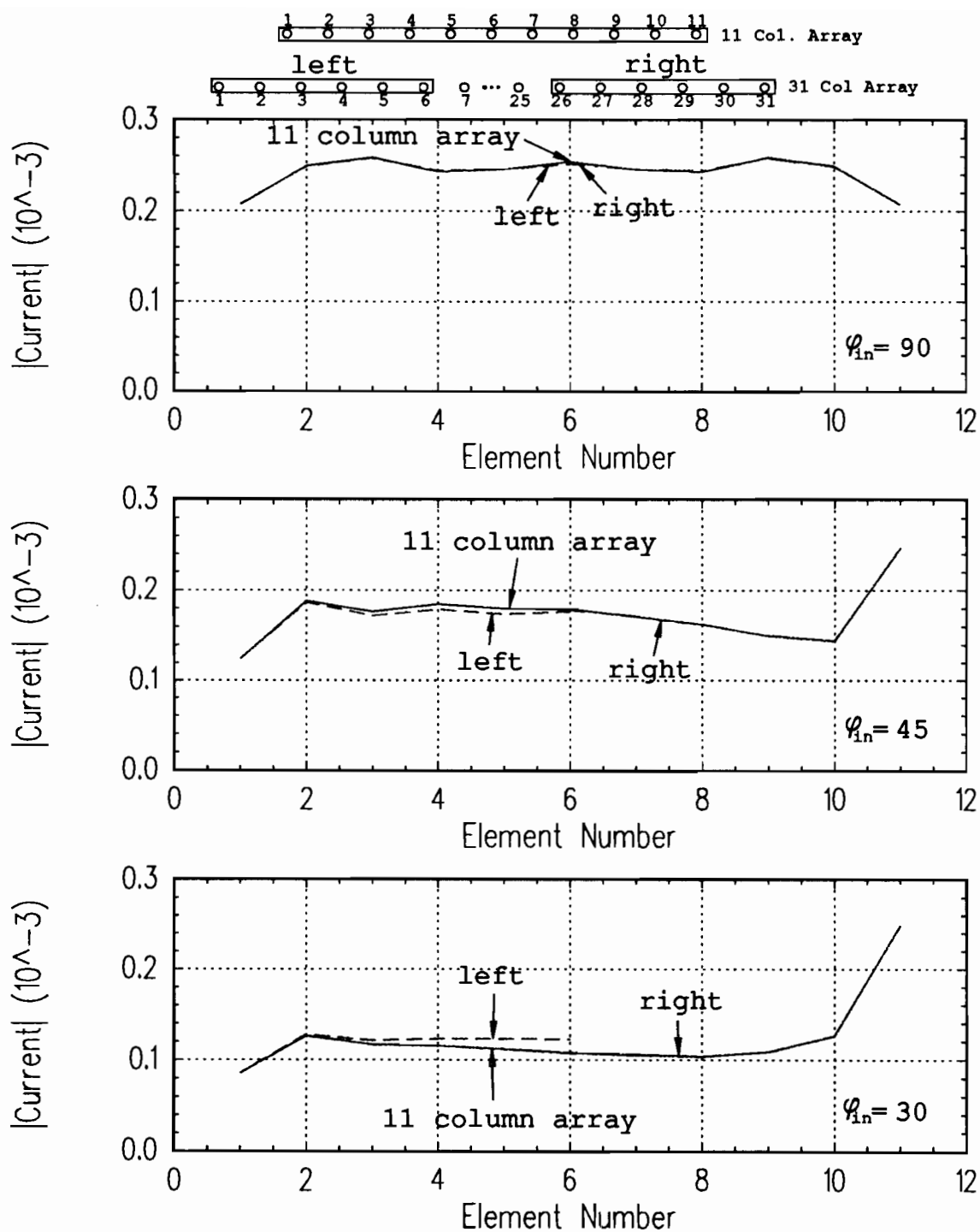
Figure 33: Axial dipole array currents — freq = 3.0 GHz, 11 columns vs. edge columns of 31 element array, left = 6 columns on the trailing edge, right = 6 columns on the leading edge of the 31 column array.

70
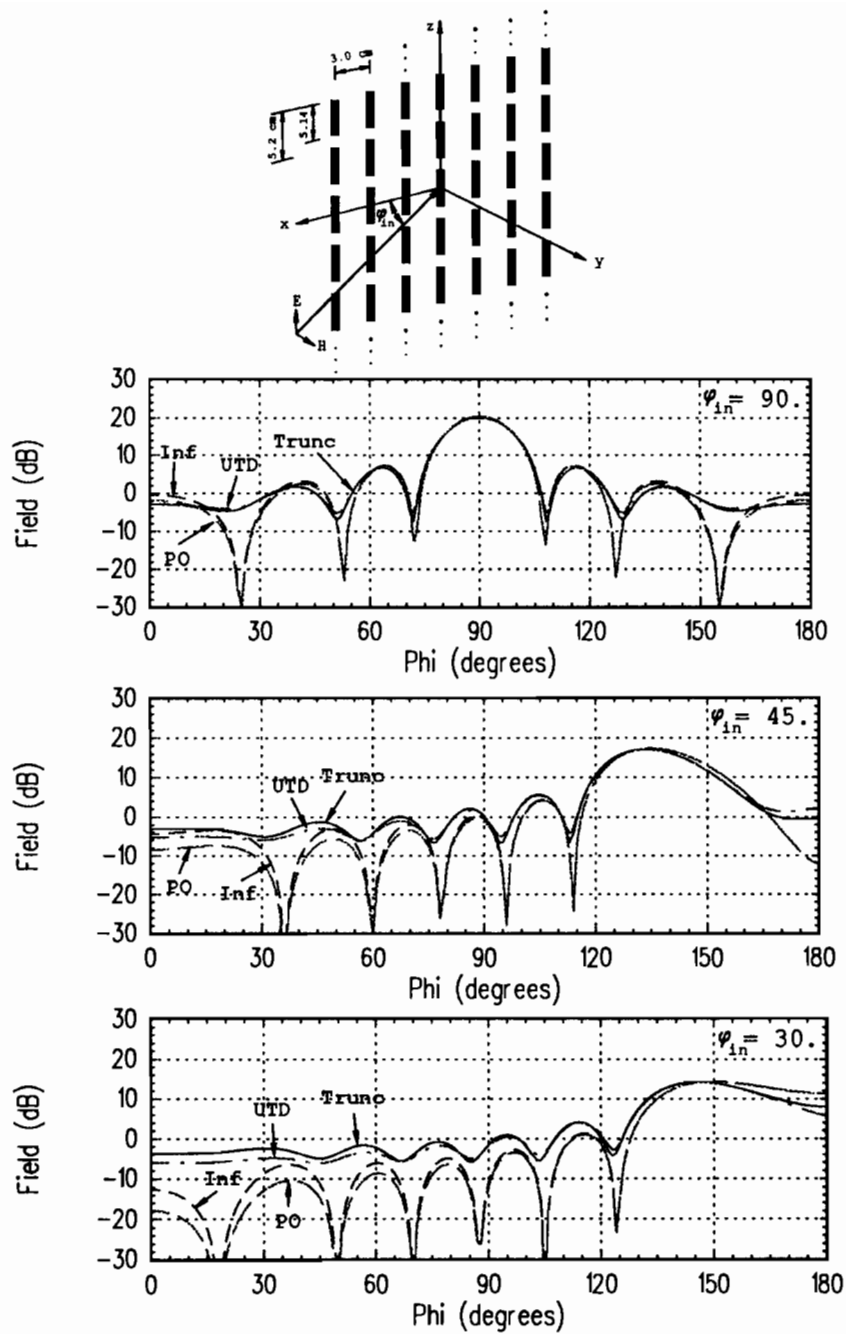
Figure 34: Bistatic scattering pattern — freq = 3.0 GHz, array of 11 columns, width = 30 cm = 3.0λ, UTD strip = 3.18λ, PO strip = 3.3λ.
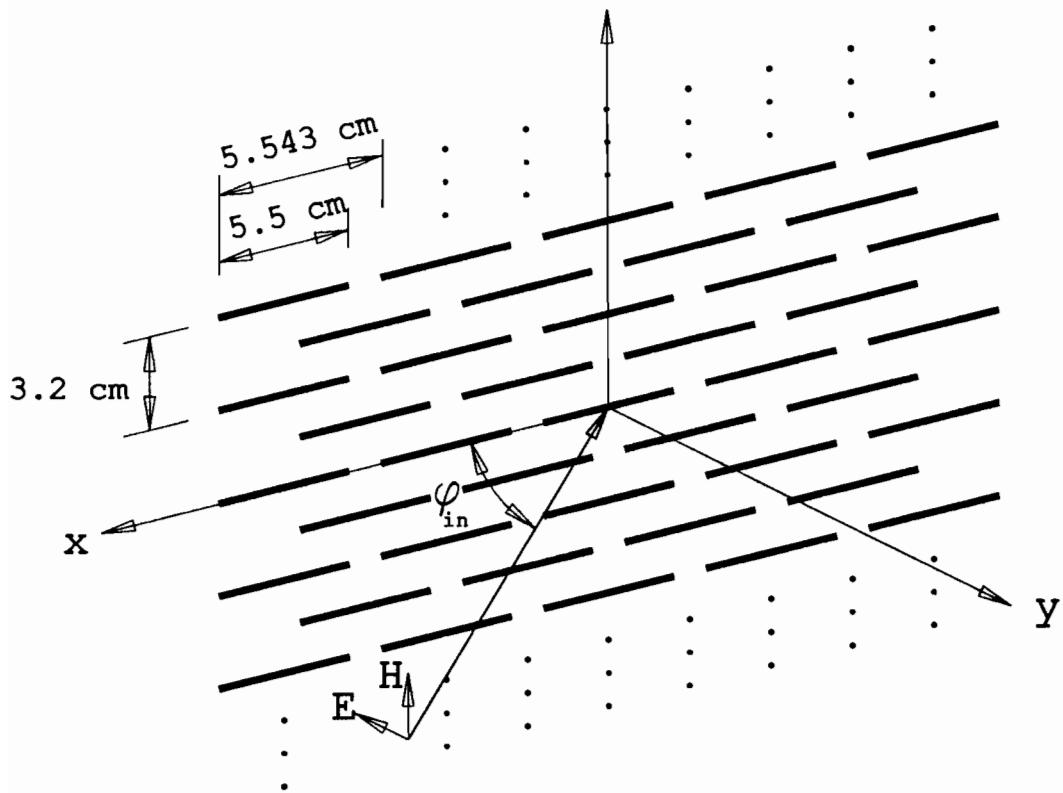
Figure 35: Array of transversely oriented dipoles.

oriented case and no difference was seen between one and three modes for any scan angle provided the dipoles stayed at their resonant frequency.)

At broadside the currents are again very similar between Trunc and Inf except for those near the edge. Now, however, the current increases at the edge of the array whereas it decreased for the axially oriented case. At 45 degrees incidence the overall current level is higher than it was at broadside and both the leading (element 98) and trailing (element 2) edge currents are altered. The currents at the leading edge are elevated and vacillate more. The Trunc current at the trailing edge now "flips" from being higher than Inf to being lower. As the incidence angle is lowered to 30 degrees the overall current level now lies between that for 90 degrees and that for 45 degrees. The trailing edge currents drop lower yet and the leading edge currents vary farther into the array.

The following overall trends are appearing. The trailing edge is affected more with polarization TE to the array axis (which coincides with physical observations of plate scattering). The current level decreases as the incidence angle goes toward grazing for the axially oriented dipoles and increases for the transversely oriented dipoles. This rule is apparently violated above for the transverse dipoles in going from 45 degrees incidence to 30 degrees incidence but the whole story was not told above. Figure 37 is a plot of the reflection coefficient for two dimensionally infinite arrays of dipoles versus frequency for the angle of incidence of interest. For transverse dipoles, the resonance frequency shifts downward as the incidence angle decreases. Therefore at 30 degrees incidence the current level has dropped slightly relative to 45 degrees incidence due to a resonance frequency shift.

The bistatic scattered fields are presented in Figure 38 for the Trunc, Inf, UTD and PO solutions. At 90 degrees incidence the Trunc and UTD curves again match each other very well until the plane of the array is approached. The UTD solution

Figure 36: Transverse dipole array currents — freq = 3.0 GHz, 33 columns, width = 94.2 cm (tip to tip) = 9.42λ. (The dipoles are in a triangular grid and would appear to overlap in the x-y plane view shown above. For the sake of readability, this overlap is not shown.)
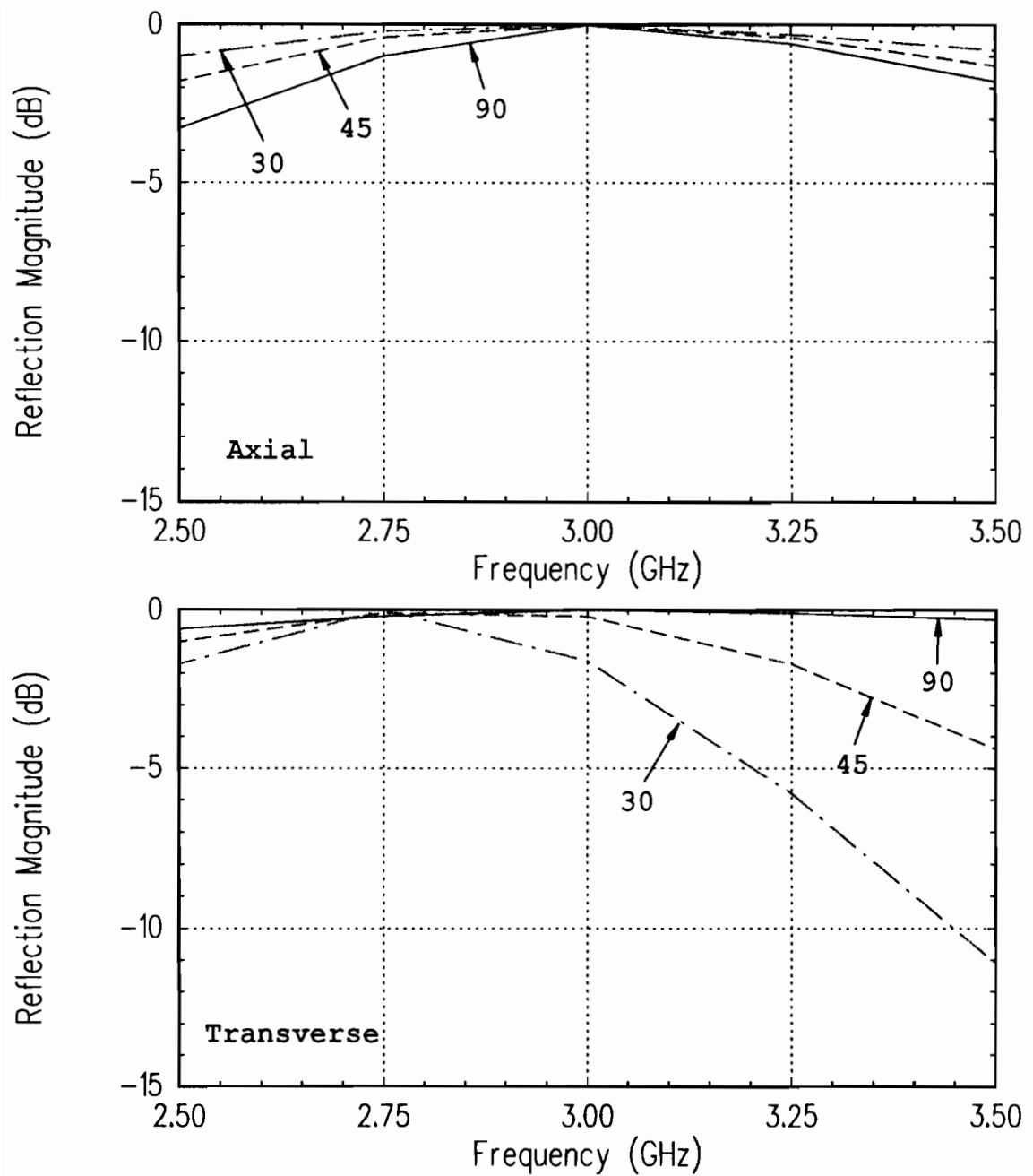
Figure 37: PMM reflection coefficients for three angle of incidence, top = axial dipoles, bottom = transverse dipoles.

does not go to zero as the other solutions do (and should) but one must bear in mind that only first order diffractions have been considered. (The implications of including multiple diffractions can be seen in the dissertation of Sikta [36].) The equivalent strip widths for this geometry and frequency were found to be 9.4 wavelengths for UTD and 9.15 wavelengths for PO. Thus, for the transverse case the equivalent UTD strip is larger than the PO strip whereas for the axial case the opposite is true. The differences between the Trunc and Inf curves appear to be somewhat more pronounced for this polarization. At angles off of broadside the Inf sidelobes start out higher than those of Trunc and end up substantially lower.

This array is now reduced to 13 columns for a total tip to tip width of 38.8 cm maintaining the dimensions given in Figure 35. The currents are as shown in Figure 39. The numbering scheme is the same as for the larger array and elements 2, 5,..., 35, 38 are shown. The overall magnitude is still centered at or near the level given by Inf but the overall character of the curve is no longer flat and smooth unlike the smaller axial case. Again a comparison of the outer elements from the larger array and those of the smaller array is made in Figure 40. (Again note that the element numbers for the larger array leading edge are not correct on this plot.) The smaller array still closely resembles the edges of the larger array but there does appear to be more interaction taking place now. The leading edge elements did not appear to vary at all when comparing the large and small axial arrays in Figure 33. For the transverse case it now appears that the trailing edge is having an impact on elements toward the leading edge. Also, the element at the trailing edge did not appear to be affected by the leading edge in the axial case but in the transverse case the trailing edge element now appears to be affected by the shrinking of the array. For the cases shown, in the axial case the leading edge currents appear to dominate with the trailing elements adjusting to match in the middle and in the transverse

76

Figure 38: Bistatic scattering pattern — freq = 3.0 GHz, array of 33 columns, width = 94.2 cm (tip to tip) = 9.42λ, UTD strip = 9.4λ, PO strip = 9.15λ.

case there appears to be more of a compromise from both ends. This does agree with trends that are seen on solid strips where the leading edge dominates for the E field parallel to the edge and the back edge becomes more prevalent for the E field orthogonal to the edge as the incident angle goes toward grazing.

The overall effect of these current changes is seen in the scattered fields shown in Figure 41. The resulting fields have the same characteristics as those exhibited in Figure 38 for the larger array. This indicates that although the edges appear to be interacting more, as indicated by the currents, the effect is not strong enough under these circumstances to be readily discernible in the scattered fields. The equivalent UTD strip width was found to be 3.82 wavelengths and the equivalent PO strip width was 3.6 wavelengths.

Overall the UTD, Inf and PO approximations to Trunc do not appear to be as good for the transverse case as in the axial case but there have been no dramatic shifts. If there were to be any dramatic shifts in the quality of the approximations, the expected place would have been at 30 degrees incidence for the transverse case as suggested by the resonance shift indicated in Figure 37. This does not appear to be a significant point however when the scattered field plots are examined.

A brief comment about the UTD and PO strip widths seems appropriate here. The PO solution assumes a constant current magnitude across the strip for plane wave incidence and hence as the array size is varied the rule for finding the equivalent strip width does not vary. The rule for the PO strip width appears to be to add one column spacing in wavelengths to the total array width in wavelengths measured from element center to element center or more simply, multiply the number of columns by the spacing in wavelengths. No such simple rules are evident for the UTD solution. With multiple diffractions being ignored, the equivalent strip width rule appears to be a function of the array width.

78
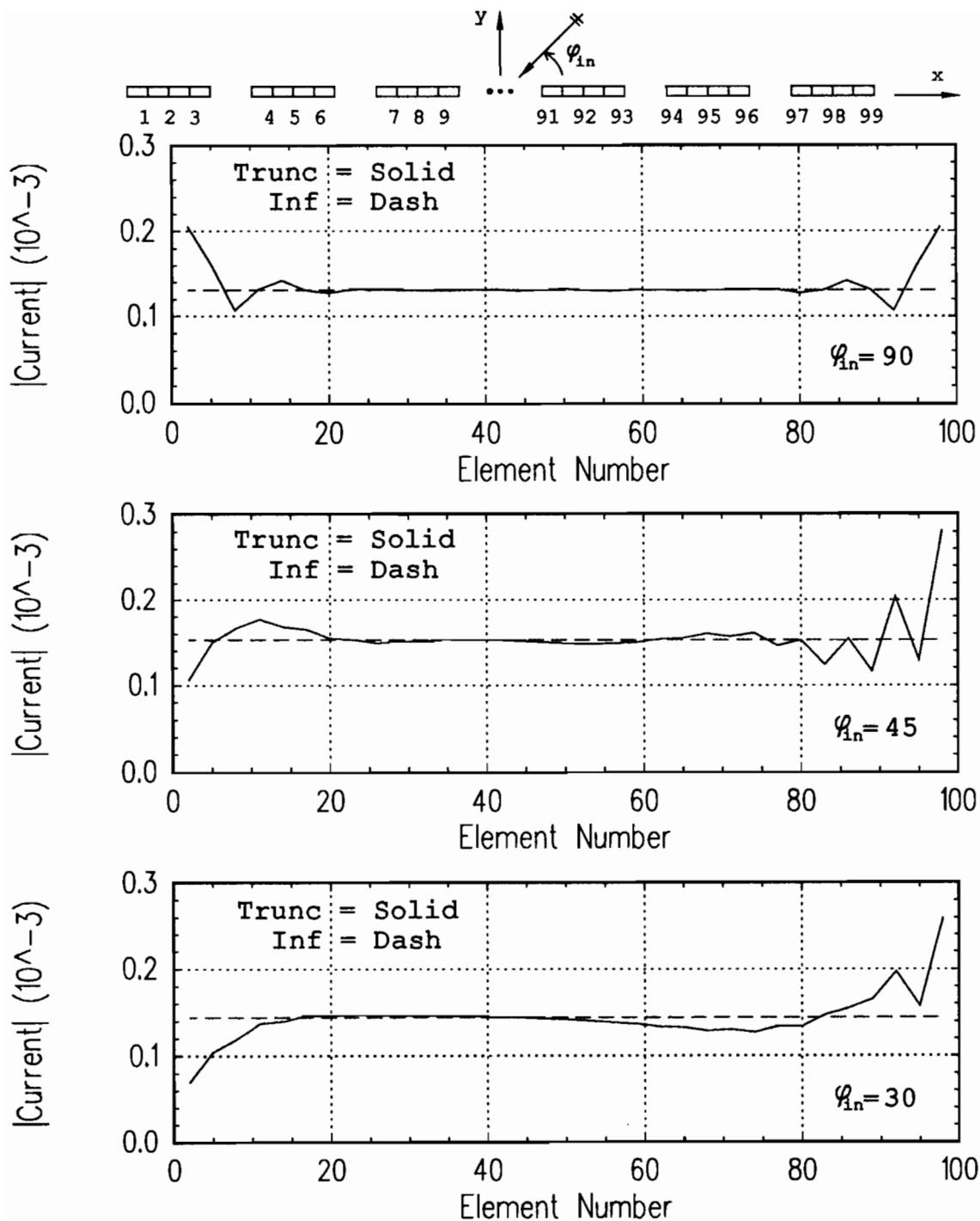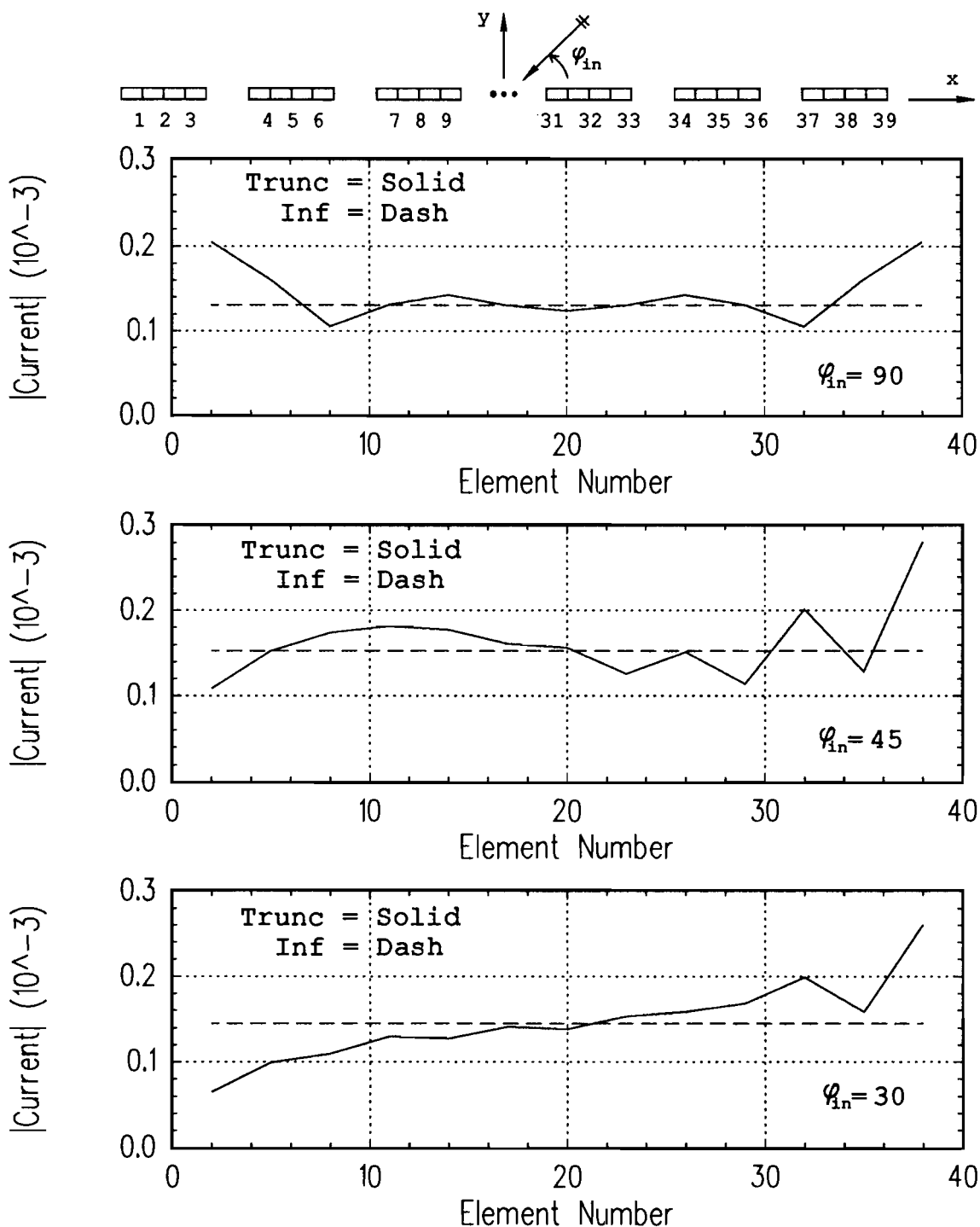
Figure 39: Transverse dipole array currents — freq = 3.0 GHz, 13 columns, width = 38.8 cm (tip to tip) = 3.88λ. (The dipoles are in a triangular grid and would appear to overlap in the x-y plane view shown above. For the sake of readability, this overlap is not shown.)
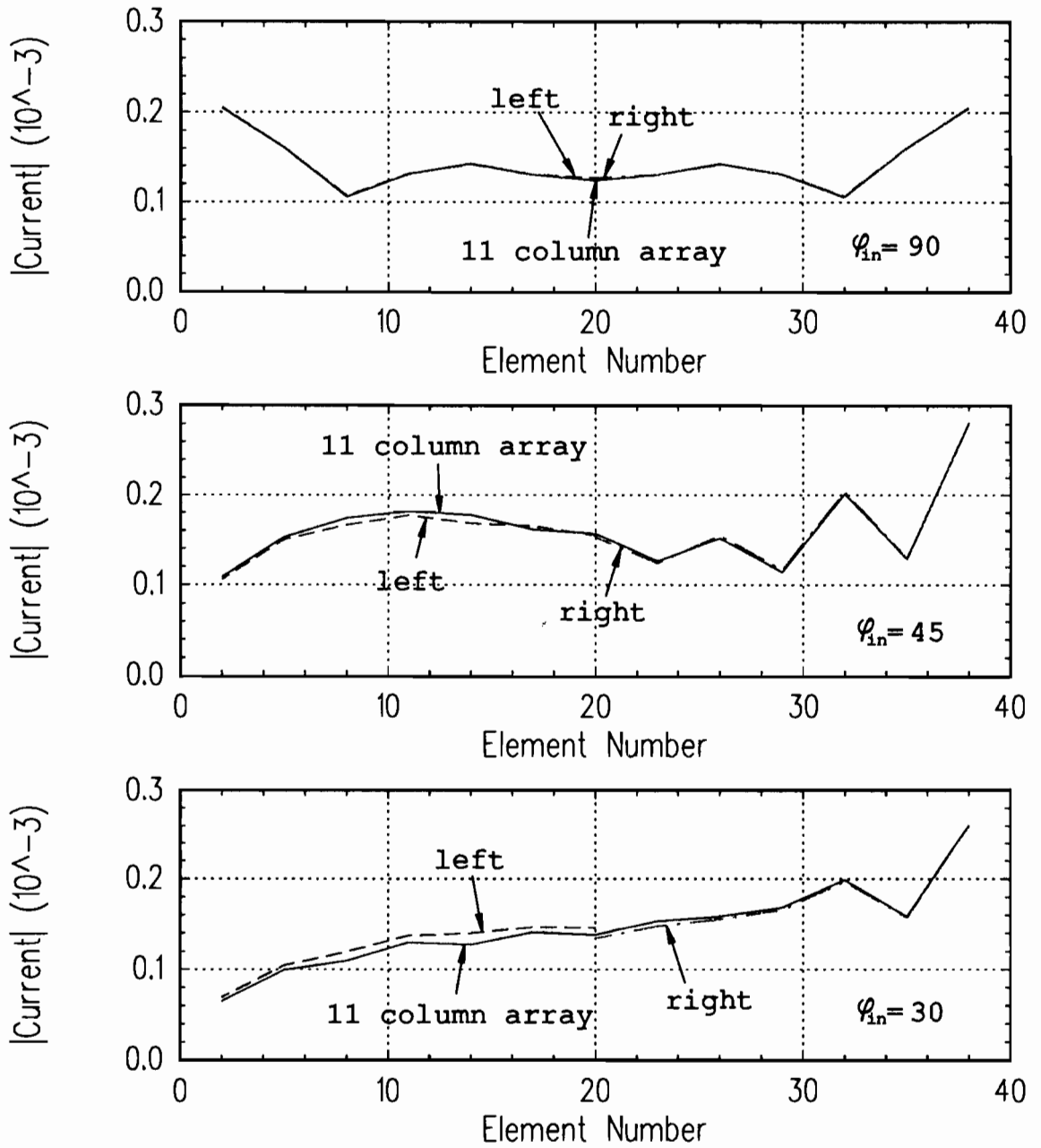
Figure 40: Transverse dipole array currents — freq = 3.0 GHz, 13 columns vs. edge columns of 33 element array, left = 7 columns on the trailing edge, right = 7 columns on the leading edge.

80
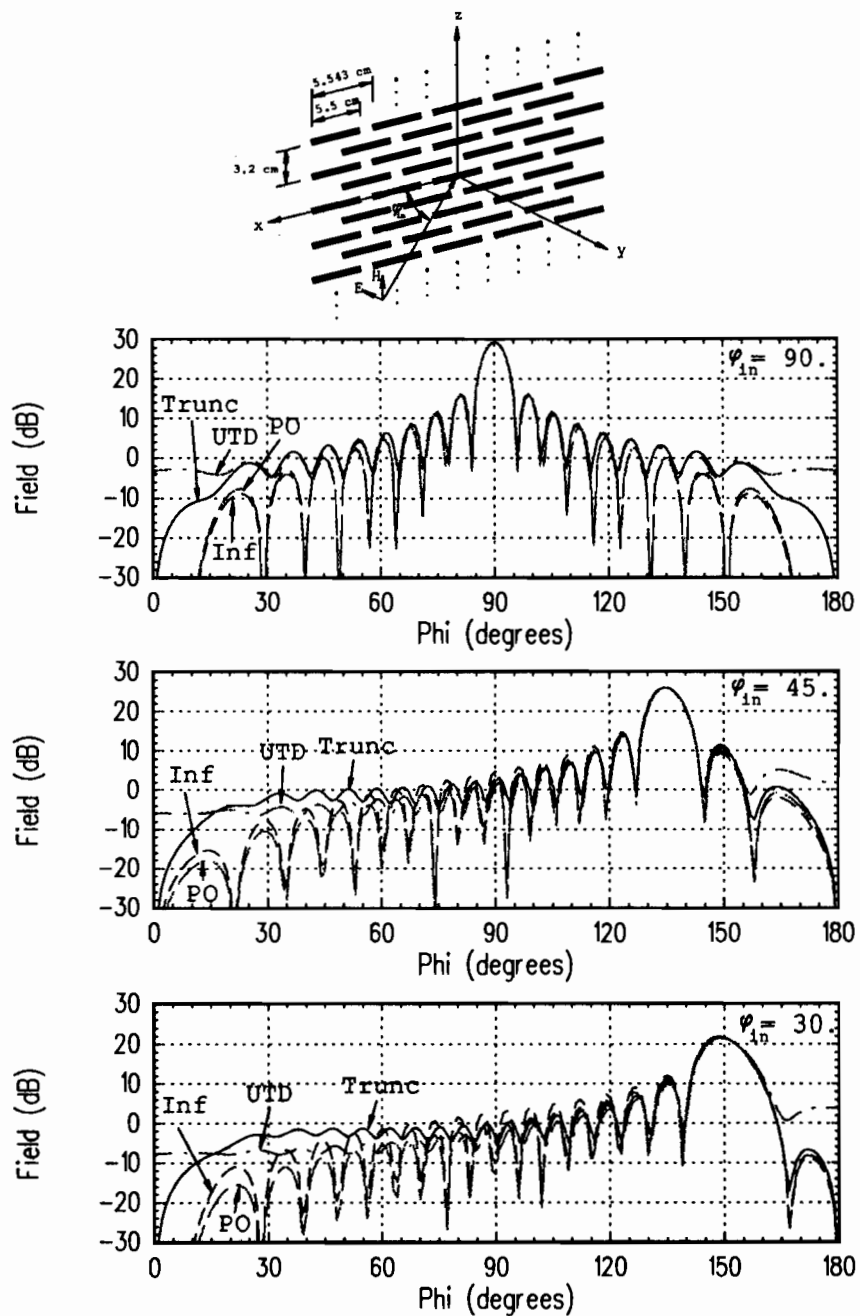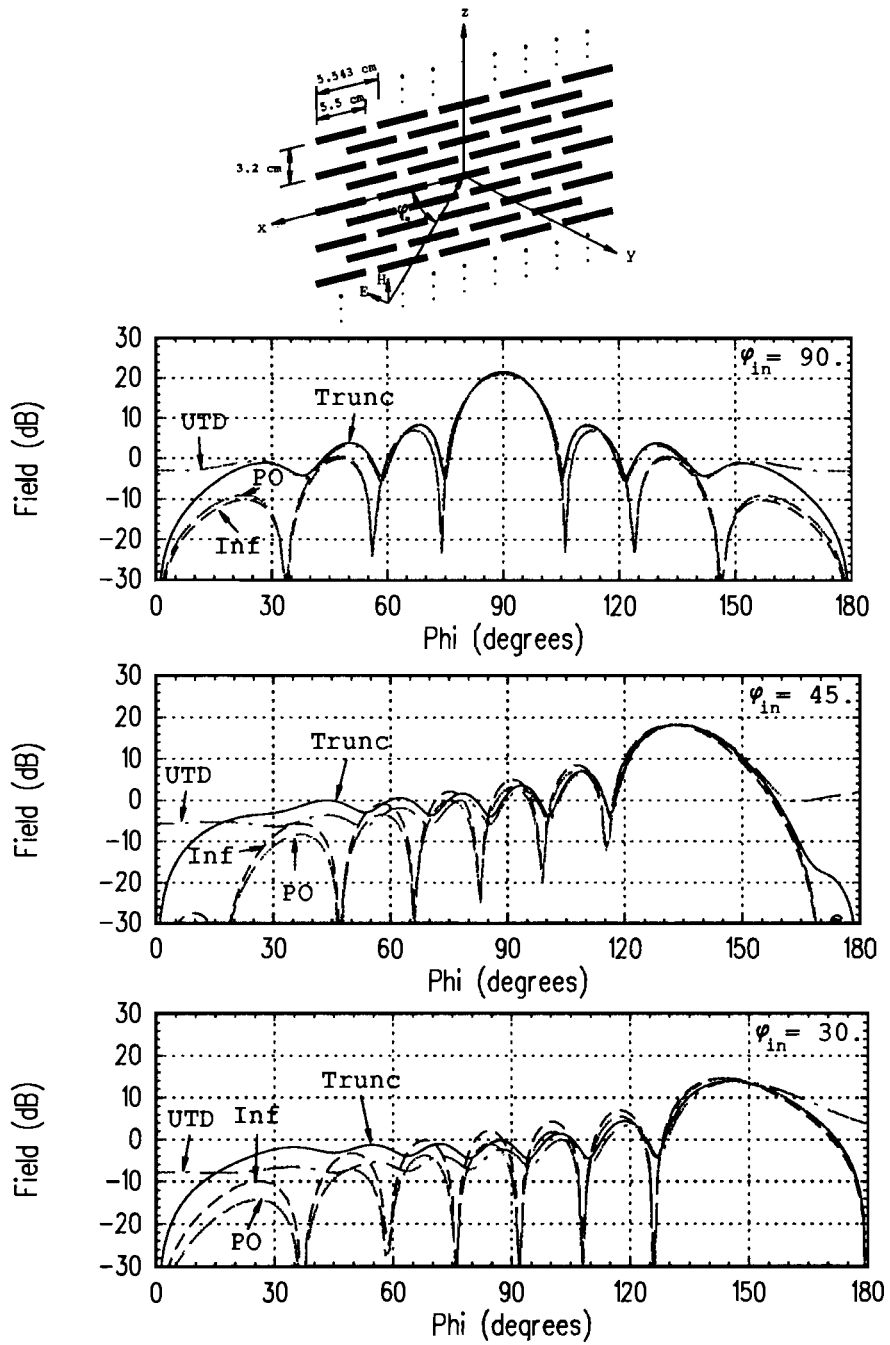
Figure 41: Bistatic scattering pattern — freq = 3.0 GHz, array of 13 columns, width = 38.8 cm (tip to tip) = 3.88 λ, UTD strip = 3.82 λ, PO strip = 3.6 λ.

Up to now the dipoles have been at their resonant frequencies. Let us now examine what happens as the frequency is varied. As an example we will take the case shown in the middle plot of Figure 41 and rerun it at 4 GHz. The UTD and PO strip widths have been scaled with the frequency. The results of this are shown in Figure 42. Two plots are presented. The top plot is the result of having a single mode on the elements and in the bottom plot there are 3 modes per element. As stated previously, the UTD solution has been normalized to the peak of Trunc and the PO results have been normalized to the peak of Inf. This demonstrates two major points. First, the amplitude and phase variation across the element is very significant in finding the scattered fields. Second, off of resonance the Inf approximation does a much better job than the UTD or PO solutions. Both of these observations indicate that the element pattern factor is becoming more dominant under these conditions. This is also seen in the movement of the scattered field peak, the change in its magnitude and the change in the sidelobe roll off characteristics. The solutions are in better agreement for the single mode case since the element pattern factor has not been allowed to show its true nature. That is to say that the solutions will agree on the wrong answer but not on the correct one!

4.3   Double Resonance

The UTD and PO solutions used here did not appear to work very well in modeling a truncated array of elements when off of their resonant frequency. In this section another complexity will be added that will be difficult for simple models, that do not include the element characteristics, to handle. This complexity comes from the addition of another axially oriented array of elements that are resonant at a different frequency from the first. The additional array will have 10 columns of
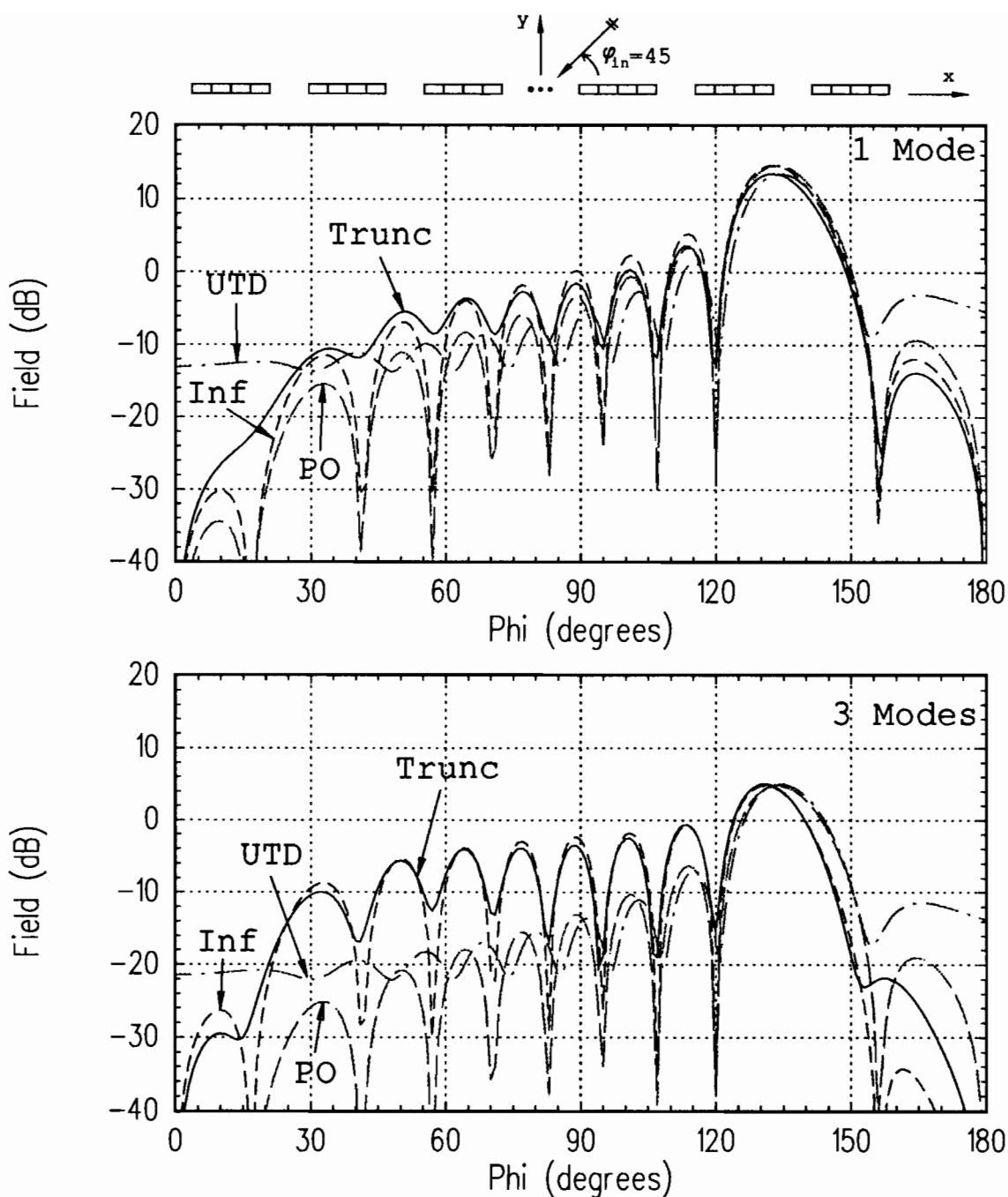
Figure 42: Bistatic scattering pattern — freq = 4.0 GHz, top = 1 mode, bottom = 3 modes, array of 13 columns, width = 38.8 cm (tip to tip) = 5.17 λ, UTD strip = 5.09λ, PO strip = 4.8λ.

shorter elements resonant at 5 GHz interspersed among the original 11 columns as shown in Figure 43. Each element will have three modes as indicated in Figure 44.

The frequency response of this structure is shown in Figure 45 for angles of incidence, 90, 45 and 30 degrees. The frequency response is a plot of the field in the specular direction normalized to an equivalent PO solution (which is proportional to the square root of the frequency). Between the two resonant peaks, there lies an anti-resonance or null. The exact frequency at which this occurs is a function of the angle of incidence.

Figure 46 shows the bistatic scattered fields for the three angles of incidence at three frequencies per plot, 3 GHz, 5 GHz and the null frequency. The curves were all derived from the numerically rigorous approach (Trunc). Note that although there is indeed a null in the specular direction in comparing frequencies, this is not true in other directions.

The UTD and PO strip approximations will give reasonable results at the resonant frequencies of 3 and 5 GHz but do not appear to be useful at the null frequency. The Inf approximation however is capable of giving a reasonable result even at the null frequency.

The current on the short elements is shown in Figure 47 and the current on the long elements in Figure 48. There are three curves per plot showing the currents at 3 GHz, 5 GHz and the null frequency and three plots per page showing the currents for 90, 45 and 30 degrees incidence. Each dipole is constructed of three modes and what is plotted is the magnitude of the center element mode of each dipole. The element numbering starts with the trailing edge long dipole and ends with the leading edge long dipole which is the 21st dipole for a total of 63 elements. Hence the long element numbers plotted are 2, 8, 14,..., 56, 62 and the short element numbers plotted are
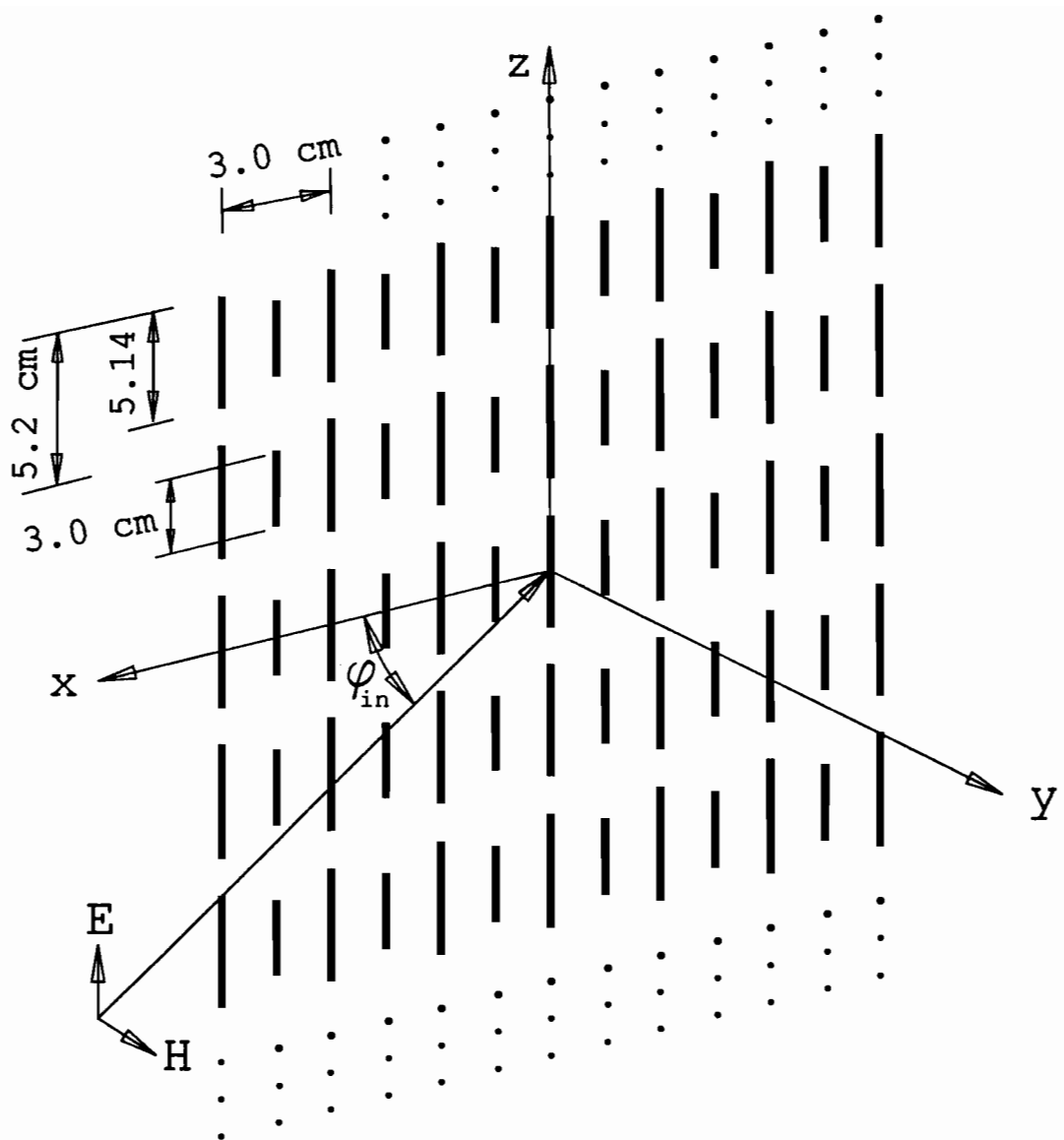
Figure 43: Array of axially oriented dipoles of two lengths.

3 Modes/Dipole
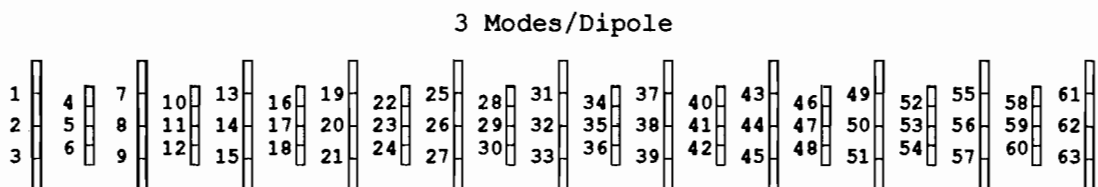
Figure 44: Mode structure for the double resonance geometry.
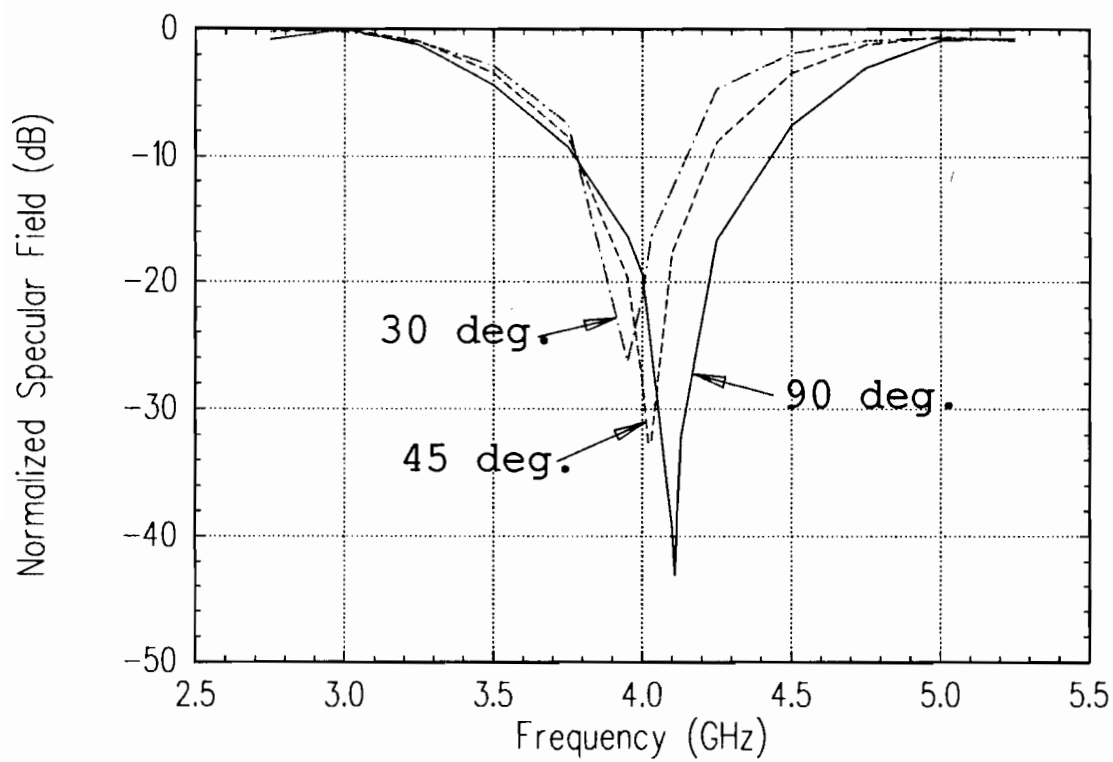
Figure 45: Double resonance frequency sweep — array width = 30 cm.
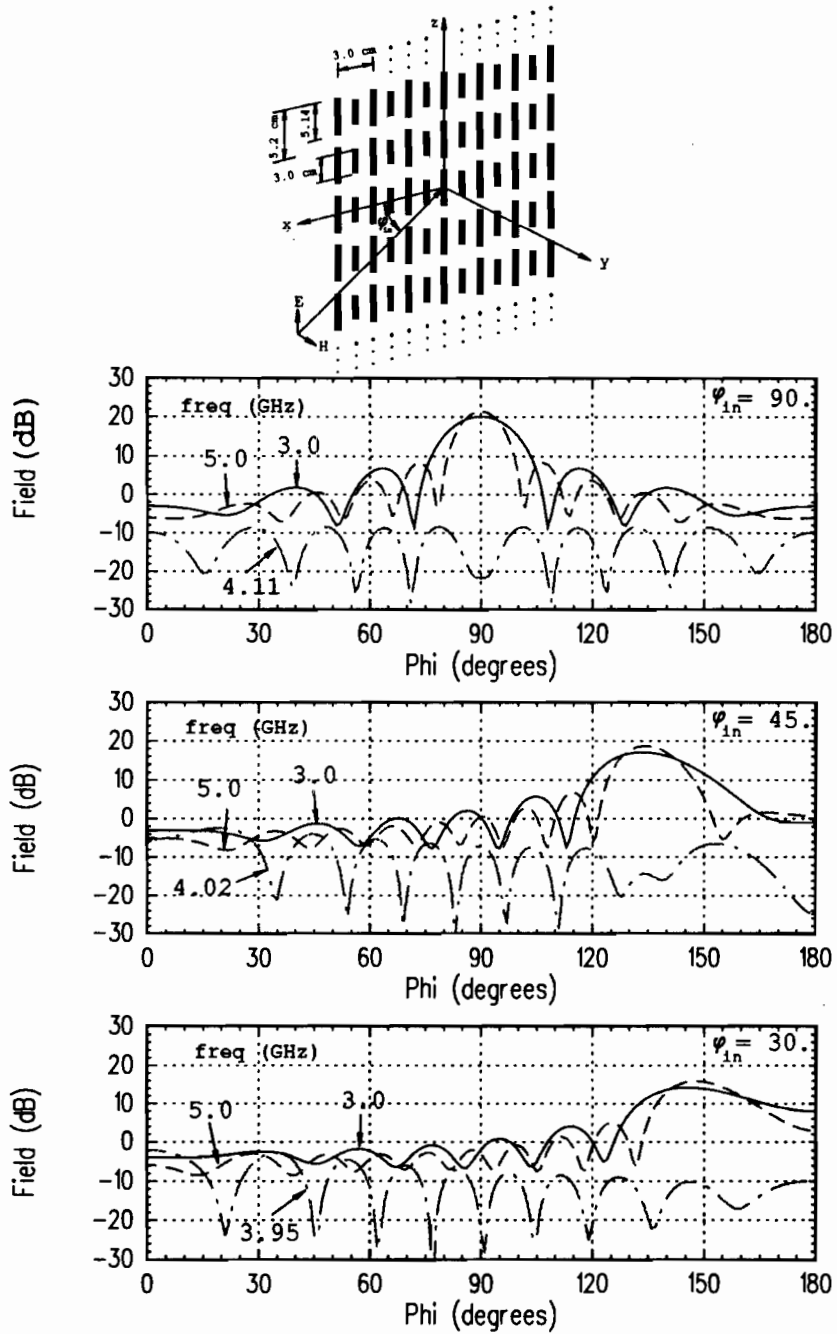
Figure 46: Bistatic scattering pattern for the resonant and anti-resonant frequencies. Trunc results only, array width = 30 cm.

5, 11, 17,..., 53, 59. Three modes were used to insure an adequate representation of the currents at frequencies off of resonance.

Examining the short elements first, the currents at 3 and 5 GHz decrease with the incidence angle at a rate roughly equal to the sine of the incidence angle. This makes physical sense since the total power capture area of the array will drop as the sine of the incidence angle and, for axially oriented dipoles at or below resonance, the pattern factor is peaked at broadside to the dipoles which does not vary with the incident angle. The current level at the null frequency however does not vary with incidence angle.

Examining the long elements, the currents at 3 GHz follow the same drop off trend with the sine of the incidence angle as is to be expected since the long dipoles are resonant at 3 GHz. Also, comparing the currents at 3 GHz with those of Figure 32, the addition of the shorter elements did not change the characteristics of the currents but did shift the level slightly higher. The current level at the null frequency again does not vary with incident angle. (The ratio of the currents at the null frequency between the long and short arrays is approximately the same as the ratio of their lengths.) However, the currents on the long elements at 5 GHz do not follow the same drop off with incidence angle as at 3 GHz.

An expanded plot of the short dipole currents at 3 GHz and the long dipole currents at 5 GHz is shown in Figure 49. For comparison, the Inf currents for the same conditions are plotted in Figure 50. This shows that in this case, as in previous cases shown, the current levels between Trunc and Inf are roughly the same and that the variation in the long element current levels with incidence angle at 5 GHz is not dependent upon the array being truncated.

Using the Inf approximation, the current magnitude on the long and short elements is constant across the array. The current is given as a function of frequency
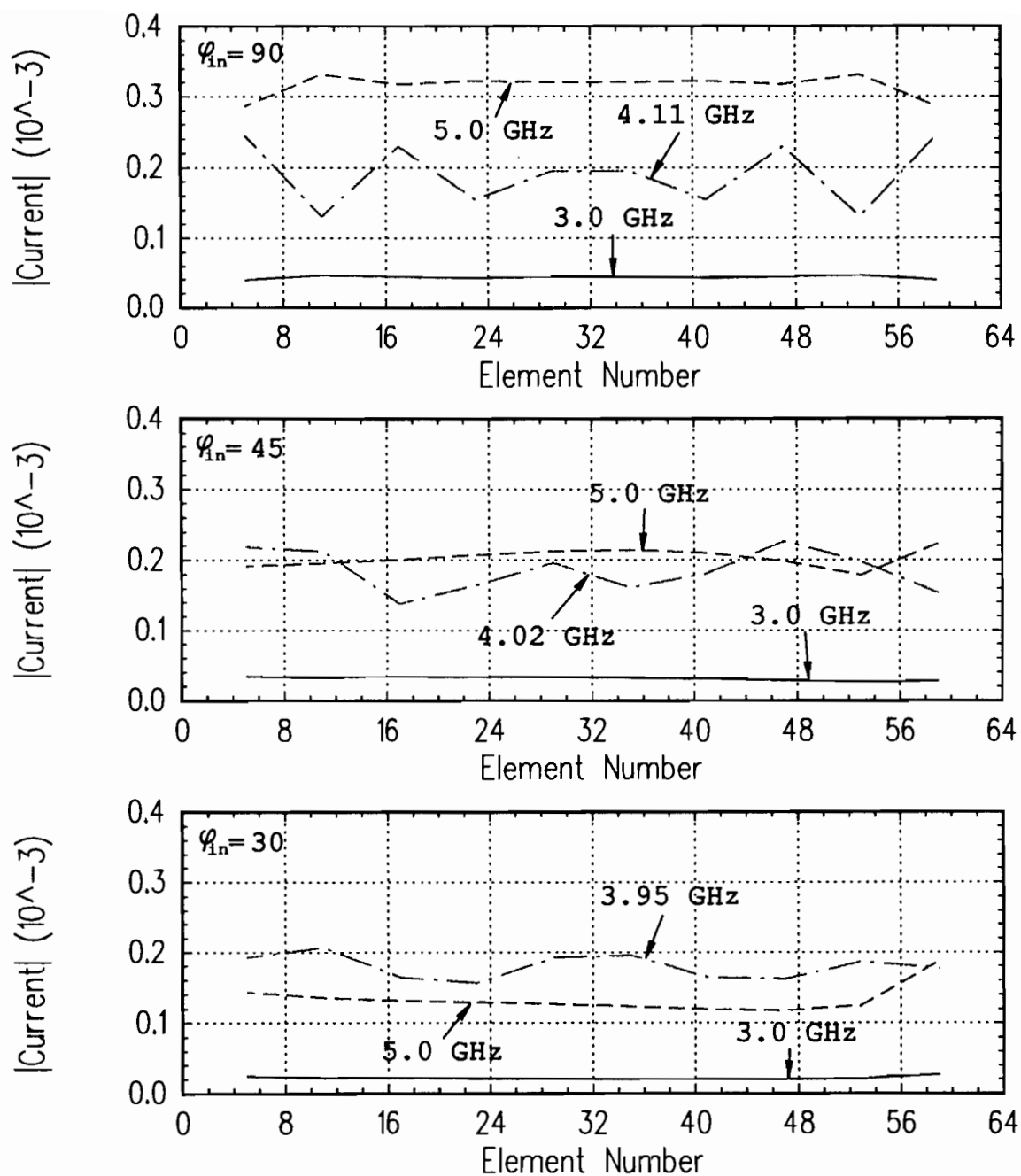
Figure 47: Current magnitude on the short elements of the doubly resonant array.
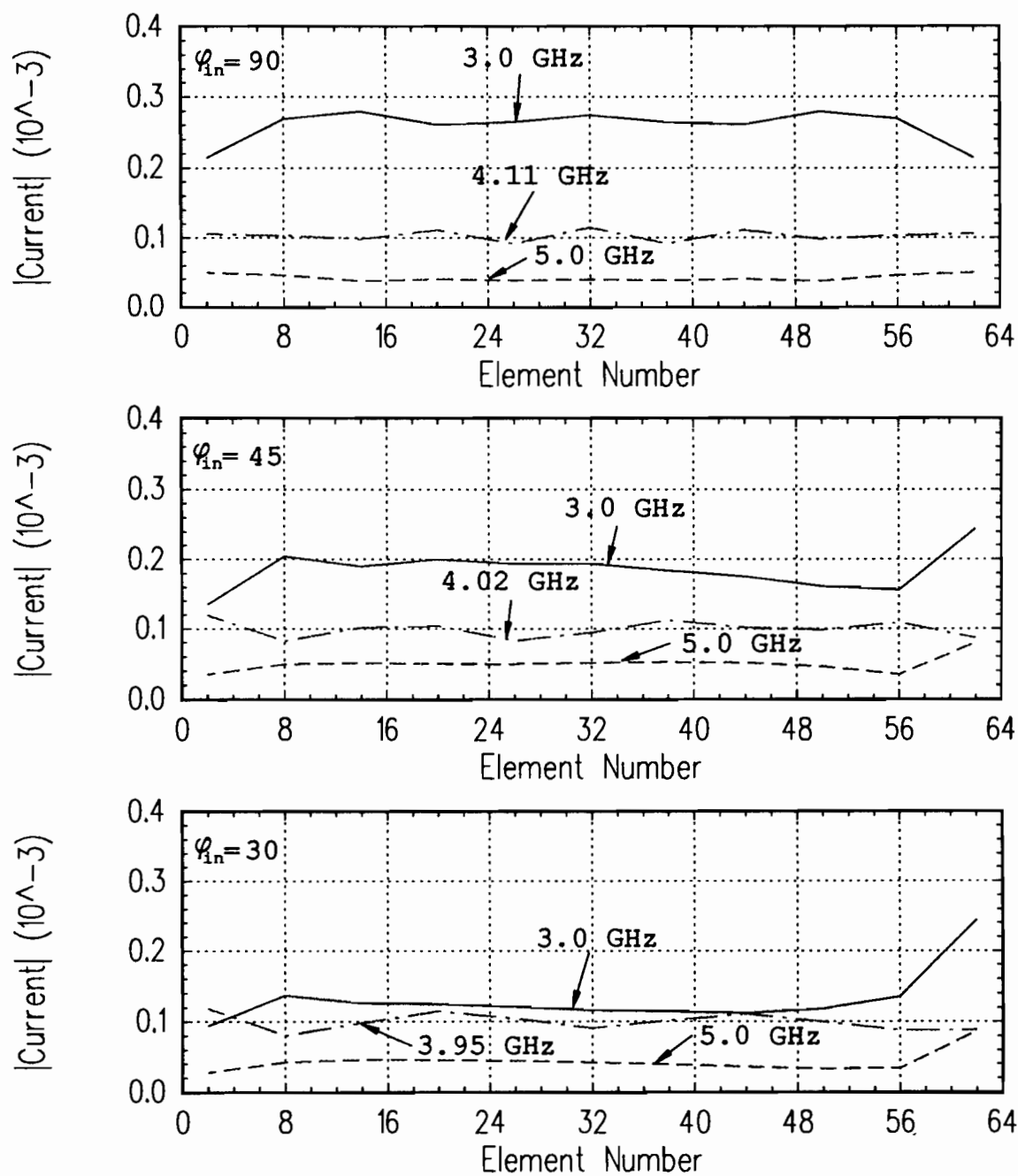
Figure 48: Current magnitude on the long elements of the doubly resonant array.
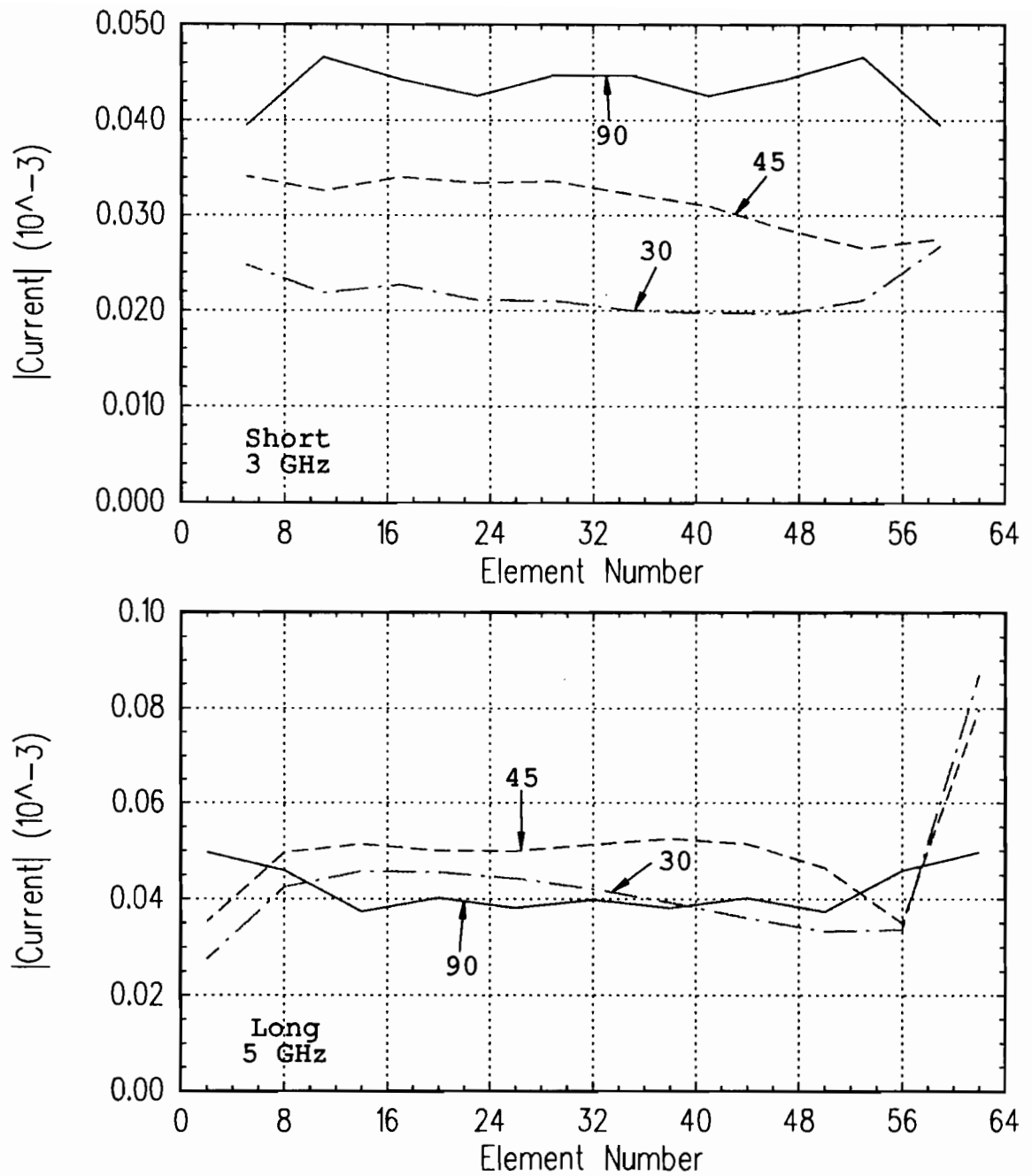
Figure 49: Expanded plot of the current magnitude on the short elements of the doubly resonant array at 3 GHz and the long elements at 5 GHz.

91
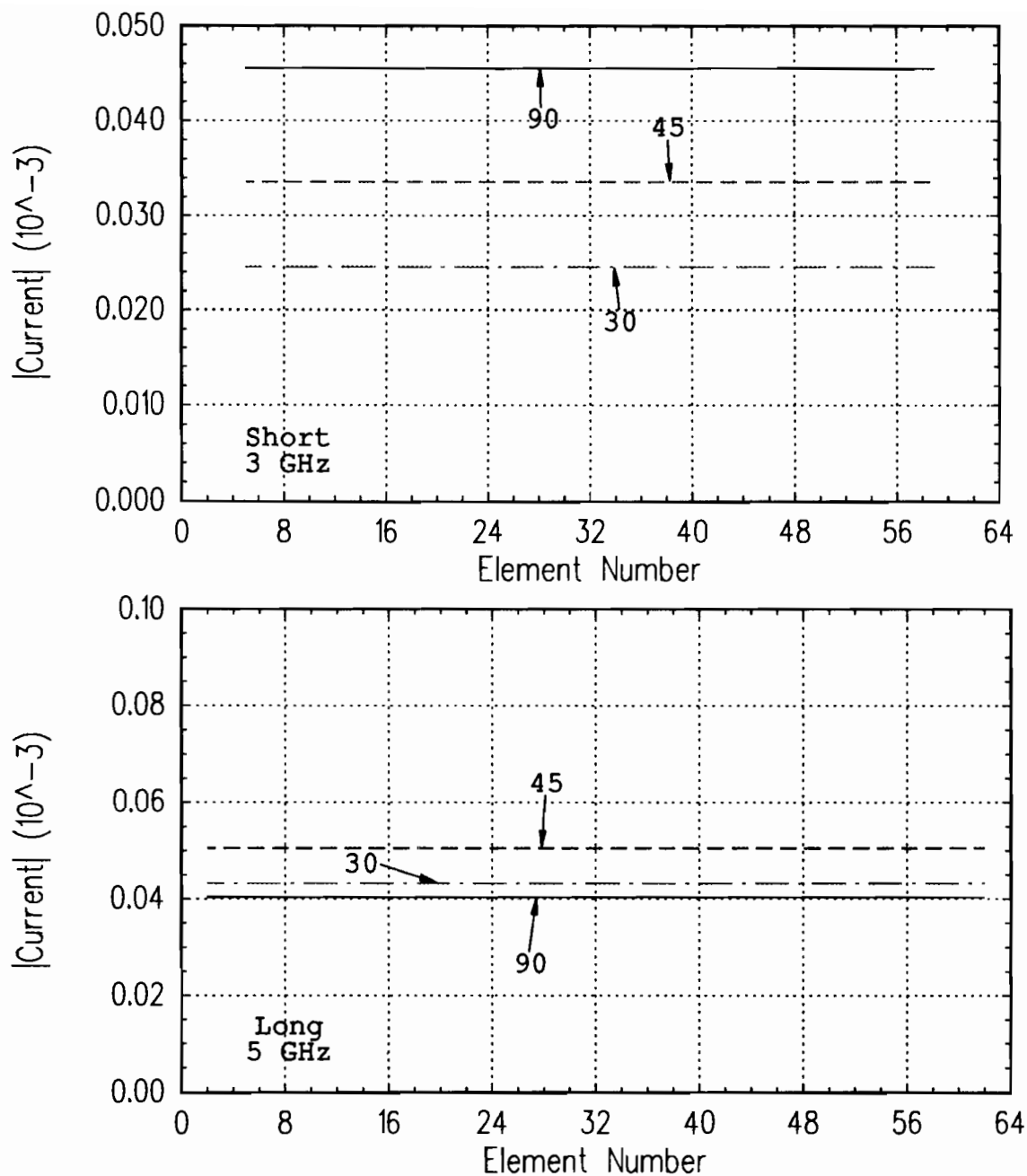
Figure 50: PMM current magnitude of the short elements of the doubly resonant array at 3 GHz and the long elements at 5 GHz.

as seen in Figure 51. The magnitude of the current is shown for the long elements (top) and the short elements (bottom) for three angles of incidence. The currents on the center elements of the finite array are very similar to these. It is seen that as the angle of incidence is varied, the current magnitude peak shifts and for the long elements, the anti-resonance point shifts. This results in the current magnitude not decreasing with the sine of the incidence angle at most frequencies as was expected.

It is also convenient to examine the fields resulting from the long and short elements separately as seen in Figure 52. Both arrays are simultaneously present but the fields from the long elements and short elements are found separately and in total as shown. The frequency at which the null occurs in the total curves corresponds to the point where the magnitude of the scattered fields from the long and short elements are equal.

The approach taken in this chapter was largely observational. Models ranging from the rigorous (Trunc) to those more crude (PO) were compared for several simple FSS geometries. The predicted scattered fields were presented along with the rigorously calculated current distributions on the elements. No attempt was made to give a physical reasoning as to how the current distributions arose to not digress from the comparison of the models. The next chapter will take a different approach. A sample design will be presented and each step will be explained in terms of how the coupling mechanisms affect the current distribution and the resulting scattered fields.
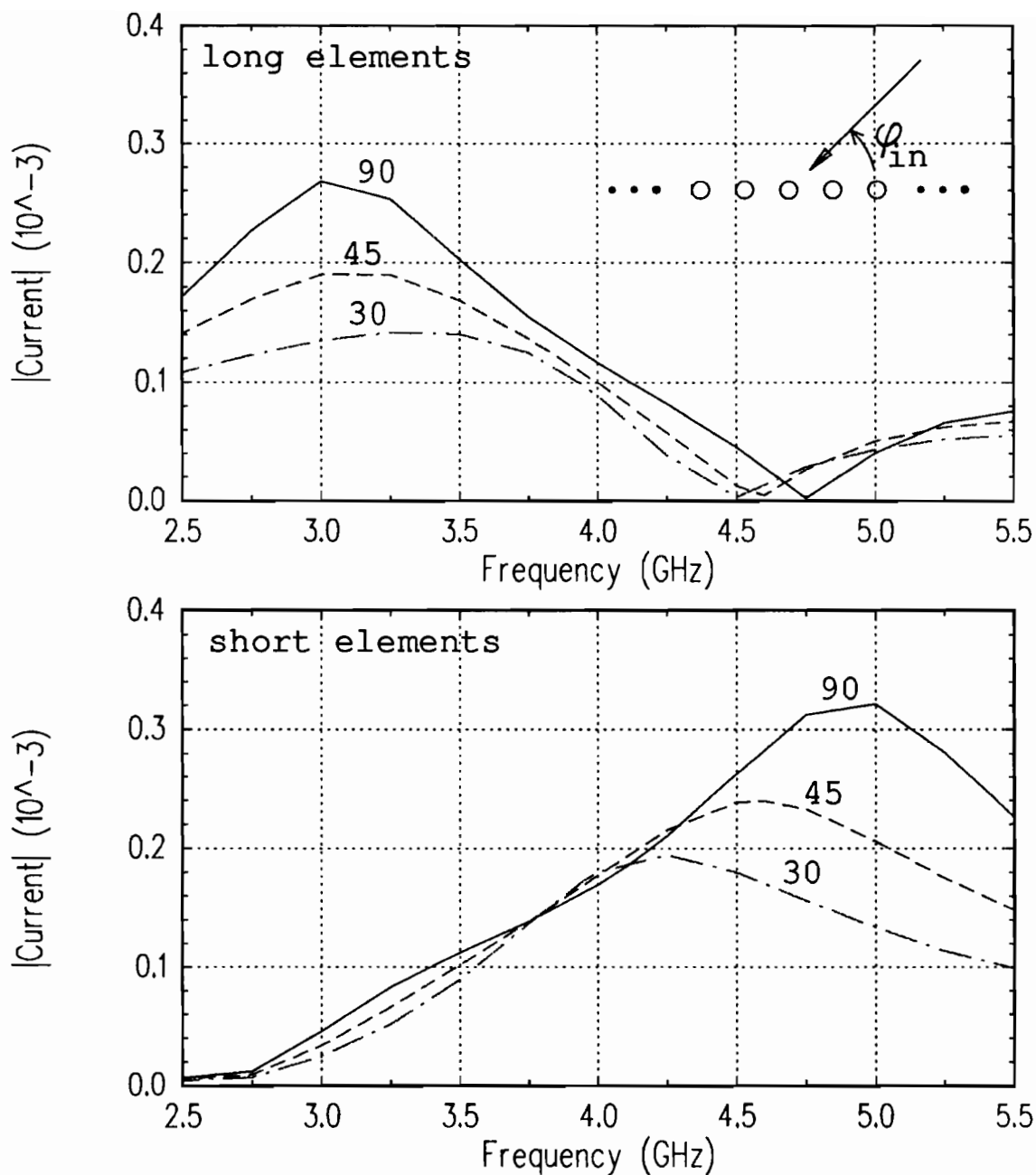
Figure 51: Inf approximation currents on the long and short elements as a function of frequency for three different angles of incidence.
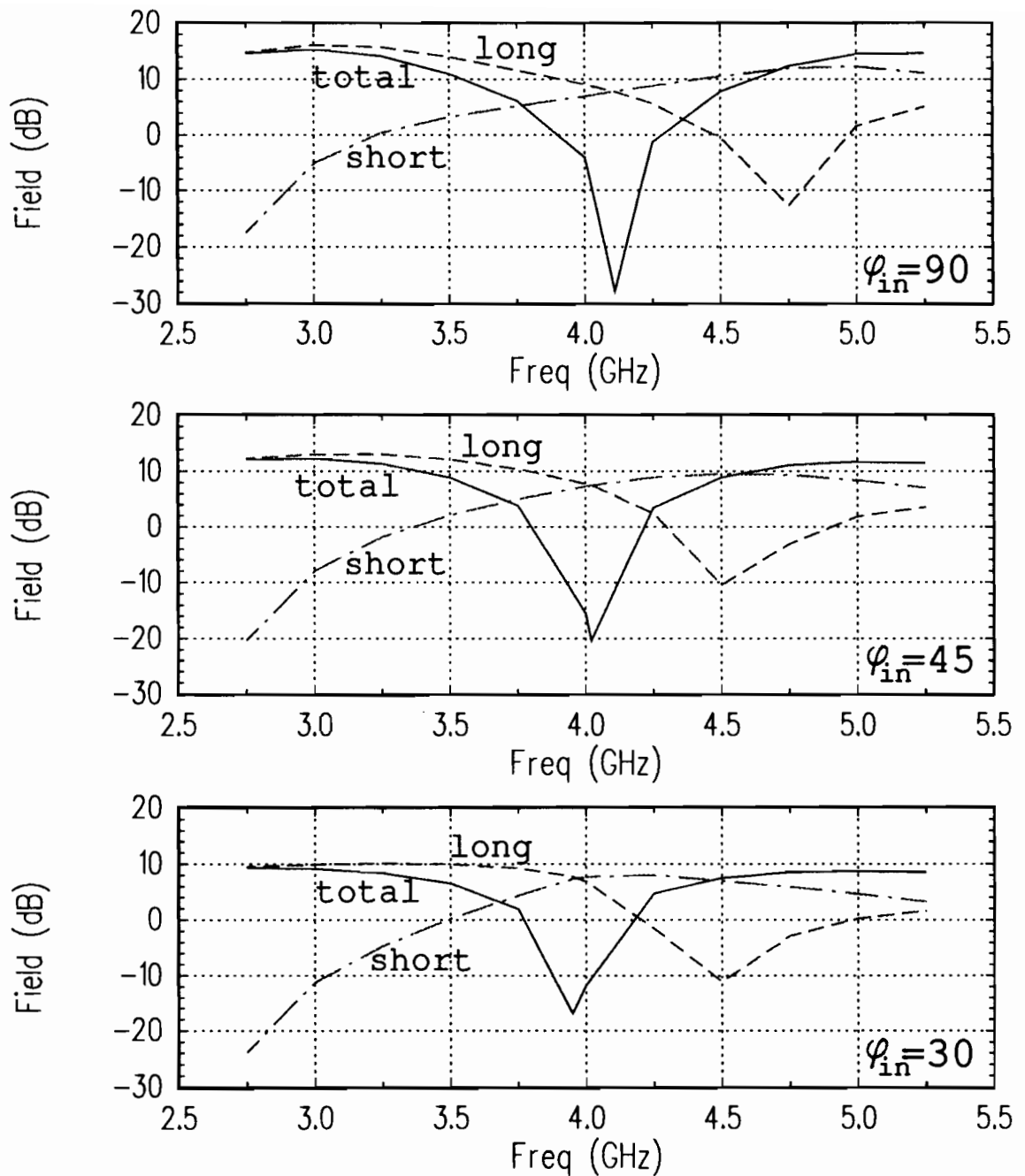
Figure 52: Specular scattered fields from the finite array as a function of frequency separated into contributions from the long and short elements for three angles of incidence.

CHAPTER V

Reduced Reflection Structures

This chapter will provide a sample design for a case where the truncation effect of a periodic structure is very evident. The design centers on the idea of wave absorption. Kraus [37] gives an example of how a wave can be absorbed by a resistive sheet having a resistance equal to the impedance of free space if that sheet is placed a quarter wavelength in front of a perfectly conducting sheet. This is commonly called a Salisbury screen. Here the perfectly conducting sheet will be replaced by an array of perfectly conducting axially oriented dipoles and the resistive sheet will be replaced by an array of perfectly conducting axially oriented dipoles with lumped loads. The backing array will be called the groundplane and the loaded array simulating the resistive sheet will simply be called the front array.

5.1 Groundplane

First the element dimensions for the groundplane are established and are given in Figure 53. The array is six wavelengths wide at 3.0 GHz with a column to column spacing of .3 wavelengths, an element to element spacing of .6 wavelengths and a wire radius of .02 cm. The element length is set such that the total reflected field is peaked at 3.0 GHz.

The resulting currents are shown in Figure 54 as a function of position. The current is relatively invariant across the middle of the array then drops at the edges
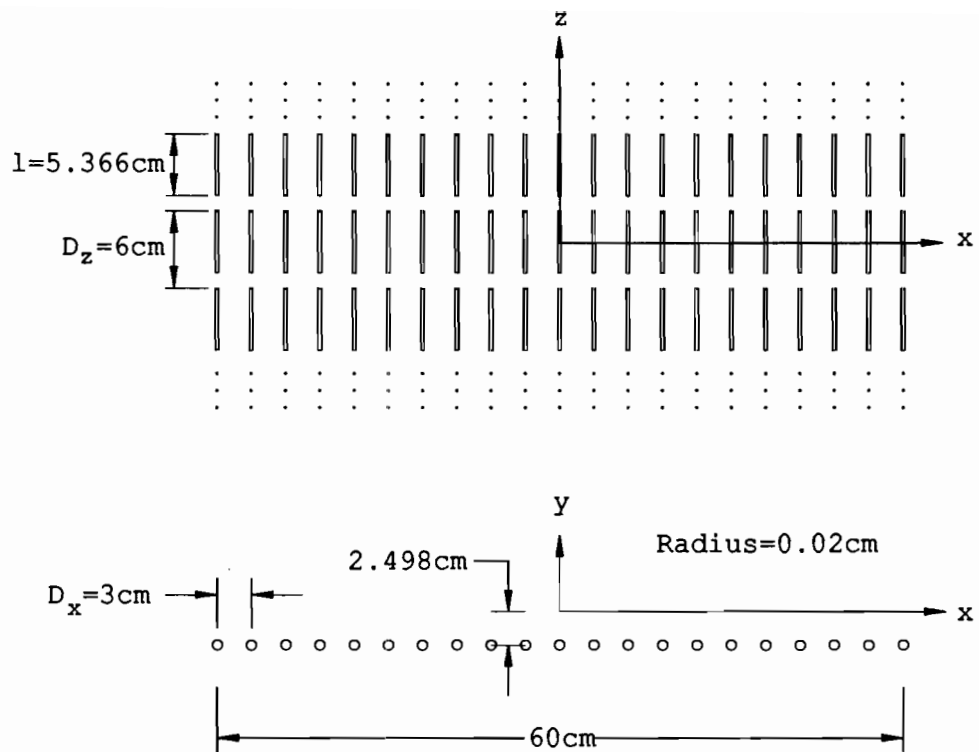
Figure 53: Groundplane geometry.
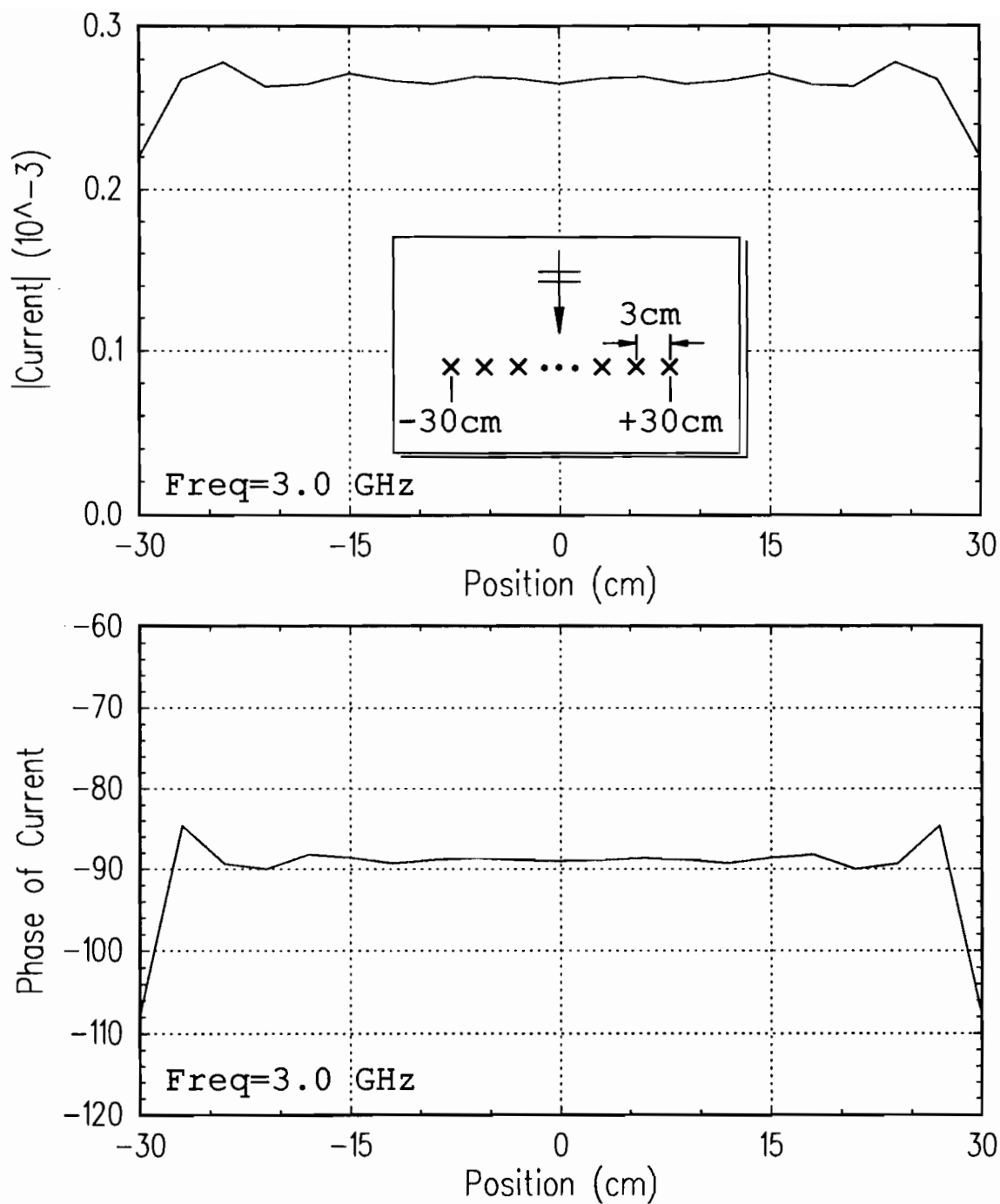
Figure 54: Current distribution across the groundplane. Top: magnitude in amps, Bottom: Phase in degrees.

of the array in magnitude and phase. This was also seen in the earlier chapter on frequency selective surfaces. The broadside coupling from column to column forces the elements to be longer than would be necessary for a single column to resonate at 3.0 GHz. At the edges of the groundplane the coupling is only to one side and as a result, the edge elements are not the proper length to resonant at 3.0 GHz creating a variation in the current near the edges.

A plot of the scattered field in the complex plane is shown in Figure 55. The phase is referenced to the origin and the field is normalized by $\sqrt{j \cdot \text{freq(GHz)}}$. This choice of normalization is derived from the far field equation (F.8) given in Appendix F. The far field of a single column of elements is seen to vary in magnitude with $\sqrt{\text{frequency}}$ and has a fixed phase offset of $\sqrt{j}$. The normalization removes the magnitude variation with frequency of each individual column and sets the phase reference to zero for an element at the origin.

Two curves are given on Figure 55. One is for the total groundplane and the other excludes the field contributions from the edge elements. The total is seen to be resonant at 3.0 GHz as was desired but if the edge element contributions are omitted, the resonance is slightly higher than 3.0 GHz. In effect, the entire array has been shortened slightly to compensate for the edge elements being too long.

It is strongly emphasized that when the field contributions from part of an array of elements is shown, the currents used are those that are calculated with all of the elements present and all coupling has been taken account of. The field from the total structure is found by superposition of the contributions from each element. The field from parts of the structure are found by superposition of the contributions of the specified elements. The currents used in finding the total and partial fields are the same.

99
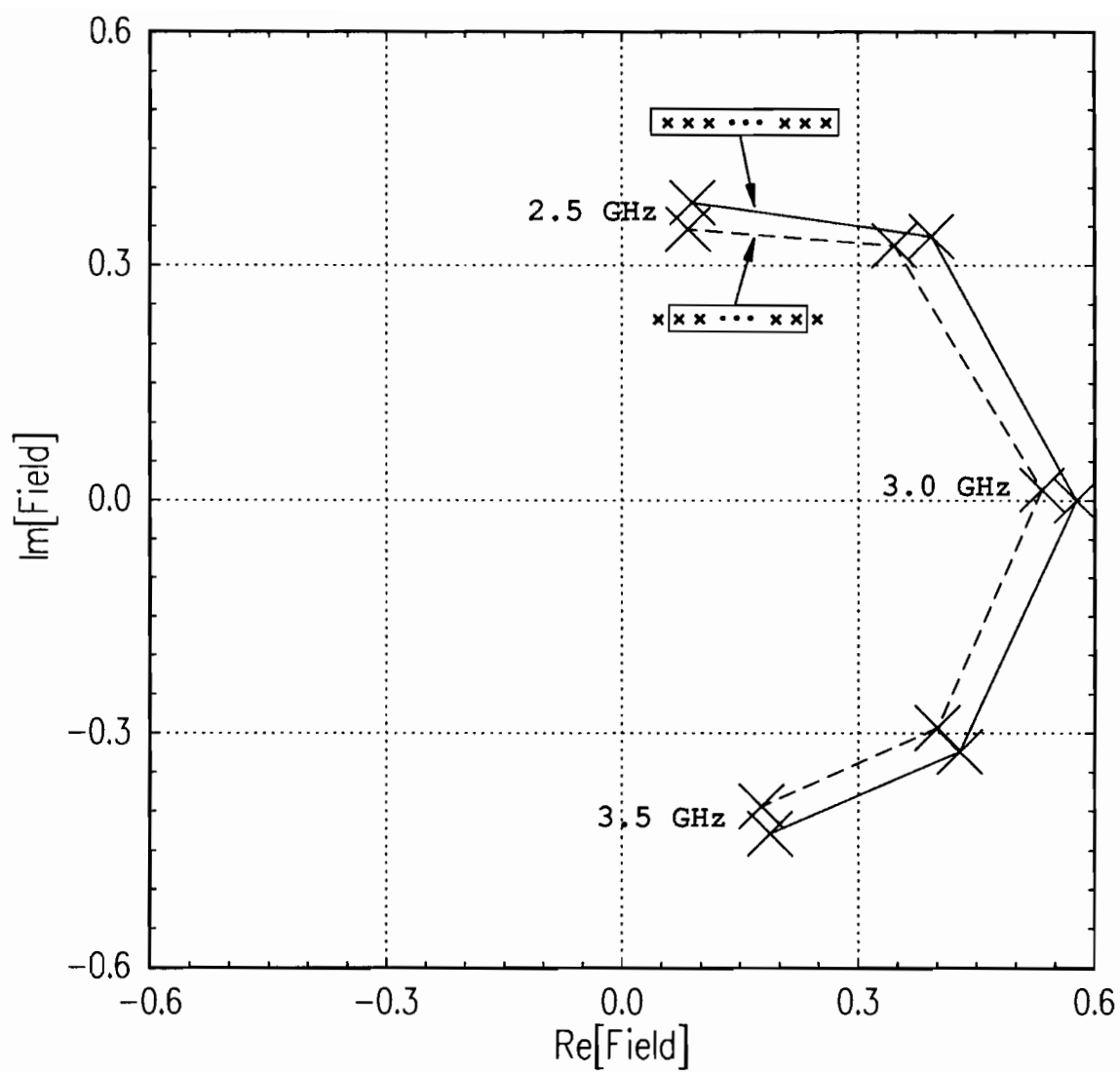
Figure 55: Groundplane backscattered field in the complex plane with and without the edge elements.

A bistatic pattern is shown at the top of Figure 56 at a frequency of 3.0 GHz. It shows the expected dropoff and lobing structure as was seen in the earlier chapter on truncated frequency selected surfaces. It also is seen to have been normalized such that its peak value is 0 dB. All bistatic plots shown in this chapter will be normalized to this peak value to easily see the reduction in backscattered field obtained. The bottom plot shows the backscattered field magnitude vs. frequency. This curve is additionally normalized by $\sqrt{j \cdot \text{freq(GHz)}}$ like the curves in Figure 55 are. Therefore, the peak value is down by $\sqrt{3.0}$ or 4.77 dB from the top plot. All plots in this chapter of the backscattered field, for magnitude or in the complex plane, as a function of frequency will be normalized by the peak value established above and by $\sqrt{j \cdot \text{freq(GHz)}}$.

5.2   Groundplane Plus a Resistive Layer

The next step is to add the loaded array of elements one quarter wavelength in front of the groundplane as shown in Figure 57. The elements in the front array are identical to those in the groundplane with the exception of them having a lumped purely resistive load placed on them. The value of the load is varied until the backscattered field is minimized, yielding a final load value of 282 ohms. This choice of load results in the currents shown in Figure 58. The currents on the front array and the groundplane are now seen to be equal in magnitude and 90 degrees out of phase. Comparing these currents to those in Figure 54, the magnitude for each element is now halved due to a doubling in the number of elements. The phase variation at the edge is seen to be greater on the groundplane and lesser on the front array compared to Figure 54.
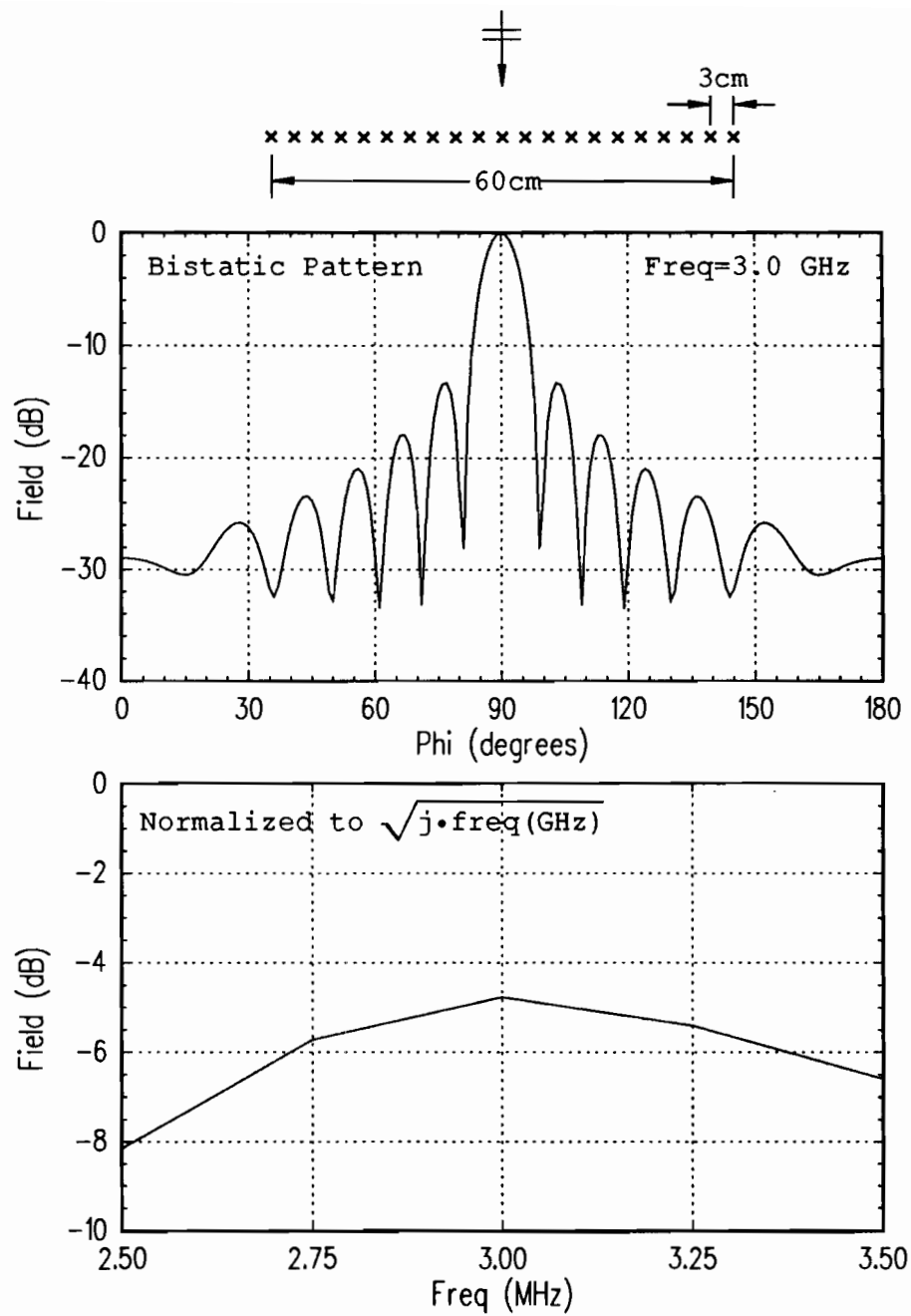
Figure 56: Top: Groundplane bistatic pattern at 3.0 GHz, Bottom: Magnitude of backscattered field vs. frequency.

Front array

1=5.366cm, radius=0.02cm, Z_L=281.6 Ω

D_y=2.498cm

1=5.366cm, radius=0.02cm, Z_L=0 Ω
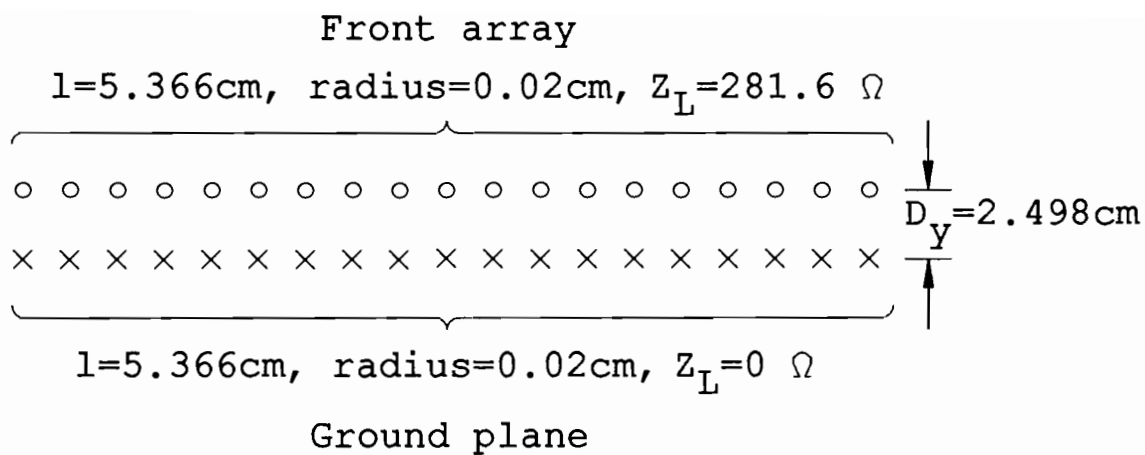
Ground plane

Figure 57: Geometry of the groundplane plus a resistive layer.
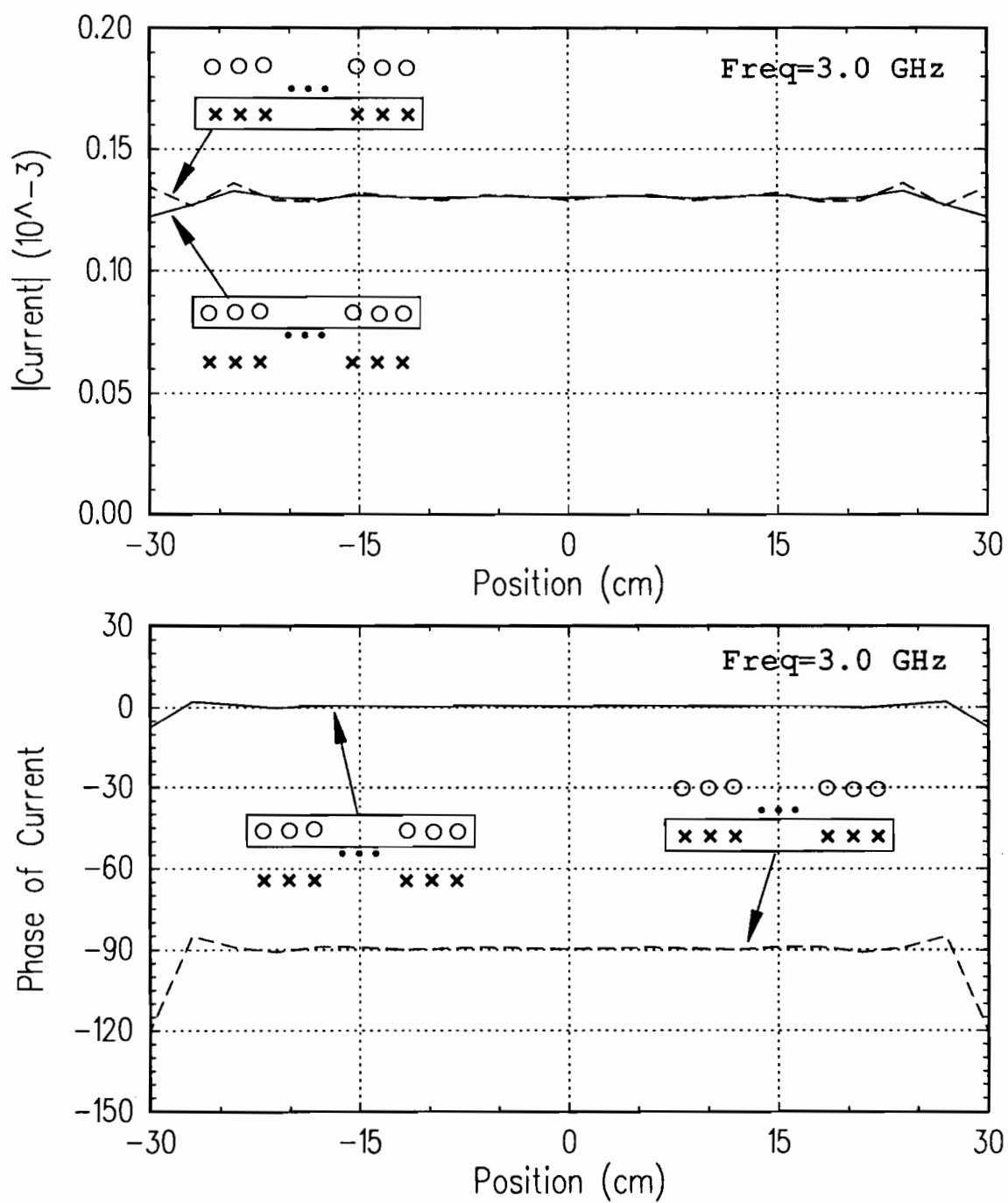
Figure 58: Currents across the groundplane and resistive layer. Top: Magnitude in amps. Bottom: Phase in degrees.

Figure 59 shows the backscattered field in the complex plane as a function of frequency. The top plot shows the field from the total structure and the contributions from the front array and groundplane separately. The front array resonates at 3.0 GHz as is desired but the groundplane is resonant at a lower frequency. The real parts of the front array and groundplane cancel as is desired but the imaginary parts do not. The bottom plot shows the total structure field again on an expanded plot and also the field from the structure with the edge front-back pair contributions omitted. Without the edge pair contributions, the backscattered field is seen to go toward zero at 3.0 GHz as is desired. This is more readily seen in Figure 60. The top plot shows the bistatic pattern for the total structure at 3.0 GHz. Overall, the backscattered field has been reduced about 35 dB from the groundplane alone, which is good, but for an infinite array the reduction would be much greater and there should be no backscattered field at all at the design frequency for broadside incidence.

The center plot shows the fields from the center of the structure with the edge pair contributions omitted. This now more closely resembles what would be expected from an infinite array. The bottom plot shows the contributions to the total fields of the edge pairs. They are seen to be the dominant contributors to the backscattered field for this structure at 3.0 GHz for broadside incidence.

Returning to Figure 59, it is noted that the curve for the groundplane contribution spans a greater range than the front array contribution curve does. This occurs due to the spacing of the arrays. The front array is at the reference point for phase and the groundplane is $\lambda/4$ behind it at 3.0 GHz. For frequencies higher than 3.0 GHz, the phase rotation to reach the reference point is greater than $\lambda/4$ and for frequencies less than 3.0 GHz, the phase rotation is less than $\lambda/4$, resulting in a greater spread between frequency points for the groundplane curve. Recalling the

Figure 59: Backscattered field from the groundplane and resistive layer. Top: Total structure fields and contributions from the front array and groundplane separately. Bottom: Total structure fields and contribution from the center part omitting the edge pairs.

106

Figure 60: Bistatic scattered field from the groundplane and resistive layer at 3 GHz. Top: Total structure. Middle: Center contribution omitting edge pairs. Bottom: Contribution from edge pairs. Normalized to peak of groundplane alone.

l=5.58cm, radius=0.06cm, Z_L=0 Ω
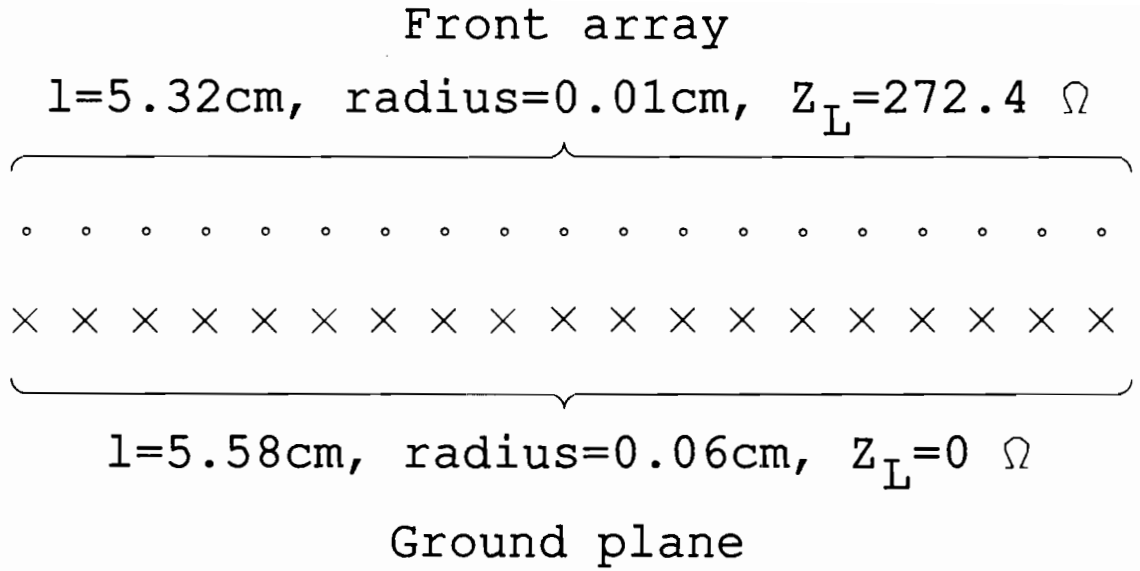
Ground plane

Figure 61: Modified geometry. Groundplane elements have been made fatter and the front array elements are now thinner.

effects of varying the wire radius, the next design will increase the groundplane wire radius to .06 cm and decrease the front array wire radius in an attempt to equalize the frequency spread of the two curves, thus hopefully yielding greater bandwidth.

5.3 Variation of Array Element Radii

The next geometry under consideration is shown in Figure 61. The front array element and groundplane element radii were altered, the lengths were adjusted such that they were again resonant at 3.0 GHz and the load value reset. The resulting currents for this configuration are shown in Figure 62. The current magnitude levels are no longer equal between the front array and the groundplane reflecting the differences in their geometries now. The phase relationship however does not appear to have been altered much when compared with the currents in Figure 58.
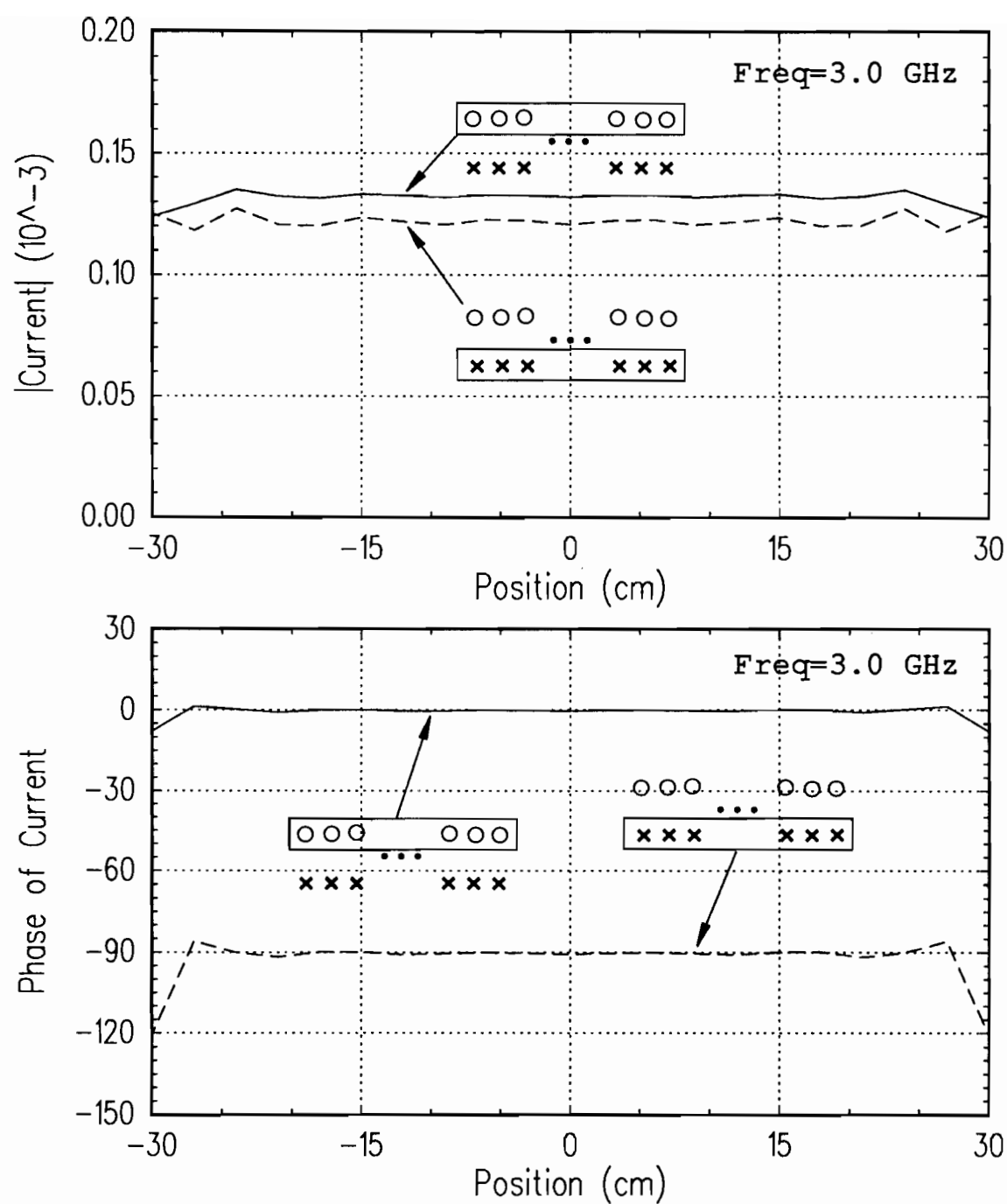
Figure 62: Currents across the modified geometry. Top: Magnitude in amps. Bottom: Phase in degrees.

The backscattered fields are plotted in the complex plane in Figure 63. The curve for the front array contribution is seen to have expanded somewhat from Figure 59 due to a decrease in the wire radius and the curve for the groundplane contribution is seen to have contracted due to an increase in the wire radius. The total field, which is a sum of the front array and groundplane contributions, is now contracted closer to the origin implying wave absorption over a wider bandwidth than before. The bottom plot of Figure 63 shows the total structure field on an expanded plot along with the contribution from the middle of the structure with the end pair contributions removed. The edge pairs again appear to be the culprits mainly responsible for the backscattered field.

Bistatic patterns at 3.0 GHz are shown in Figure 64. The top plot shows the field from the total structure which has not decreased in level from what was seen in Figure 60. The middle plot shows the contribution from the center of the structure, which is seen to be very small in the backscatter direction. The bottom plot again confirms that the edge pairs are the dominant contributors to the scattered fields. Since the problem seems to lie in the edge pairs, they will be examined further.

Figure 65 shows the field contributed by the center pair of the structure on top and an edge pair on the bottom. Each pair is further broken down into the contributions from its front element and from its groundplane element. The center pair reacts as if it were in an infinite array as is expected. The edge pair elements are not resonant at the desired frequency. Both the front and groundplane element are resonant at a lower frequency implying that they may be longer than they need to be, again as is expected. The elements need not be resonant at 3.0 GHz as long as their contributions still cancel at 3.0 GHz, but that is not the case.

Another way to look at how the center and edge pairs differ is to examine their bistatic field patterns as shown in Figure 66. The center pair exhibits a cardioid

110
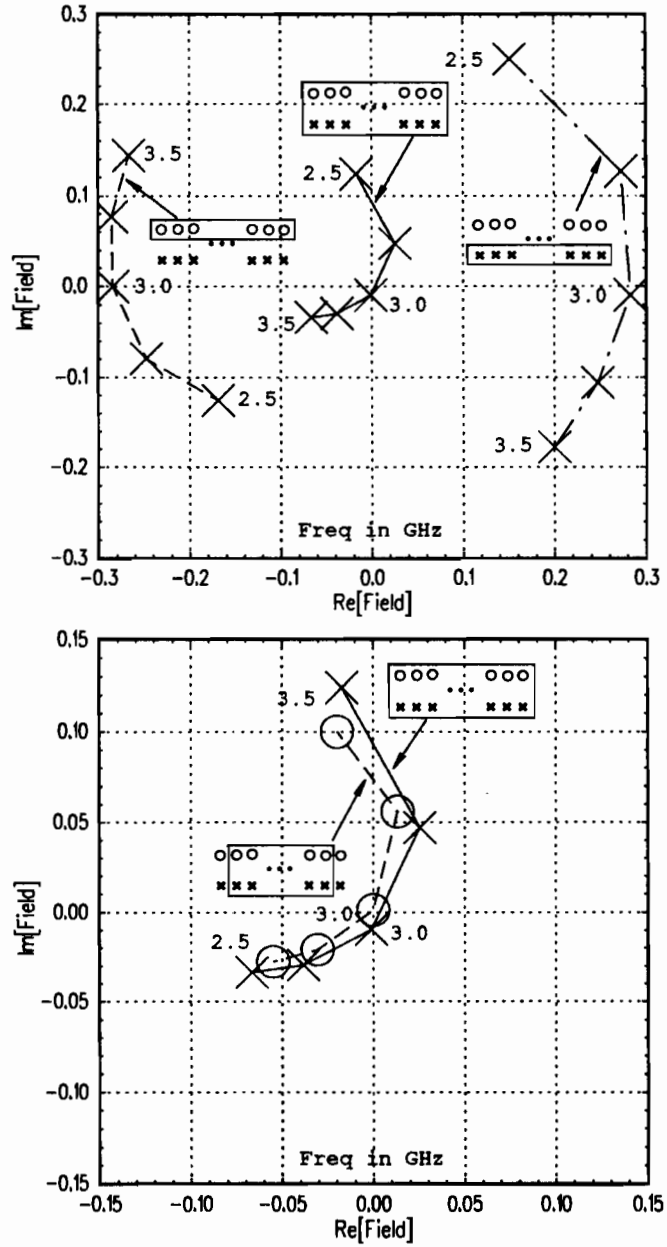
Figure 63: Complex backscattered field from the modified geometry. Top: Total structure fields and contributions from the front array and groundplane separately. Bottom: Total structure fields and contribution from the center part omitting the edge pairs.
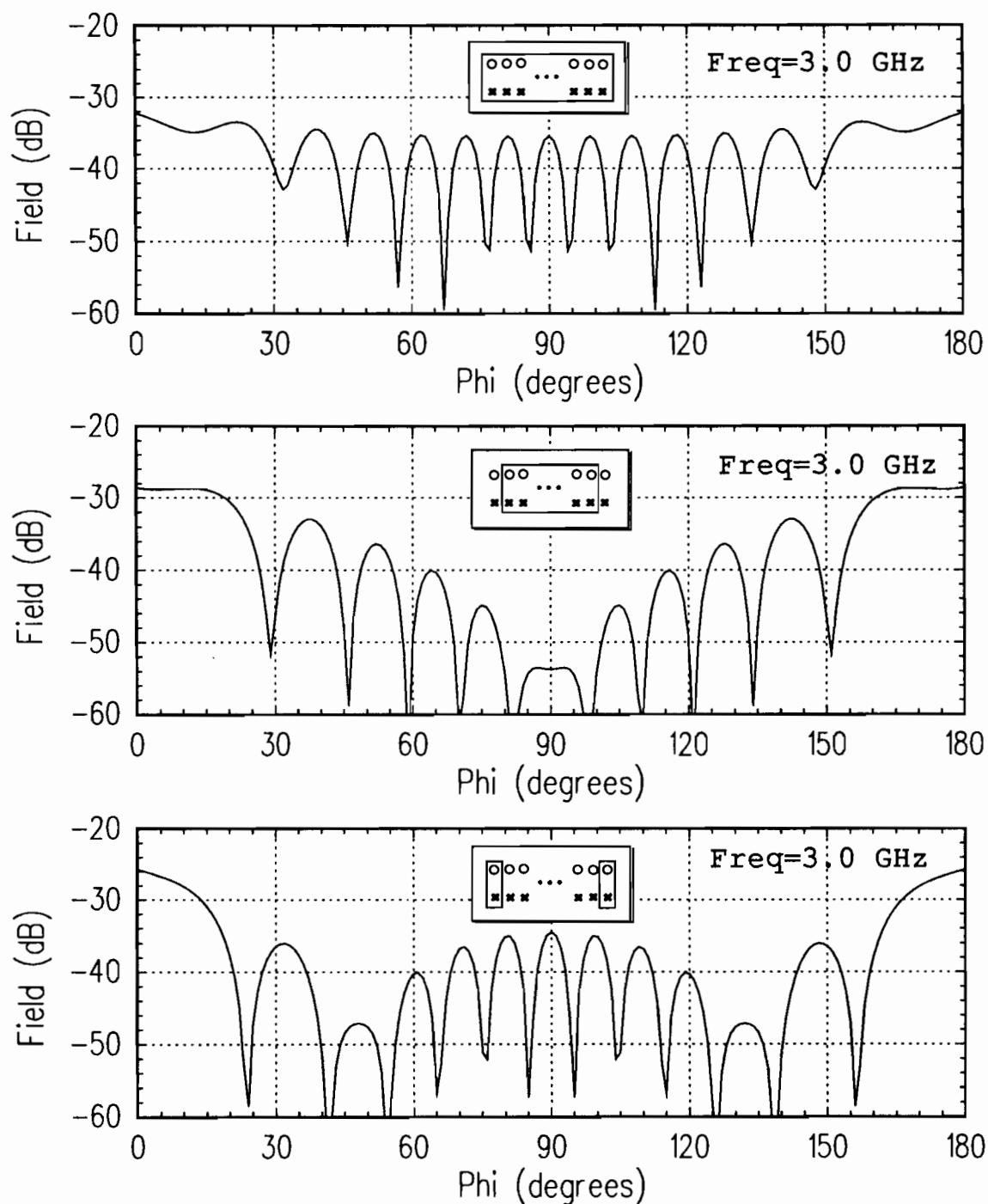
Figure 64: Bistatic scattered field from the modified geometry at 3 GHz. Top: Total structure. Middle: Center contribution omitting edge pairs. Bottom: Contribution from the edge pairs.

112
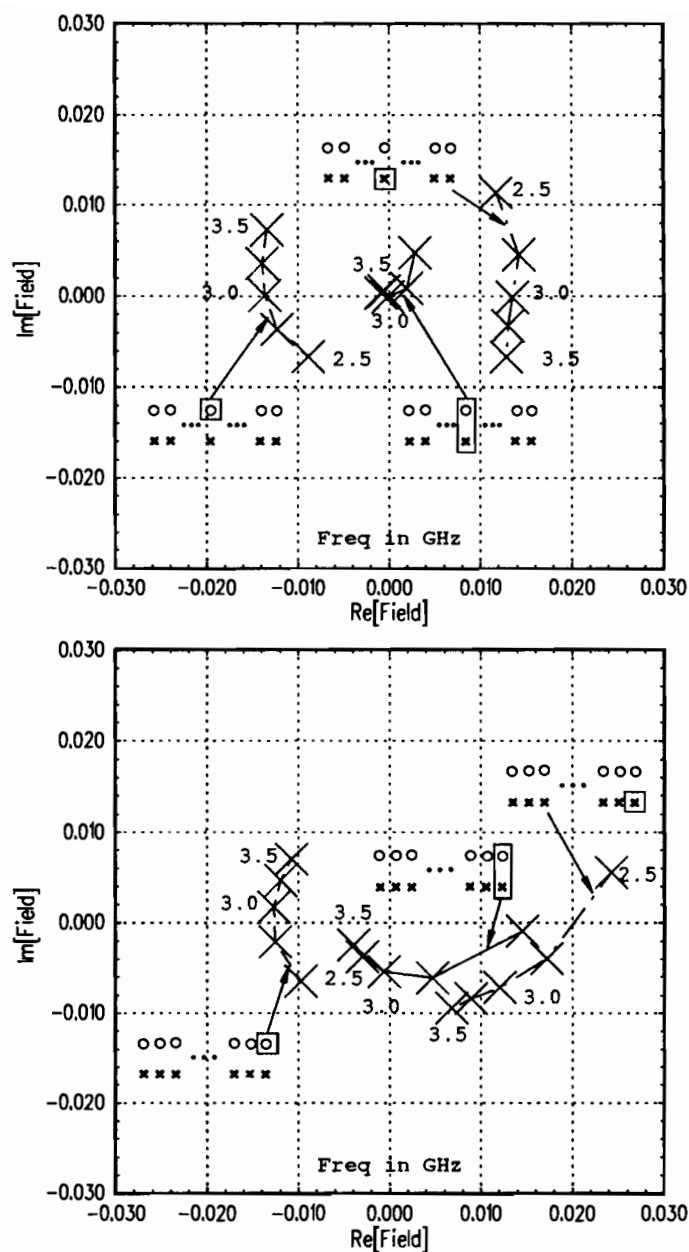
Figure 65: Complex backscattered fields from selected pairs of the modified geometry. Top: Central front/back duo. Bottom: Edge front/back duo.
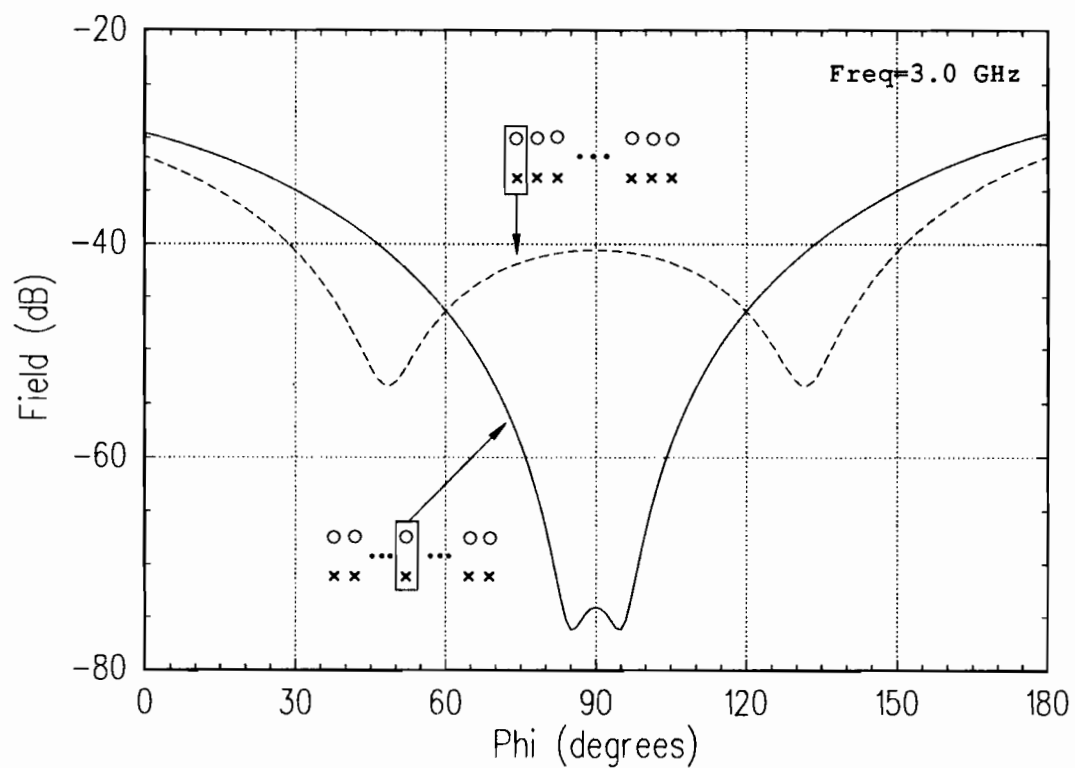
Figure 66: Bistatic scattered fields from center and edge duos of the modified geometry.

Front array

$1=5.32$cm, radius$=0.01$cm, $Z_L=272.4$ Ω

$1=5.58$cm, radius$=0.06$cm, $Z_L=0$ Ω

Ground plane

$1=4.82$cm
radius$=0.06$cm
$Z_L=30$ Ω

$1=4.82$cm
radius$=0.06$cm
$Z_L=30$ Ω

Figure 67: Edge treatment geometry.

pattern where the contributions from the front element and groundplane element cancel in the backscatter direction. The pattern from the edge pair is seen to be filled in, in the backscatter direction. This is a result of the front and groundplane edge elements not having currents in the proper magnitude ratio or phase relationship as seen in Figure 62. The next course of action is to attempt to fix the problem, bearing in mind that altering one element can have repercussions elsewhere in the array.

5.4   Edge Element Modifications

One approach to reducing the total backscattered field is shown in Figure 67. In this approach, only the edge elements of the groundplane were altered by shortening their length and applying a small resistive load. The resulting currents are shown in

115

Figure 68. Shortening the edge element results in a higher current on that element and lowers the current on the adjacent element. Applying a resistive load lowers the current on the edge element somewhat but the load applied was not large enough to return it to its original level as that was not the desired goal. Shortening the groundplane edge element also significantly altered the current phase on both the groundplane edge element and the front array edge element such that they are now more in line with the rest of the elements. The phases of the adjacent elements have also been shifted.

Figure 69 shows the backscattered field for this structure in the complex plane. The net contribution from the front array and the net contribution from the ground-plane array are both resonant at 3.0 GHz and of equal magnitude and opposite phase such that they cancel at the center frequency of 3.0 GHz. The bottom plot shows the backscattered field from the total structure and from the structure minus the contributions from the edge pairs. For this case, the total structure curve passes through the origin and the central part of the array is no longer matched.

Figure 70 shows the fields scattered from the center and edge pairs. The center pair still appears to be matched much better than the edge pair. This is confirmed by looking at the bistatic fields arising from each pair in Figure 71. The edge pair is matched better than it was in Figure 66 but it does not resemble a central pair. Is this contradictory to the front array contribution cancelling the groundplane array contribution in Figure 69? Perhaps the question is more easily answered by looking at the bistatic fields from the total structure at the top of Figure 72. The backscattered field from the total structure has indeed been reduced substantially at the desired frequency. The manner in which this was achieved is seen by examining the middle and bottom plots. The middle plot shows that the contribution from the center part of the structure has increased but it is of the same magnitude as the
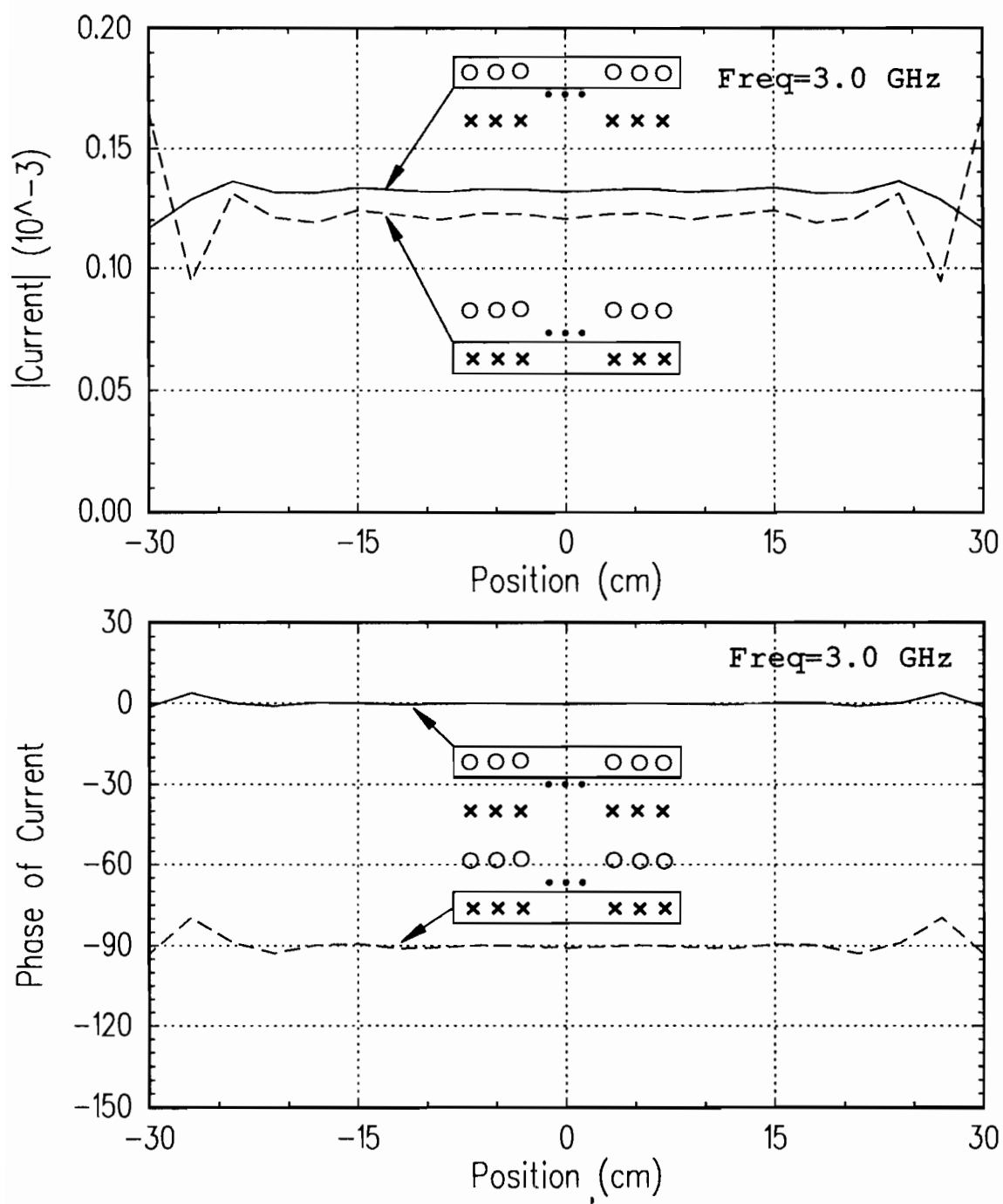
Figure 68: Currents from the edge treated case. Top: Magnitude in amps. Bottom: Phase in degrees.
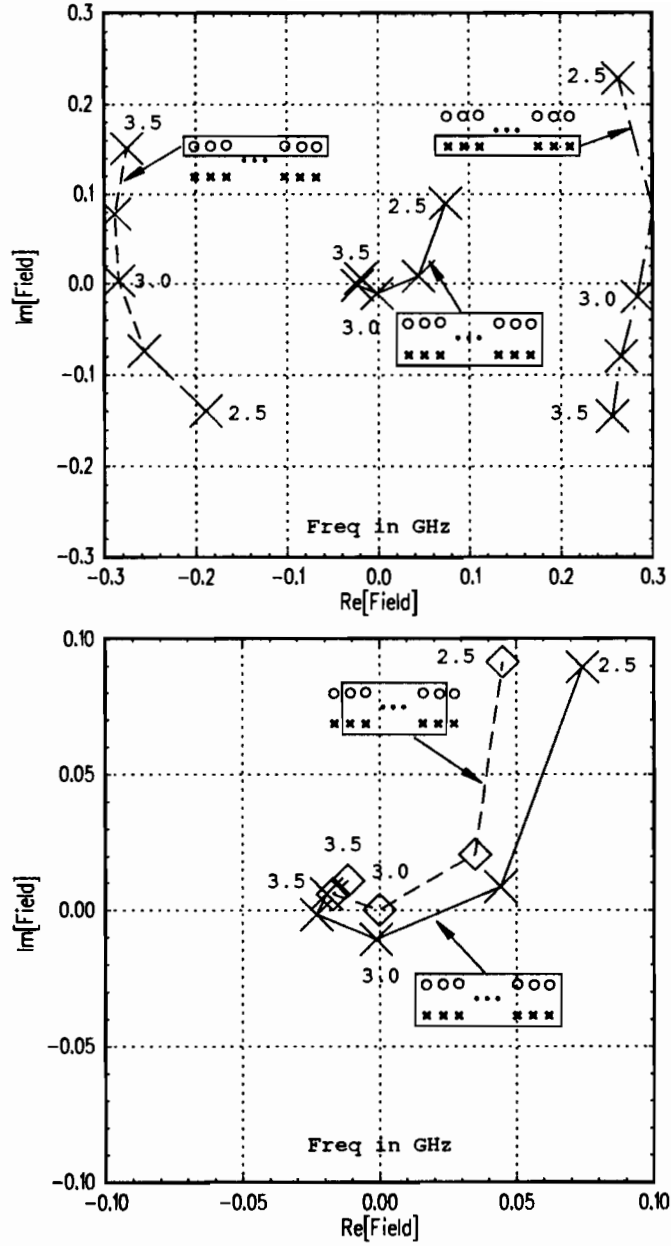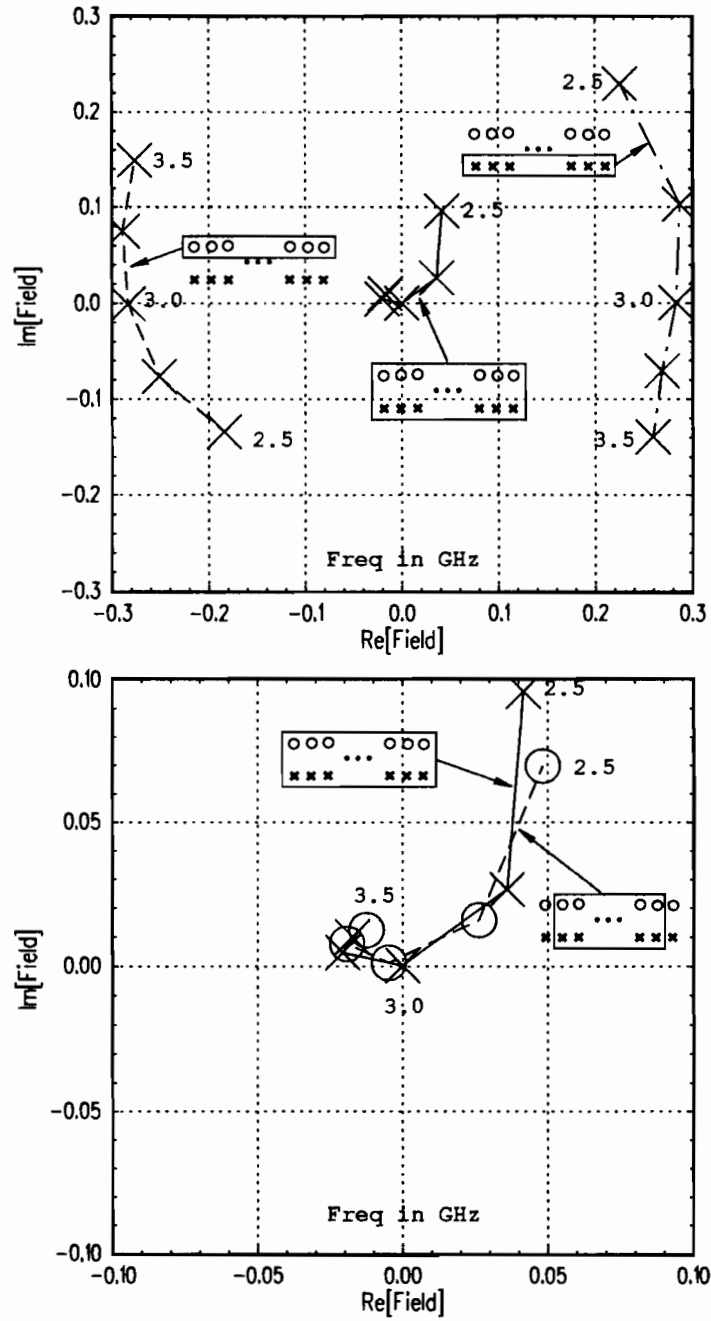
Figure 69: Complex backscattered fields from the edge treated case. Top: Total structure fields and contributions from the front array and groundplane separately. Bottom: Total structure fields and contribution from the center part omitting the edge pairs.
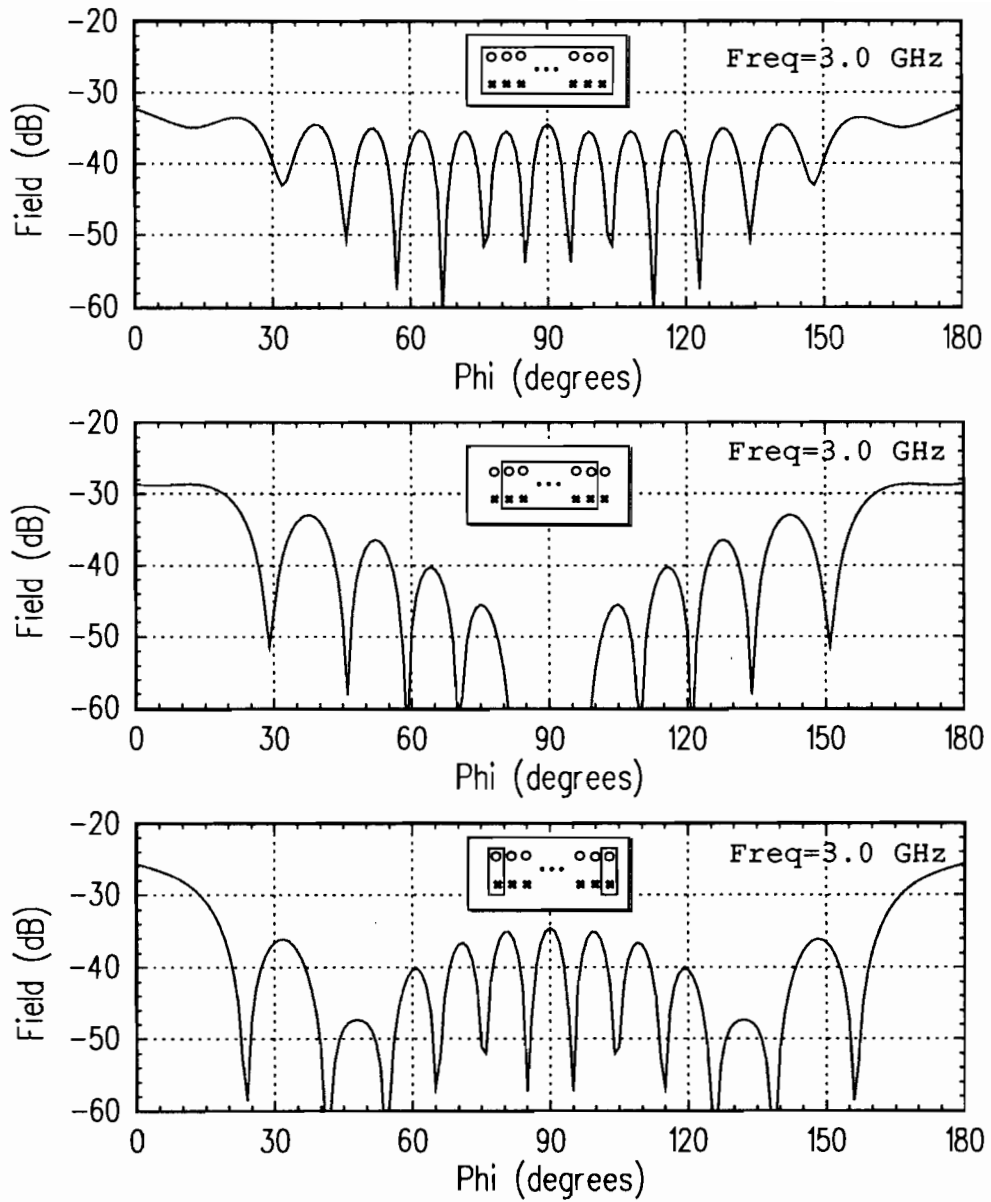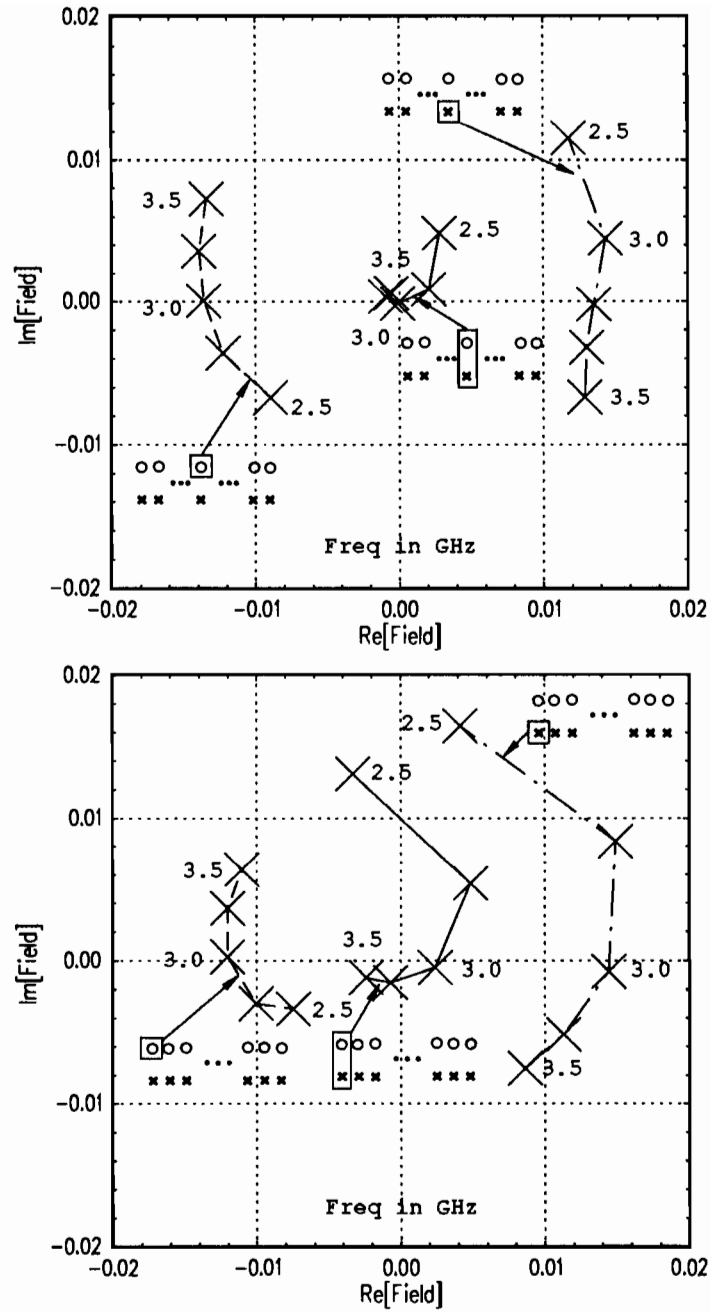
Figure 70: Complex backscattered fields from selected pairs of the edge treated case. Top: Central front/back duo. Bottom: Edge front/back duo.

119
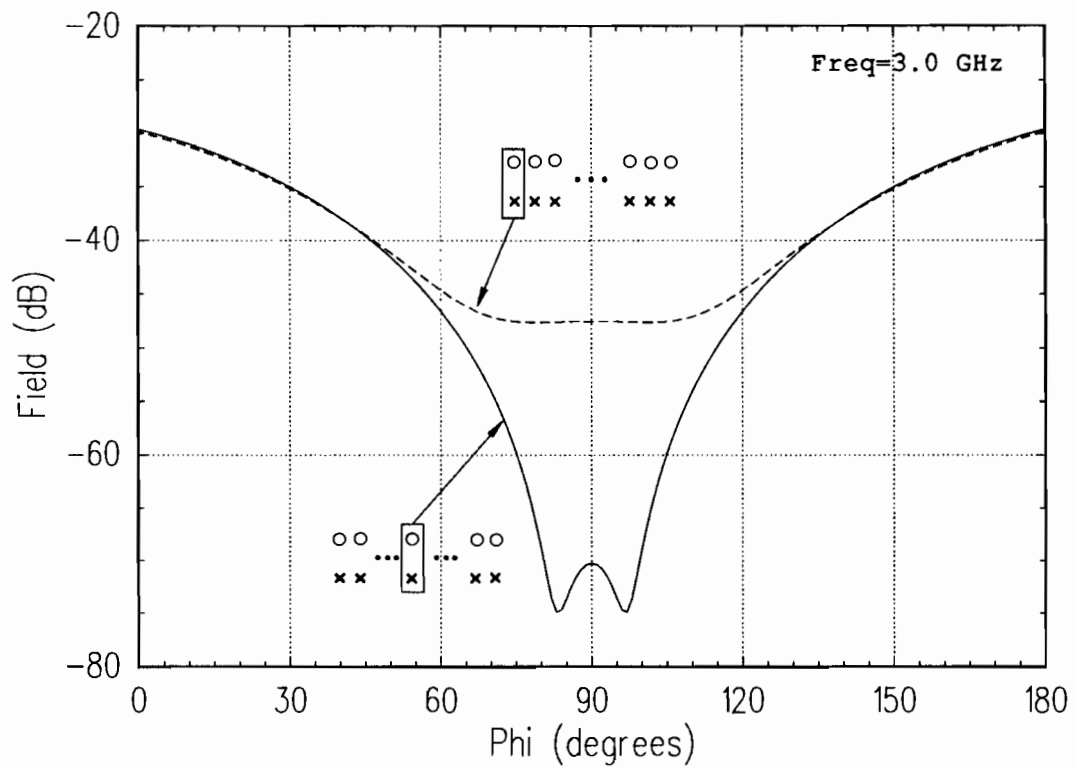
Figure 71: Bistatic scattered fields from the center and edge duos of the edge treated case.
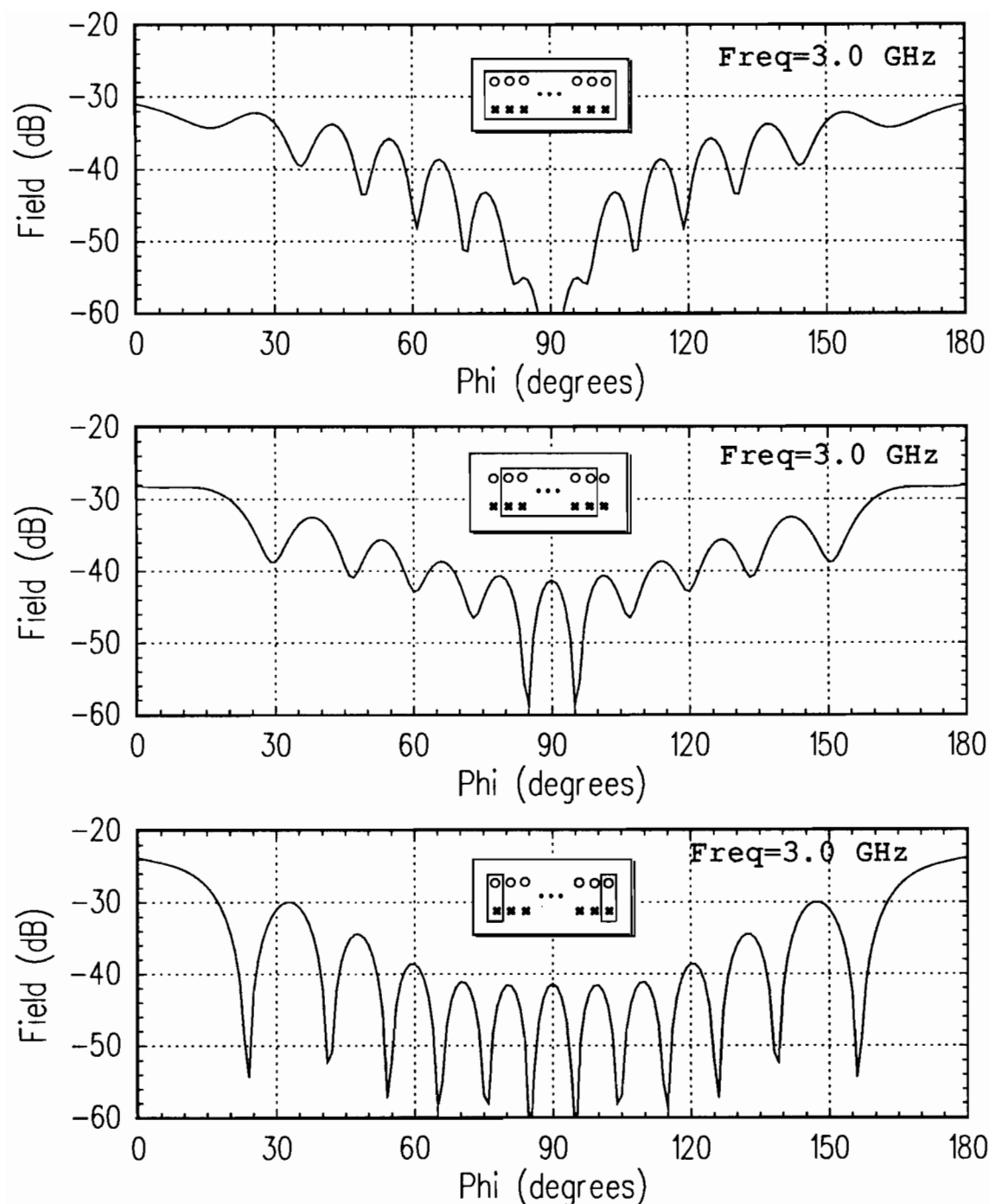
Figure 72: Bistatic scattered field from the edge treated case at 3 GHz. Top: Total structure. Middle: Center contribution omitting edge pairs. Bottom: Contribution from the edge pairs.
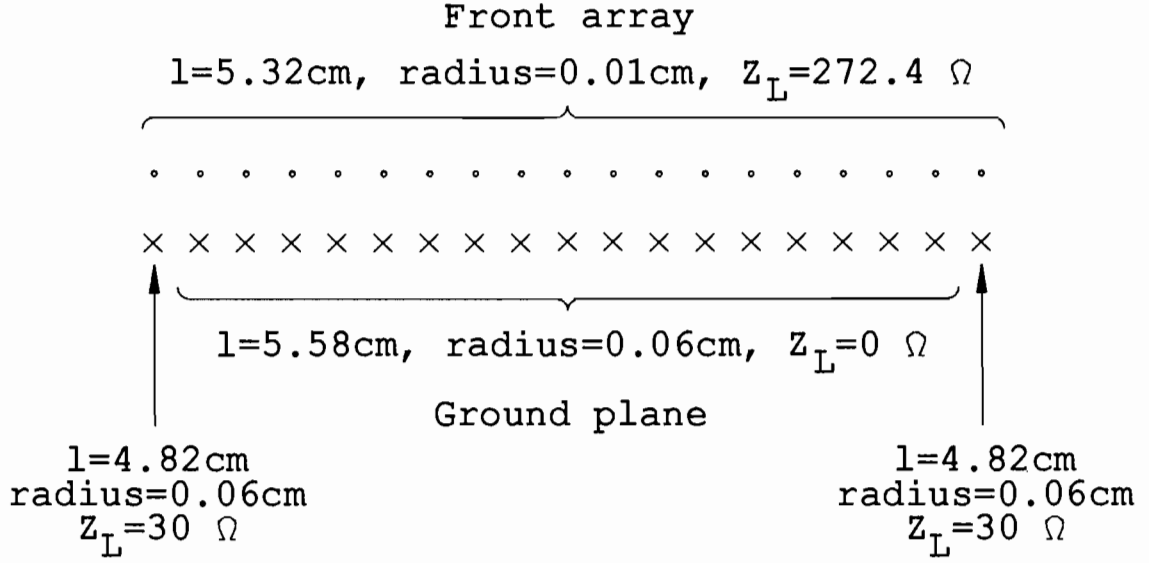
121

contribution from the edge pairs as shown in the bottom plot. The two contributions are of equal magnitude but of opposite phase resulting in a low total.

The broadside null is therefore achieved as desired but it was not achieved by cancelling every front element contribution with its corresponding groundplane element contribution. Modifying the edge elements affected the center part of the structure changing it from a "perfect" absorber to a very good one. The residual backscattered field coming from the center part of the structure is then cancelled by the contribution of the edge pairs. Overall this is seen to be a zero sum game and the final desired result may be achieved in different ways.

This design achieves a very limited goal of no backscattered field at a single frequency and a single angle of incidence. The limited angular capability is seen in Figure 72 and the limited frequency response is seen in Figure 73. Comparing the middle and bottom plots of Figure 73, the limited effectiveness of the edge modification used is obvious. This is not and was not meant to be a practical design to be used for any particular purpose. It is very sensitive to having precise dimensions and precise load values that are probably not achievable and certainly not maintainable, however that is not to say that a good design is not achievable in any manner.

This chapter gives an example of a particular class of structures where the truncation effects can predominate. It also shows that it may be possible to reduce these effects and that the lessons learned from the variation of properties in a single column of elements are directly applicable to the design of a larger and more complex structure.
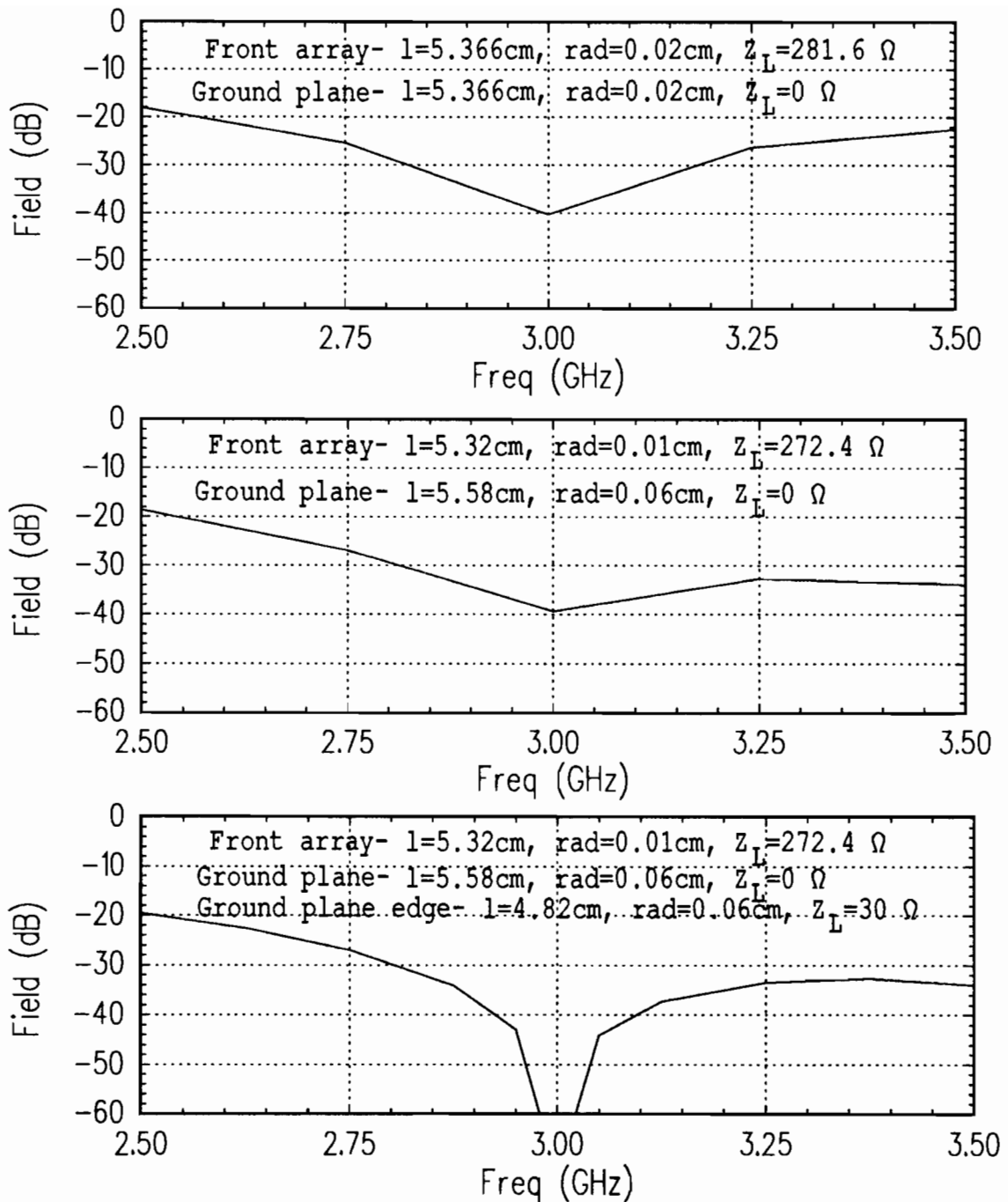
Figure 73: Magnitude of the backscattered field vs. frequency. Top: Groundplane plus resistive layer. Middle: Modified radius geometry. Bottom: Edge treated case.

CHAPTER VI

Conclusions

The underlying theory for calculating the scattered fields from infinite periodic linear arrays was presented and used to define self and mutual impedances between arrays of general V-dipole elements. A generalized Ohmic equation was formed, solved for the current coefficients and the resulting fields found.

Simple examples were introduced first to gain a basic understanding of how various element parameters and interelement spacing affect the resultant scattered fields. It was seen that fatter elements lead to greater bandwidth in general for single columns. Reduced interelement spacing also leads to greater bandwidth, but while axial elements become shorter, transverse elements must become longer to maintain a given resonance frequency. Adding a dielectric coating is equivalent to adding a capacitive load, but the loading effect is much stronger at the ends of an element than at the center.

Scattered fields from three frequency selective surfaces were found and compared to predicted results using diffraction theory, physical optics and infinite planar approximations. At the resonant frequency of the elements, all three simple methods did a fairly good job of predicting the scattered field. The simple single diffraction approach did particularly well with axial elements at resonance provided an appropriate strip width was used. Unfortunately it was not discernible as to what the strip width should be before doing the rigorous calculations. Also, at resonance, the physical optics solution and the infinite planar array approximations were quite

close. This is to be expected since both make a uniform current assumption and the surface resembles a solid conductor at resonance. Off of resonance the simple diffraction and physical optics approaches quickly lost accuracy. This is seen to be especially significant in surfaces that use the interelement interactions to create transmission bands. Overall the infinite array approximation was seen to hold up quite well for the single layer FSS designs shown, implying that the truncation effects were relatively minor.

A sample design was given in Chapter V of a structure that is strongly dominated by truncation effects. One could say that the scattering was coming from the edges but that is not entirely correct. The scattered field from each column of the structure is seen to be roughly of the same magnitude, but at the center of the structure each column of elements has a field cancelling counterpart, while at the edge of the structure the cancellation is flawed. Using the lessons learned in analyzing single columns, the design was altered to yield more desirable results. First, an attempt was made to match the bandwidth of the front array and groundplane with limited success. Next, the edge element of the groundplane was modified, producing a null in the backscattered field at the desired frequency and incidence angle.

From a practitioners point of view, for structures with dimensions on the order of three wavelengths or longer and non-radical curvature, the best approach would be to do all preliminary design work assuming an infinite planar structure. If truncation or curvature effects are significant, this will provide a good starting place for the design and it will also lead to a better understanding of the dominant scattering mechanisms. If the structure is not so large as to be computationally prohibited, the entire structure can be modeled as a finite by infinite structure along one axis, then on the other, and the design fine tuned. If the structure is large, it was seen that the truncation effects are generally limited to the edge regions with the affected

areas increasing in size as the scan angle heads toward grazing. Bearing that in mind, fine tuning the edge elements can first be done on a smaller structure and the results then transferred to a larger model to save computation time.

The results obtained have been quite satisfactory, which of course leads to a desire for more. The approach taken and the resulting computer code have thus far been seen to be effective at modeling truncation effects and this approach should also be effective at modeling singly curved surfaces with small radii of curvature. Thin dielectric coatings can be applied and the packing density of the elements increased to alleviate grating lobe problems, but it would be very interesting to include dielectric layers, which are often used to stabilize performance with scan angle. This could perhaps be done initially with infinite planar sheets, as it is an easier problem, and eventually be expanded to include finite dielectric layers. Also, the computational efficiency of the current program could be improved. A likely target for quick gains is the method in which the numerical integration is completed in the spectral domain. Special cases, such as straight axially or transversely oriented elements, could be singled out for specialized treatment which is not currently being done.

The addition of infinite periodic linear arrays to the repertoire of tools currently available for periodic structures enhances those tools and expands the analysis capability to new classes of problems, such as edge treatments or cylindrical surfaces with small radii of curvature. The research thus far has proven to be quite fruitful suggesting that further research and enhancements should be pursued.

APPENDIX A

Equivalent Currents and Reaction

The basic underlying premise to the field solutions proposed herein lie in the concepts of Schelkunoff's equivalent currents [25] and Rumsey's reaction [26].

The Schelkunoff equivalent currents are most readily described using the following diagrams. In Figure 74 the original problem is shown as a scatterer and source $(\bar{J}^i, \overline{M}^i)$ which generates the field $(\overline{E}, \overline{H})$ in the presence of the scatterer. Electric and magnetic currents can be placed on the surface S of the scatterer such that a null field will exist internal to the scatterer and the field external to S will remain as $(\overline{E}, \overline{H})$. These currents are shown in Figure 74. Since the field is now zero inside of S, the scatterer can be replaced with the ambient medium to facilitate the calculation of the fields by using the Green's function applicable to that medium.

The total field $(\overline{E}, \overline{H})$ can now be viewed as the sum of the fields from the source with the scatterer not present $(\overline{E}^i, \overline{H}^i)$ and the fields from the surface currents $(\overline{E}^s, \overline{H}^s)$ known as the scattered fields.

$$\overline{E} = \overline{E}^i + \overline{E}^s \tag{A.1}$$

$$\overline{H} = \overline{H}^i + \overline{H}^s \tag{A.2}$$

Rumsey noted in his 1954 paper [26] that electromagnetic fields cannot be observed directly and defined an observable that he called reaction as:

$$\langle a, b \rangle = \int_{V_a} \left(\overline{E}^b \cdot \bar{J}^a - \overline{H}^b \cdot \overline{M}^a \right) dV = \langle b, a \rangle \quad \text{(by reciprocity)} \tag{A.3}$$
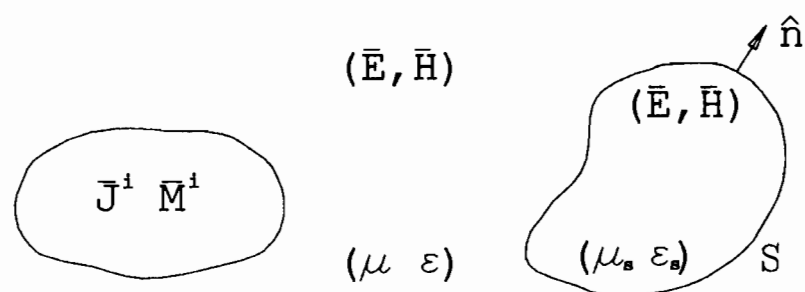
Original Problem
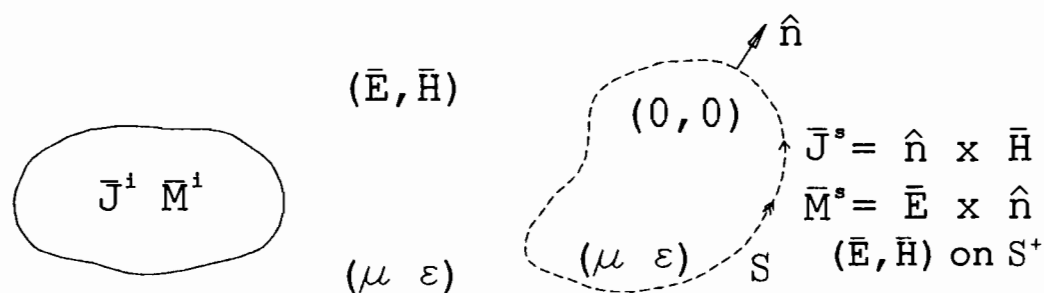
Equivalent Problem

$\bar{J}^s = \hat{n} \times \bar{H}$

$\bar{M}^s = \bar{E} \times \hat{n}$

$(\bar{E}, \bar{H})$ on S^+

Figure 74: Schelkunoff equivalent currents.
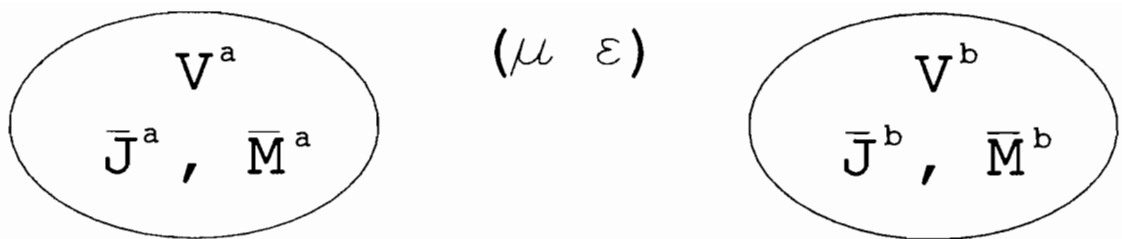
Figure 75: Rumsey's reaction between two volumetric sources.

where

$$V_a = \text{the volume containing the sources } \bar{J}^a \text{ and } \overline{M}^a \qquad (A.4)$$

$$V_b = \text{the volume containing the sources } \bar{J}^b \text{ and } \overline{M}^b \qquad (A.5)$$

$$\overline{E}^a, \overline{H}^a = \text{the fields generated by } \bar{J}^a, \overline{M}^a \qquad (A.6)$$

$$\overline{E}^b, \overline{H}^b = \text{the fields generated by } \bar{J}^b, \overline{M}^b \qquad (A.7)$$

This arrangement of sources is shown in Figure 75.

The concepts of equivalent currents and reaction can now be combined. Consider a test source $(\bar{J}^t, \overline{M}^t)$ placed interior to the scatterer as shown in Figure 76. The impressed currents $(\bar{J}^i, \overline{M}^i)$ and the equivalent currents $(\bar{J}^s, \overline{M}^s)$ can be consid-
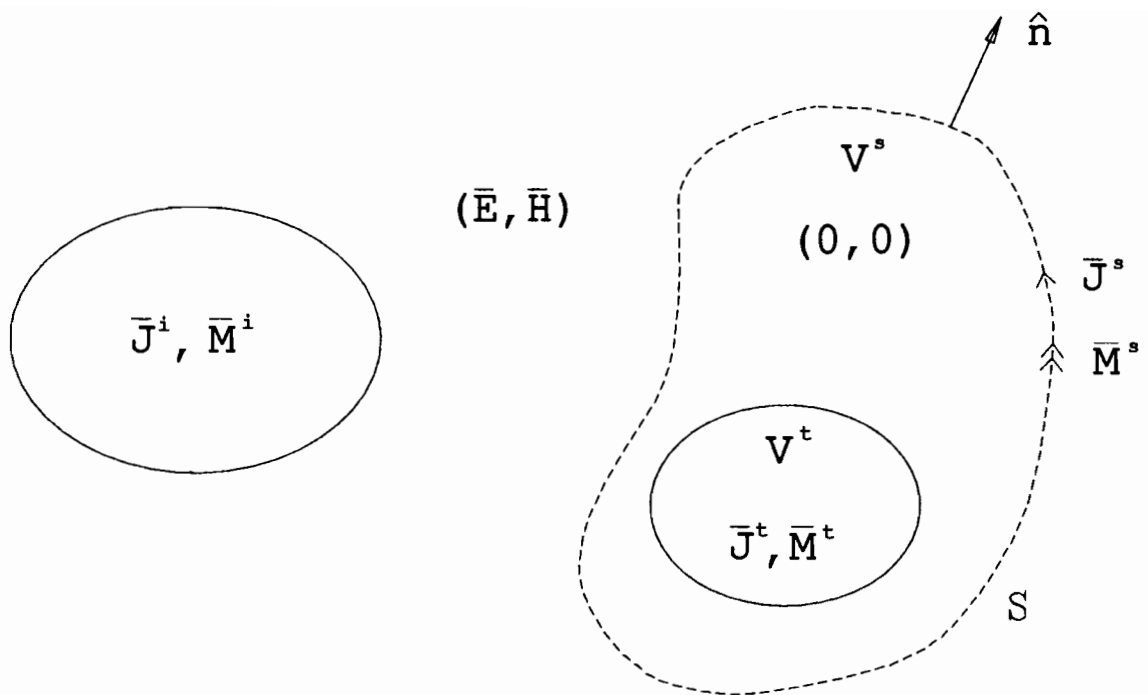
Figure 76: Test source placed interior to the scattering body.

ered as one source, the test currents $(\bar{J}^t, \overline{M}^t)$ as the second source and the reaction between the two found.

$$
\begin{aligned}
\langle i + s, t \rangle &= \langle i, t \rangle + \langle s, t \rangle \\
&= \int_{V_t} \left(\overline{E}^i \cdot \bar{J}^t - \overline{H}^i \cdot \overline{M}^t \right) dv + \int_{V_t} \left(\overline{E}^s \cdot \bar{J}^t - \overline{H}^s \cdot \overline{M}^t \right) dv \\
&= \int_{V_t} \left[\left(\overline{E}^i + \overline{E}^s \right) \cdot \bar{J}^t - \left(\overline{H}^i + \overline{H}^s \right) \cdot \overline{M}^t \right] dv \\
&= \int_{V_t} \left(\overline{E} \cdot \bar{J}^t - \overline{H} \cdot \overline{M}^t \right) dv \\
&= 0 \tag{A.8}
\end{aligned}
$$

The reaction is zero since the total field from the impressed and equivalent current is zero inside of the scatterer. This results in the reaction integral equation:

$$
\langle s, t \rangle = -\langle i, t \rangle = \langle t, s \rangle \quad \text{(by reciprocity)} \tag{A.9}
$$

$$
\int_S \left(\overline{E}^t \cdot \bar{J}^s - \overline{H}^t \cdot \overline{M}^s \right) ds = -\int_{V_t} \left(\overline{E}^i \cdot \bar{J}^t - \overline{H}^i \cdot \overline{M}^t \right) dv \tag{A.10}
$$

This is the equation that will be used in this investigation to solve for the equivalent surface currents which will then be used to find the scattered fields which are the desired results.

131

APPENDIX B

Thin Wire Approximation

Appendix A provides an overview of the integral equation to be used in solving this scattering problem. To make the problem tractable, a few approximations and a judicious choice of testing sources will be made. The V-dipoles will be constructed of "thin" wires which must obey a few simple rules if the approximation is to remain valid.

The test source is chosen to be a filamentary electric current on the wire axis and the wires are assumed to be circular in cross section. If the wire is very thin, the current can be assumed to be constant around the circumference of the wire and the current on the end caps can be ignored. These assumptions result in great simplification of the reaction integral equation (RIE) but of course, not without paying a price. The RIE is now reduced to:

$$\int I(l) \left[E_l^t - Z_s H_\phi^t \right] dl = V^t \tag{B.1}$$

where

$$\bar{J}^s(l) \;\; = \;\; \hat{l} \frac{I(l)}{2\pi a} \tag{B.2}$$

$$I(l) \;\; = \;\; \text{total wire current} \tag{B.3}$$

$$a \;\; = \;\; \text{wire radius} \tag{B.4}$$

$$\hat{l} \;\; = \;\; \text{unit vector on wire axis} \tag{B.5}$$

$$l \;\; = \;\; \text{metric along wire axis} \tag{B.6}$$

$$E_l^t = \frac{1}{2\pi} \int_0^{2\pi} \hat{l} \cdot \overline{E}^t d\phi \tag{B.7}$$

$$H_\phi^t = \frac{1}{2\pi} \int_0^{2\pi} \hat{\phi} \cdot \overline{H}^t d\phi \tag{B.8}$$

$$\overline{E}^t = \text{electric field from test filament} \tag{B.9}$$

$$\overline{H}^t = \text{magnetic field from the test filament} \tag{B.10}$$

$$Z_s = \text{surface impedance}$$

$$= -\frac{\beta}{j\omega\epsilon} \frac{J_0(\beta a)}{J_1(\beta a)} \tag{B.11}$$

$$\beta = \omega\sqrt{\mu_0(\epsilon - \epsilon_0)} \tag{B.12}$$

$$J_0, J_1 = \text{Bessel functions} \tag{B.13}$$

$$\overline{M}^s = Z_s \bar{J}^s \times \hat{n} = \hat{\phi} Z_s \frac{I(l)}{2\pi a} \tag{B.14}$$

$$V^t = -\int \overline{E}^i \cdot \bar{J}^t dl \tag{B.15}$$

Figure 77 shows the local wire coordinate system.

These approximations are extremely useful and many problems can be solved using them but care must be taken in their use. Richmond [21] recommended the following restrictions for the approximations to hold: 1) the wire radius should not exceed .007 wavelengths, 2) the ratio of the longest to shortest segments should be no greater than 100, 3) the ratio of the wire length to its diameter should be at least 30, 4) wires should not be bent to form an acute angle less than 30 degrees, and 5) no two wires should pass within a few wire radii of each other. These restrictions are somewhat conservative but obeying them will yield more accurate solutions and faster convergence.

133

$$\hat{l} \times \hat{n} = \hat{\varphi}$$
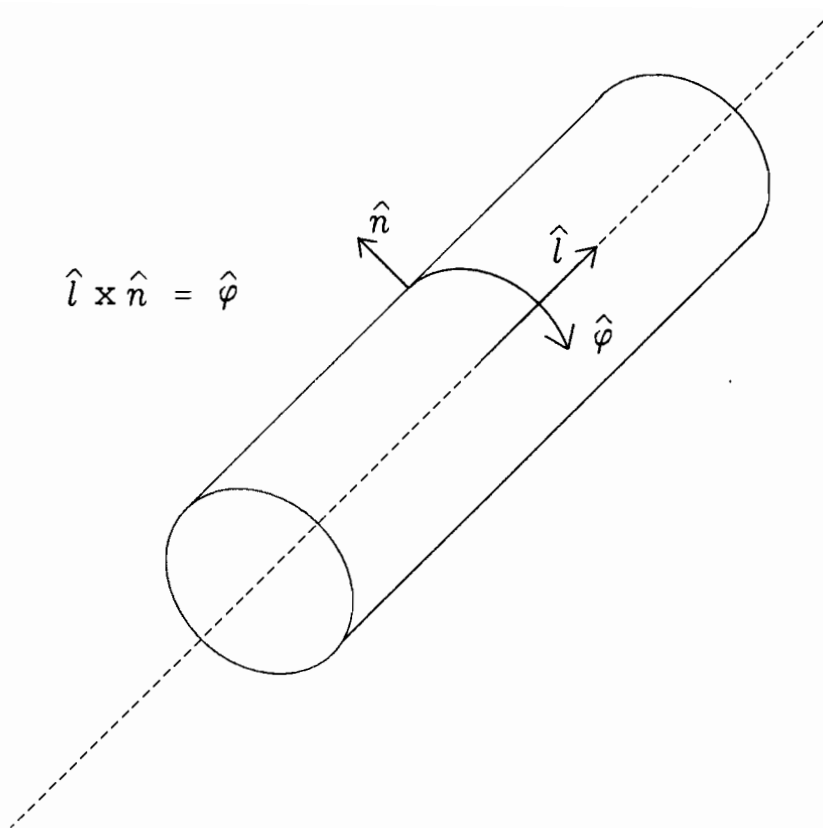
Figure 77: Local wire coordinates.

APPENDIX C

Coordinate References

The coordinates to be used throughout this dissertation are as shown in Figure 78. Each dipole is designated by three points given in rectangular coordinates as (x_1, y_1, z_1), (x_2, y_2, z_2) and (x_3, y_3, z_3). The assumed current direction is from (1) to (2) to (3). Each leg of the dipole will be assigned direction vectors as follows: the "a" leg will have the direction vector:

$$\hat{p}^{(a)} = p_{ax}\hat{x} + p_{ay}\hat{y} + p_{az}\hat{z} \tag{C.1}$$

where

$$p_{ax} = \frac{x_3 - x_2}{|\bar{p}^{(a)}|} \tag{C.2}$$

$$p_{ay} = \frac{y_3 - y_2}{|\bar{p}^{(a)}|} \tag{C.3}$$

$$p_{az} = \frac{z_3 - z_2}{|\bar{p}^{(a)}|} \tag{C.4}$$

$$|\bar{p}^{(a)}| = \sqrt{(x_3 - x_2)^2 + (y_3 - y_2)^2 + (z_3 - z_2)^2} \tag{C.5}$$

and the "b" leg will have the direction vector

$$\hat{p}^{(b)} = p_{bx}\hat{x} + p_{by}\hat{y} + p_{bz}\hat{z} \tag{C.6}$$

where

$$p_{bx} = \frac{x_2 - x_1}{|\bar{p}^{(b)}|} \tag{C.7}$$
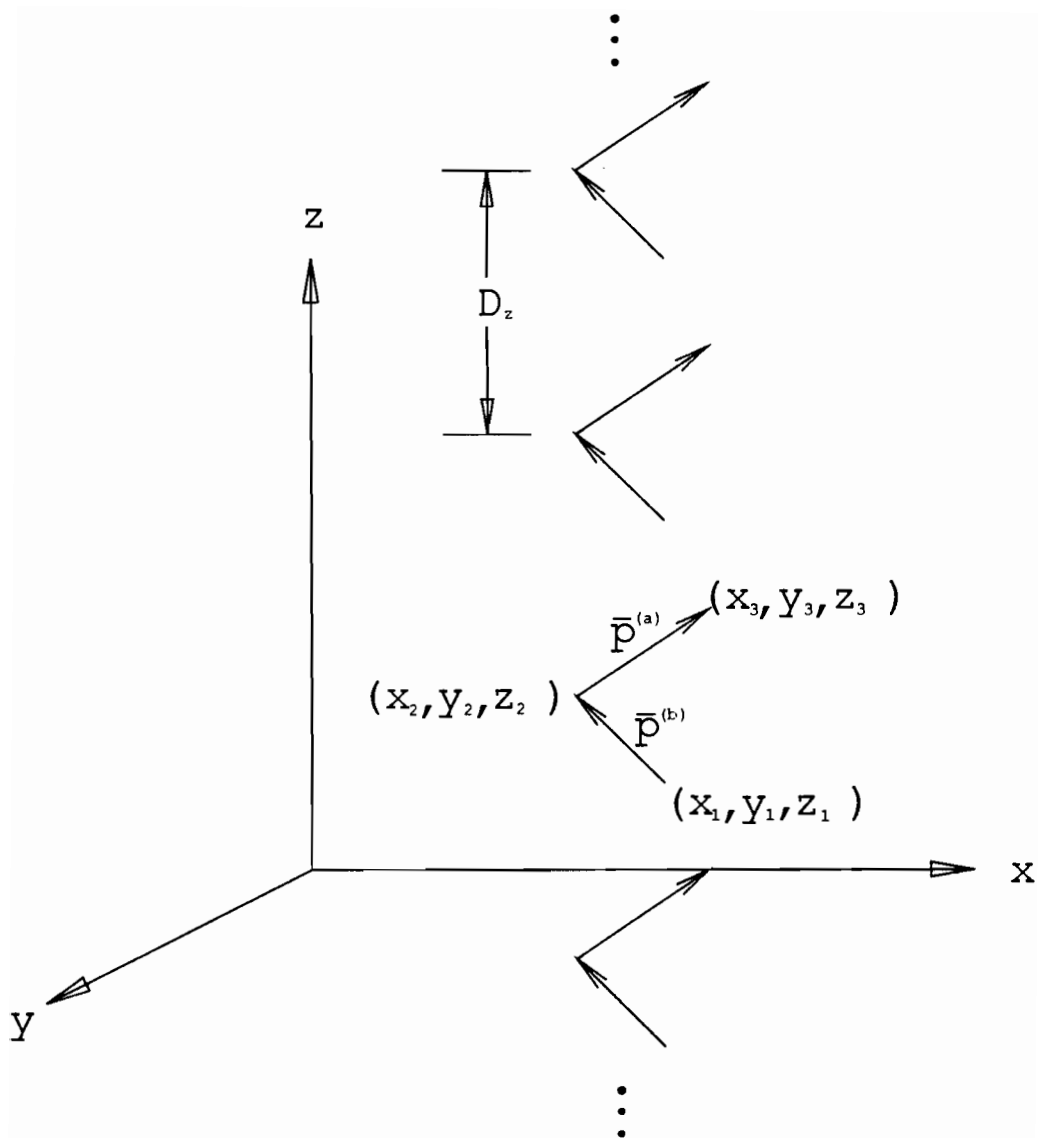
Figure 78: Coordinates for an infinite, periodic column of V-dipoles.

$$p_{by} = \frac{y_2 - y_1}{|\bar{p}^{(b)}|} \tag{C.8}$$

$$p_{bz} = \frac{z_2 - z_1}{|\bar{p}^{(b)}|} \tag{C.9}$$

$$|\bar{p}^{(b)}| = \sqrt{(x_2 - x_1)^2 + (y_2 - y_1)^2 + (z_2 - z_1)^2} \tag{C.10}$$

It will also be convenient to define local variables l_a and l_b which represent the length along a dipole leg from the bend point. Any point on the dipole (x', y', z') can be given in terms of the local variables as

$$x' = \begin{cases} x_2 + p_{ax}l_a & \text{on leg a} \\ x_2 - p_{bx}l_b & \text{on leg b} \end{cases} \tag{C.11}$$

$$y' = \begin{cases} y_2 + p_{ay}l_a & \text{on leg a} \\ y_2 - p_{by}l_b & \text{on leg b} \end{cases} \tag{C.12}$$

$$z' = \begin{cases} z_2 + p_{az}l_a & \text{on leg a} \\ z_2 - p_{bz}l_b & \text{on leg b} \end{cases} \tag{C.13}$$

The arrays are assumed to be periodic in the z direction with periodicity D_z.

137

APPENDIX D

Near-Zone Field of Sinusoidal Line Source

Consider an electric line source located on the z axis with endpoints at z_1 and z_2 as shown in Figure 79. Two of these "monopoles" can be arranged to form a V dipole. The filamentary V dipole is of interest because it is employed as the test source in the sinusoidal reaction technique for thin-wire structures.

Let the electric monopole have the following current distribution:

$$I(z) \;=\; \frac{I_1 \sinh \gamma(z_2 - z) + I_2 \sinh \gamma(z - z_1)}{\sinh \gamma d} \tag{D.1}$$

where I_1 and I_2 are the endpoint currents, γ is the complex propagation constant of the medium, $d = z_2 - z_1$ is the source length and the time dependence e^{st} is understood. The medium is considered to be homogeneous with complex parameters μ and ϵ. The cylindrical components of the field are $E_\phi = 0$ and

$$\begin{aligned}
E_\rho \;=\; \frac{\eta}{4\pi\rho \sinh \gamma d} &\left[\left(I_1 e^{-\gamma R_1} - I_2 e^{-\gamma R_2} \right) \sinh \gamma d \right.\\
&+ \left(\gamma I_1 \cosh \gamma d - I_2 \right) e^{-\gamma R_1} \cos \theta_1 \\
&\left.+ \left(I_2 \cosh \gamma d - I_1 \right) e^{-\gamma R_2} \cos \theta_2 \right]
\end{aligned} \tag{D.2}$$

$$E_z \;=\; \frac{\eta}{4\pi \sinh \gamma d} \left[(I_1 - I_2 \cosh \gamma d) \frac{e^{-\gamma R_2}}{R_2} + (I_2 - I_1 \cosh \gamma d) \frac{e^{-\gamma R_1}}{R_1} \right] \tag{D.3}$$

$$\begin{aligned}
\overline{H} \;=\; \frac{\hat{\phi}}{4\pi\rho \sinh \gamma d} &\left[(I_1 \cos \theta_1 \sinh \gamma d + I_1 \cosh \gamma d - I_2) e^{-\gamma R_1} \right.\\
&\left.- (I_2 \cos \theta_2 \sinh \gamma d - I_2 \cosh \gamma d + I_1) e^{-\gamma R_2} \right]
\end{aligned} \tag{D.4}$$

138
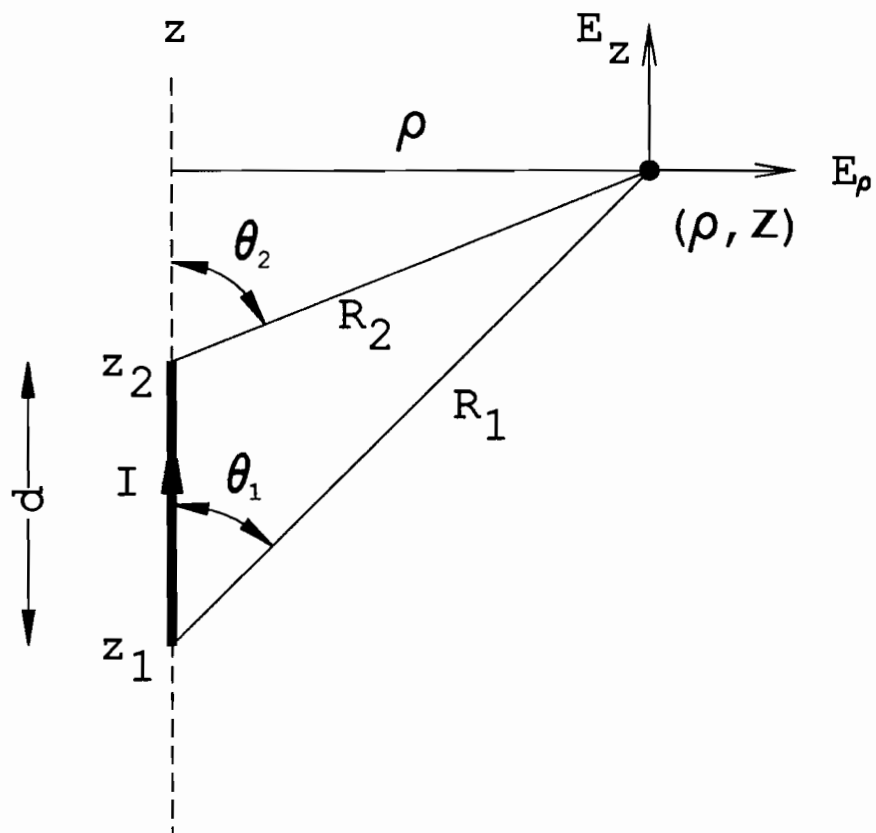
Figure 79: An electric line source on the z axis and the observation point at (ρ, z).

where η is the intrinsic impedance of the medium:

$$\eta \;=\; \sqrt{\mu/\epsilon} \qquad\qquad\qquad \text{(D.5)}$$

These expressions exclude the field contributions from the point charges at the endpoints of the line source, since these charges disappear when two monopoles are connected to form a dipole. For a V dipole, scalar addition applies to the cartesian components (E_x, E_y, E_z) of the field generated by each of the monopoles.

APPENDIX E

The Field from a Column of Hertzian Elements

The following approach will be taken in finding the scattered fields. The ambient medium is taken to be linear, homogeneous and isotropic. The fields are assumed to be time harmonic with an $e^{+j\omega t}$ time convention that will hereafter be suppressed in all formulations.

The vector potential for a single Hertzian current element is given by [38]:

$$d\bar{A} \;=\; \hat{p}\,I\,dl\,\frac{e^{-j\beta R}}{4\pi R}$$

where

$$\hat{p} \;=\; \text{element direction vector} \tag{E.1}$$

$$I \;=\; \text{element current} \tag{E.2}$$

$$dl \;=\; \text{element length} \tag{E.3}$$

$$R \;=\; |\bar{r} - \bar{r}'| \tag{E.4}$$

$$\bar{r} \;=\; \text{field point} \tag{E.5}$$

$$\bar{r}' \;=\; \text{source point} \tag{E.6}$$

$$\beta \;=\; \text{wave number of the ambient medium} \tag{E.7}$$

The total potential for a column of elements as in Figure 80 is:

$$d\bar{A} \;=\; \hat{p}\,\frac{dl}{4\pi}\sum_{m=-\infty}^{\infty} I_m \,\frac{e^{-j\beta R_m}}{R_m} \tag{E.8}$$

141
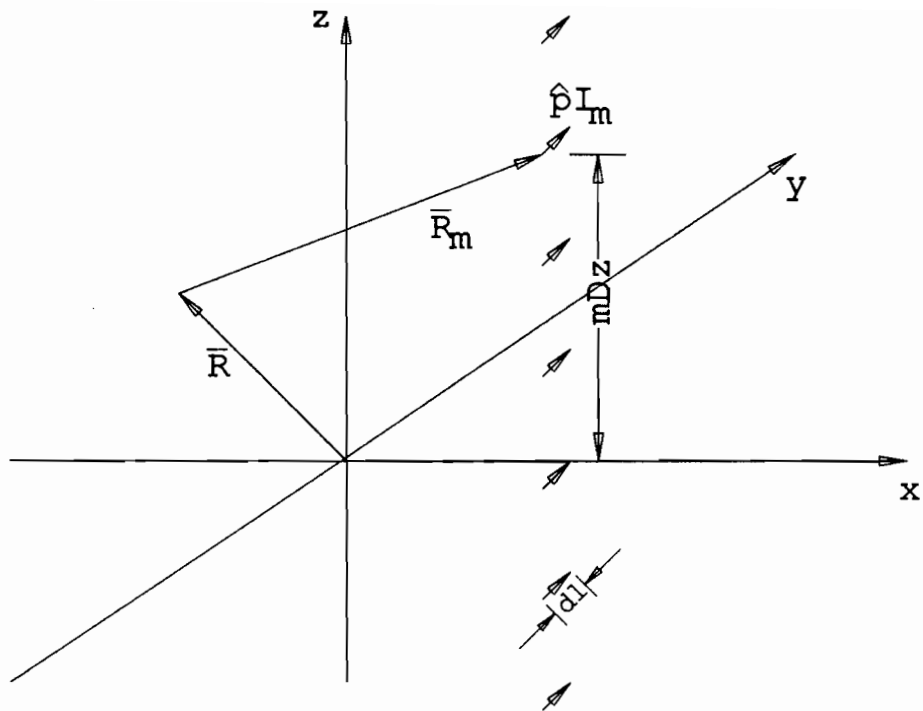
Figure 80: Column array of Hertzian dipoles.

where

$$I_m = \text{current of the } m^{th} \text{ element} \qquad (E.9)$$

$$R_m = \sqrt{\delta^2 + (z - z' - mD_z)^2} \qquad (E.10)$$

$$\delta^2 = (x - x')^2 + (y - y')^2 \qquad (E.11)$$

For plane wave incidence the periodicity of the problem allows for the invocation of Floquet's theorem which is given for a single dimension as:

$$I_m = I_0 e^{-j\beta mD_z s_z} \qquad (E.12)$$

where

$$\hat{s} \;=\; \hat{x}s_x + \hat{y}s_y + \hat{z}s_z \;=\; \text{plane wave direction} \tag{E.13}$$

$$D_z \;=\; \text{element to element spacing along the array axis} \tag{E.14}$$

Upon substitution this yields:

$$d\bar{A} \;=\; \hat{p}\,\frac{I_0 dl}{4\pi}\sum_{m=-\infty}^{\infty}\frac{e^{-j\beta R_m}}{R_m}\,e^{-j\beta m D_z s_z} \tag{E.15}$$

The electric and magnetic fields in a source free region are given by [38]:

$$\bar{E} \;=\; \frac{1}{j\omega\epsilon}\,\nabla \times \nabla \times \bar{A} \tag{E.16}$$

$$\bar{H} \;=\; \nabla \times \bar{A} \tag{E.17}$$

Using the vector potential derived above, the electric field for an infinite linear array of Hertzian elements is given in rectangular coordinates as:

$$d\bar{E}(\bar{R},\bar{R}') \;=\; -\frac{\eta}{4\pi}\sum_{m=-\infty}^{\infty}I_0 dl\, e^{-j\beta m D_z s_z}\,\frac{e^{-j\beta R_m}}{R_m^2}\left\{\left[(\hat{p}\times\hat{R}_m)\times\hat{R}_m\right]\gamma - 2\hat{p}\xi\right\} \tag{E.18}$$

where

$$\gamma \;=\; j\beta R_m + 3 + \frac{3}{j\beta R_m} \tag{E.19}$$

$$\xi \;=\; 1 + \frac{1}{j\beta R_m} \tag{E.20}$$

$$\hat{R}_m \;=\; \frac{\left[\hat{x}(x-x') + \hat{y}(y-y') + \hat{z}(z-z'-mD_z)\right]}{R_m} \tag{E.21}$$

$$\hat{p} \;=\; \hat{x}p_x + \hat{y}p_y + \hat{z}p_z \tag{E.22}$$

This will be termed the spatial domain approach. This series has been found to converge rather slowly and the convergence degrades as you move away from the array. To accelerate the convergence it is advantageous to transform the vector

potential via Poisson's sum formula as shown in Munk [7]. This results in a vector potential of:

$$d\bar{A} \;=\; \hat{p}\,\frac{Idl}{4jD_z}\sum_{n=-\infty}^{\infty}e^{-j\beta r_z(z-z')}\,H_0^{(2)}(\beta r_\rho\delta) \tag{E.23}$$

where

$$r_z \;=\; s_z + n\frac{\lambda}{D_z} \tag{E.24}$$

$$r_\rho \;=\; \sqrt{1-r_z^2} \tag{E.25}$$

which yields the following electric field for rectangular coordinates:

$$
\begin{aligned}
d\bar{E}(\bar{R},\bar{R}') \;=\; &-\frac{\eta}{4D_z}\sum_{n=-\infty}^{\infty}I_0 dl\,e^{-j\beta r_z(z-z')}\\
&\Bigg\{\hat{x}\;\;\Bigg[p_x\left(\beta r_\rho^2\frac{(y-y')^2}{\delta^2}H_0^{(2)}-\frac{r_\rho}{\delta}\left(\frac{2(y-y')^2}{\delta^2}-1\right)H_1^{(2)}+\beta r_z^2H_0^{(2)}\right)\\
&\quad+p_y\left(-\beta r_\rho^2\frac{(x-x')(y-y')}{\delta^2}H_0^{(2)}+\frac{2r_\rho(x-x')(y-y')}{\delta^3}H_1^{(2)}\right)\\
&\quad+p_z\left(j\beta r_z r_\rho\frac{(x-x')}{\delta}H_1^{(2)}\right)\Bigg]\\
&+\hat{y}\;\;\Bigg[p_x\left(-\beta r_\rho^2\frac{(x-x')(y-y')}{\delta^2}H_0^{(2)}+2r_\rho\frac{(x-x')(y-y')}{\delta^3}H_1^{(2)}\right)\\
&\quad+p_y\left(\beta r_\rho^2\frac{(x-x')^2}{\delta^2}H_0^{(2)}-\frac{r_\rho}{\delta}\left(\frac{2(x-x')^2}{\delta^2}-1\right)H_1^{(2)}+\beta r_z^2H_0^{(2)}\right)\\
&\quad+p_z\left(j\beta r_z r_\rho\frac{(y-y')}{\delta}H_1^{(2)}\right)\Bigg]\\
&+\hat{z}\;\;\Bigg[p_x\left(j\beta r_z r_\rho\frac{(x-x')}{\delta}H_1^{(2)}\right)\\
&\quad+p_y\left(j\beta r_z r_\rho\frac{(y-y')}{\delta}H_1^{(2)}\right)+p_z\beta r_\rho^2H_0^{(2)}\Bigg]\Bigg\}
\end{aligned}
\tag{E.26}
$$

where

$$\delta^2 \;=\; (x-x')^2 + (y-y')^2 \tag{E.27}$$

144

$$H_0^{(2)} = H_0^{(2)}(\beta r_\rho \delta) \tag{E.28}$$

$$H_1^{(2)} = H_1^{(2)}(\beta r_\rho \delta) \tag{E.29}$$

This will be termed the spectral domain approach.

The field from an array with a current distribution with constant direction $\hat{p}I^{(1)}(l)$ is found by integrating along the length of the element (the $\bar{R}'$ coordinates) or:

$$\bar{E}^{(1)}(\bar{R}) = \int_{element} d\bar{E}^{(1)}(\bar{R}, \bar{R}') \tag{E.30}$$

where

$$\bar{R} = \text{field point} \tag{E.31}$$

$$\bar{R}' = \text{source point on the element} \tag{E.32}$$

$$\bar{R}' = \bar{R}^{(1)} + \hat{p}\,dl \tag{E.33}$$

$$\bar{R}^{(1)} = \text{position of the element terminals} \tag{E.34}$$

APPENDIX F

Far Field

Equation (2.39) can be significantly simplified and perhaps be better understood if viewed in the "far field". For large arguments the Hankel function is given as

$$H_\nu^{(2)}(x) \xrightarrow{x \to \infty} \sqrt{\frac{2j}{\pi x}} j^\nu e^{-jx} \tag{F.1}$$

and also,

$$\delta = \sqrt{(x-x')^2 + (y-y')^2} = |\bar{\rho} - \bar{\rho}'| \xrightarrow{\rho \to \infty} \rho - x' \cos\phi - y' \sin\phi \tag{F.2}$$

$$\frac{x-x'}{\delta} \to \cos\phi \qquad \frac{y-y'}{\delta} \to \sin\phi \tag{F.3}$$

where

$$\rho, \phi = \text{field point coordinates} \tag{F.4}$$

$$\rho', \phi' = \text{source point coordinates} \tag{F.5}$$

Combining the above for the Hankel functions of interest yields

$$H_0^{(2)}\left(\beta r_\rho \delta\right) \xrightarrow{\beta r_\rho \delta \to \infty} \sqrt{\frac{2j}{\pi \eta r_\rho \rho}} e^{-j\beta r_\rho(\rho - x'\cos\phi - y'\sin\phi)} \tag{F.6}$$

$$H_1^{(2)}\left(\beta r_\rho \delta\right) \xrightarrow{\beta r_\rho \delta \to \infty} j\sqrt{\frac{2j}{\pi \eta r_\rho \rho}} e^{-j\beta r_\rho(\rho - x'\cos\phi - y'\sin\phi)} \tag{F.7}$$

These large argument approximations can now be substituted into Equation (2.39) yielding:

$$
\begin{aligned}
\overline{E}^a(x,y,z) \;=\; & -\frac{\eta\beta}{4D_z} \sum_{n=-\infty}^{\infty} \frac{e^{-j\beta r_\rho \rho}}{\sqrt{\beta r_\rho \rho}} \sqrt{\frac{2j}{\pi}}\, e^{-j\beta r_z z} \\[4pt]
& \cdot \int_0^A dl_a I^{(a)}(l_a) e^{j\beta r_z z'} e^{j\beta r_\rho (x'\cos\phi + y'\sin\phi)} \\[4pt]
& \Big\{ \hat{x}\left[p_{ax}\left(r_\rho^2 \sin^2\phi + r_z^2\right) - p_{ay}\left(r_\rho^2 \sin\phi\cos\phi\right) - p_{az}\left(r_z r_\rho \cos\phi\right) \right] \\[4pt]
& + \hat{y}\left[-p_{ax}\left(r_\rho^2 \sin\phi\cos\phi\right) + p_{ay}\left(r_\rho^2 \cos^2\phi + r_z^2\right) - p_{az}\left(r_z r_\rho \sin\phi\right) \right] \\[4pt]
& \hat{z}\left[-p_{ax}r_z r_\rho \cos\phi - p_{ay}r_z r_\rho \sin\phi + p_{az}r_\rho^2 \right] \Big\}
\end{aligned}
\tag{F.8}
$$

where the $\frac{1}{\rho}$ terms have been dropped.

The source coordinates are given in Equation (C.11) of Appendix C in terms of the local variables of the V-dipole. Upon substitution the integral along the dipole leg is now seen to pertain to only a few terms. This integral represents the pattern factor of this element in the array and is given as:

$$
P^a \;=\; \int_0^A dl_a I^a(l_a) e^{j\beta u_a l_a}
\tag{F.9}
$$

where

$$
u_a \;=\; r_\rho p_{ax}\cos\phi + r_\rho p_{ay}\sin\phi + r_z p_{az}
\tag{F.10}
$$

It is recognized that this integral can be completed in closed form for a sinusoidal current. If the current is given as:

$$
I^a(l_a) \;=\; \frac{\sin\beta(A - l_a)}{\sin\beta A} \quad , \quad 0 \leq l_a \leq A
\tag{F.11}
$$

this results in a pattern factor of:

$$
P^a_{\sin} \;=\; \frac{1}{2\beta\sin\beta A}\left[e^{j\beta A}\frac{\left(e^{j\beta(u_a+1)A} - 1\right)}{(u_a + 1)} - e^{-j\beta A}\frac{\left(e^{j\beta(u_a-1)A} - 1\right)}{(u_a - 1)} \right]
\tag{F.12}
$$

147

for leg a of the dipole. The current could also be given as:

$$I_a(l_a) \;=\; \frac{\cos\beta l_a - \cos\beta A}{1 - \cos\beta A} \tag{F.13}$$

which results in a pattern factor of:

$$
\begin{aligned}
P_{\cos}^a \;=\;& \frac{1}{1-\cos\beta A}\left[\frac{\left(e^{j\beta(u_a+1)A}-1\right)}{2j\beta(u_a+1)} + \frac{\left(e^{j\beta(u_a-1)A}-1\right)}{2j\beta(u_a-1)}\right.\\
&\left. -\cos\beta A\frac{\left(e^{j\beta u_a A}-1\right)}{j\beta u_a}\right]
\end{aligned}
\tag{F.14}
$$

The pattern factors can be similarly found for leg b of the dipole taking care to be consistent with the coordinates defined in Appendix C. This results in:

$$P_{\sin}^b \;=\; \frac{1}{2\beta\sin\beta B}\left[e^{j\beta B}\frac{\left(e^{-j\beta(u_b+1)B}-1\right)}{(u_b+1)} - e^{-j\beta B}\frac{\left(e^{-j\beta(u_b-1)B}-1\right)}{(u_b-1)}\right] \tag{F.15}$$

for

$$I_b(l_b) \;=\; \frac{\sin\beta(B-l_b)}{\sin\beta B}\quad,\quad 0\le l_b \le B \tag{F.16}$$

and

$$
\begin{aligned}
P_{\cos}^b \;=\;& \frac{1}{1-\cos\beta B}\left[-\frac{\left(e^{-j\beta(u_b+1)B}-1\right)}{2j\beta(u_b+1)} - \frac{\left(e^{-j\beta(u_b-1)B}-1\right)}{2j\beta(u_b-1)}\right.\\
&\left. +\cos\beta B\frac{\left(e^{j\beta u_b B}-1\right)}{j\beta u_b}\right]
\end{aligned}
\tag{F.17}
$$

for

$$I_b(l_b) \;=\; \frac{\cos\beta l_b - \cos\beta B}{1 - \cos\beta B}\quad,\quad 0\le l_b \le B \tag{F.18}$$

where

$$u_b \;=\; r_\rho p_{bx}\cos\phi + r_\rho p_{by}\sin\phi + r_z p_{bz} \tag{F.19}$$

It is also usually convenient to put the far field into θ and ϕ components. This results in the following fields which include both leg a and leg b:

148

$$E_\theta(\overline{R}, \overline{R}') = -\frac{\eta\beta}{4D_z}\sqrt{\frac{2j}{\pi}}\sum_{n=-\infty}^{\infty}\frac{e^{-j\beta r_\rho\rho}}{\sqrt{\beta r_\rho\rho}}e^{-j\beta r_z z}e^{j\beta(r_\rho x_2\cos\phi + r_\rho y_2\sin\phi + r_z z_2)}I_0$$

$$\left(r_z\cos\theta + r_\rho\sin\theta\right)\left[P^a\left(p_{ax}r_z\cos\phi + p_{ay}r_z\sin\phi - p_{az}r_\rho\right)\right.$$

$$\left.+P^b\left(p_{bx}r_z\cos\phi + p_{by}r_z\sin\phi - p_{bz}r_\rho\right)\right] \qquad (\text{F.20})$$

and

$$E_\phi(\overline{R}, \overline{R}') = -\frac{\eta\beta}{4D_z}\sqrt{\frac{2j}{\pi}}\sum_{n=-\infty}^{\infty}\frac{e^{-j\beta r_\rho\rho}}{\sqrt{\beta r_\rho\rho}}e^{-j\beta r_z z}e^{j\beta(r_\rho x_2\cos\phi + r_\rho y_2\sin\phi + r_z z_2)}I_0$$

$$\left(r_\rho^2 + r_z^2\right)\left[P^a\left(-p_{ax}\sin\phi + p_{ay}\cos\phi\right) + P^b\left(-p_{bx}\sin\phi + p_{by}\cos\phi\right)\right]$$

$$(\text{F.21})$$

where

$$I_0 = \text{magnitude of the current} \qquad (\text{F.22})$$

$$x_2, y_2, z_2 = \text{point where the two legs are connected} \qquad (\text{F.23})$$

This still appears to involve an infinite summation but in actuality only a few, and quite often only a single term, is of interest. The first term has an exponent of $-j\beta r_\rho\rho$. This is what limits the number of terms since r_ρ is given as:

$$r_\rho = \sqrt{1 - r_z^2} \qquad (\text{F.24})$$

and

$$r_z = s_z + n\lambda/D_z \qquad (\text{F.25})$$

As n increases in magnitude, r_z becomes greater than 1 which forces r_ρ to become purely complex. This results in exponential decay as the field point moves away from the array axis. Hence there is a discrete spectrum of waves, of which only a limited number are non-evanescent.

APPENDIX G

Lumped Loads, Finite Conductivity and Insulated Wires

Lumped loads, finite conductivity of the wires, and dielectric coatings on the wires will be handled in the same manner as that used by Richmond [21]. A delta gap model will be used and hence lumped loads will simply be added to the diagonal elements of the impedance matrix.

For perfect conductors Z_s will be zero and hence the second term in Equation (2.22) will be zero. If the conductivity is finite however, the second term must be included. This term contributes when segments overlap and is given as:

$$Z'_{mn} = \frac{Z_s}{2\pi a} \int_{n \oplus m} F_m(l) F_n(l) dl \qquad (G.1)$$

where

$$Z_s = -\frac{\beta}{j\omega\epsilon} \frac{J_0(\beta a)}{J_1(\beta a)} \qquad (G.2)$$

$$\beta = \omega\sqrt{\mu_0(\epsilon - \epsilon_0)} \qquad (G.3)$$

$$\epsilon = \epsilon_0 - j\frac{\sigma}{\omega} \qquad (G.4)$$

$$\omega = 2\pi \cdot \text{frequency} \qquad (G.5)$$

$$\sigma = \text{conductivity} \qquad (G.6)$$

$$a = \text{wire radius} \qquad (G.7)$$

$$F_m(l) = \text{normalized current basis function of mode } m \qquad (G.8)$$

$$F_n(l) = \text{normalized current basis function of mode } n \qquad (G.9)$$

$$n \oplus m = \text{overlap length of modes } n \text{ and } m \qquad (\text{G.10})$$

Putting a dielectric coating onto wires in an array can be very useful as the effective length of the wire is increased and therefore elements may be packed more tightly together to alleviate grating lobe concerns. Richmond and Newman [39] used volume equivalence and a simple approximation of the field in the shell to come up with:

$$\delta Z_{mn} = -\frac{(\epsilon_2 - \epsilon) \ln(b/a)}{2\pi j \omega \epsilon \epsilon_2} \int_{n \oplus m} F_m'(l) F_n'(l) dl \qquad (\text{G.11})$$

where

$$\epsilon = \text{ambient complex permittivity} \qquad (\text{G.12})$$

$$\epsilon_2 = \text{shell complex permittivity} \qquad (\text{G.13})$$

$$b = \text{shell radius} \qquad (\text{G.14})$$

$$a = \text{wire radius} \qquad (\text{G.15})$$

$$\omega = 2\pi \cdot \text{frequency} \qquad (\text{G.16})$$

$$F_m'(l) = \text{derivative of normalized current basis function of mode } m \qquad (\text{G.17})$$

$$F_n'(l) = \text{derivative of normalized current basis function of mode } n \qquad (\text{G.18})$$

$$n \oplus m = \text{overlap length of modes } n \text{ and } m \qquad (\text{G.19})$$

It should be noted that the thin wire approximations of constant surface currents on the wire and constant radial electric field in the shell as functions of phi are inherent in the above equation. Therefore care should be taken to insure that both of these constraints are approximately true, i.e., the coating cannot be made arbitrarily fat and elements that are sharply bent or are in close proximity to other elements are suspect.

For a piecewise sinusoidal basis function given on leg a by:

$$F(l) = \begin{cases} \dfrac{\sin \beta(A-l)}{\sin \beta A} & 0 \le l \le A \\[2mm] \quad\text{— or —} \\[2mm] \dfrac{\sin \beta l}{\sin \beta A} & 0 \le l \le A \end{cases} \qquad (G.20)$$

the above integrals can be completed in closed form. For self terms and those that overlap and have terminals at the same end of a mode:

$$\int_0^A F_m(l)F_m(l)dl = \frac{2\beta A - \sin 2\beta A}{4\beta \sin^2 \beta A} \qquad (G.21)$$

$$\int_0^A F'_m(l)F'_m(l)dl = \frac{\beta}{4\sin^2 \beta A}\left(2\beta A + \sin 2\beta A\right) \qquad (G.22)$$

For overlapping elements with terminals at opposite ends of the segment:

$$\int_0^A F_m(l)F_n(l)dl = \frac{-\beta A \cos \beta A + \sin \beta A}{2\beta \sin^2 \beta A} \qquad (G.23)$$

$$\int_0^A F'_m(l)F'_n(l)dl = \frac{-\beta}{2\sin^2 \beta A}\left(\beta A \cos \beta A + \sin \beta A\right) \qquad (G.24)$$

Therefore as seen above, lumped loads, finite conductivity and insulated wires only arise in the calculation of self impedances and those of overlapping elements.

APPENDIX H

Shanks Transform

The Shanks transform [31] is a non-linear sequence to sequence transformation that will be used here to accelerate the convergence of the impedance element summations in the spatial domain. The transform is defined as follows. Given a sequence of numbers or function $\{A_n\}(n = 0, 1, 2, \ldots)$ let:

$$\Delta A_n = A_{n+1} - A_n \tag{H.1}$$

From this sequence a new sequence will be derived. If k is a positive integer, define the kth order transform of $\{A_n\}$ as $\{B_{k,n}\}(n = k, k+1, k+2, \ldots)$ such that:

$$B_{k,n} = \frac{\begin{vmatrix} A_{n-k} & \cdots & A_{n-1} & A_n \\ \Delta A_{n-k} & \cdots & \Delta A_{n-1} & \Delta A_n \\ \Delta A_{n-k+1} & \cdots & \Delta A_n & \Delta A_{n+1} \\ \vdots & & \vdots & \\ \Delta A_{n-1} & \cdots & & \Delta A_{n+k-1} \end{vmatrix}}{\begin{vmatrix} 1 & \cdots & 1 & 1 \\ \Delta A_{n-k} & \cdots & \Delta A_{n-1} & \Delta A_n \\ \Delta A_{n-k+1} & \cdots & \Delta A_n & \Delta A_{n+1} \\ \vdots & & \vdots & \vdots \\ \Delta A_{n-1} & \cdots & & \Delta A_{n+k-1} \end{vmatrix}} \tag{H.2}$$

153

for each n for which the denominator does not vanish. Of particular interest is the $k = 1$ case which reduces to:

$$B_{1,n} = \frac{\begin{vmatrix} A_{n-1} & A_n \\ \Delta A_{n-1} & \Delta A_n \end{vmatrix}}{\begin{vmatrix} 1 & 1 \\ \Delta A_{n-1} & \Delta A_n \end{vmatrix}} = \frac{A_{n+1}A_{n-1} - A_n^2}{A_{n+1} + A_{n-1} - 2A_n} \qquad (H.3)$$

By applying the first order transform a new sequence is generated in which each element is a function of three elements in the original sequence. The new sequence has been formed such that it will converge more rapidly. This process can now be repeated on the second sequence and the new third sequence will converge faster still. This process is repeated until the desired degree of stability is reached.

Shanks [31] offers a proof showing that if the original sequence can be expressed as a summation with the summand being a ratio of polynomials, then each successive transformed sequence converges more rapidly than its predecessor to the same limit. The summand of interest here for calculating the mutual impedance is not given as a ratio of polynomials so there is not a guarantee of success. Experimentation with the first order transform has demonstrated that it is very useful when doing the summation in the spatial domain but of little consequence when summing in the spectral domain. This did not prove to be significant in the final program as the spectral domain solution is used only in the cases where the summation converges quite rapidly without being accelerated.

To show how the transform performs the acceleration Shanks [31] offers a "heuristic motivation of the transforms" section in his paper. In it he has a figure showing several graphs of transients either converging or diverging in a monotonic or oscillatory fashion. Each sequence can be considered to be k^{th} order transient locally; that is if you consider k terms to either side of A_n, A_n can be approximated

154

by a constant and a summation of exponentials

$$A_n \approx A_r = B_{k,n} + \sum_{i=1}^{k} a_{i,n} e^{\alpha_{i,n} r} \qquad (\alpha_{i,n} \neq 0)$$

$$(n - k \leq r \leq n + k) \qquad (n \geq k) \qquad \text{(H.4)}$$

We are interested in the constant part, $B_{k,n}$, which approximates the final converged solution. The mechanics of the transform are that $2k + 1$ points are taken and an approximate solution is found, then the $2k + 1$ point window is moved a point and another approximation is made. The approximations now form a new sequence which will hopefully converge much more rapidly than the original sequence. As stated above, the transform is also applied to the new sequence once it has $2k + 1$ points and if the convergence is still not to the desired goal it is applied to that sequence and so forth.

As a demonstration of its usefulness the mutual impedance between two arrays of $\hat{z}$ directed straight dipoles is calculated in the spatial domain using a straight summation and applying the Shanks transform. The dipoles are a half wavelength long and spaced three wavelengths apart as shown in Figure 81. Figure 82 is a plot of the straight summation terms in the complex plane. The convergence criteria has been set to .0005% to obtain a fairly high degree of accuracy. A total of 499 terms were calculated using 5.75 cpu seconds. It is seen visually that the last digit of accuracy is not only requiring a large number of terms but could be estimated long before the summation runs its course.

The effect of the Shanks transform is more readily seen when plotting the real and imaginary parts separately versus the summation index as in Figure 83 and 84. Using the Shanks transformation the same degree of accuracy is obtained using only the first 11 terms in the summation in 0.11 cpu seconds! The increase in accuracy with each level of transform is shown separately for each level in Figures 83 and 84.
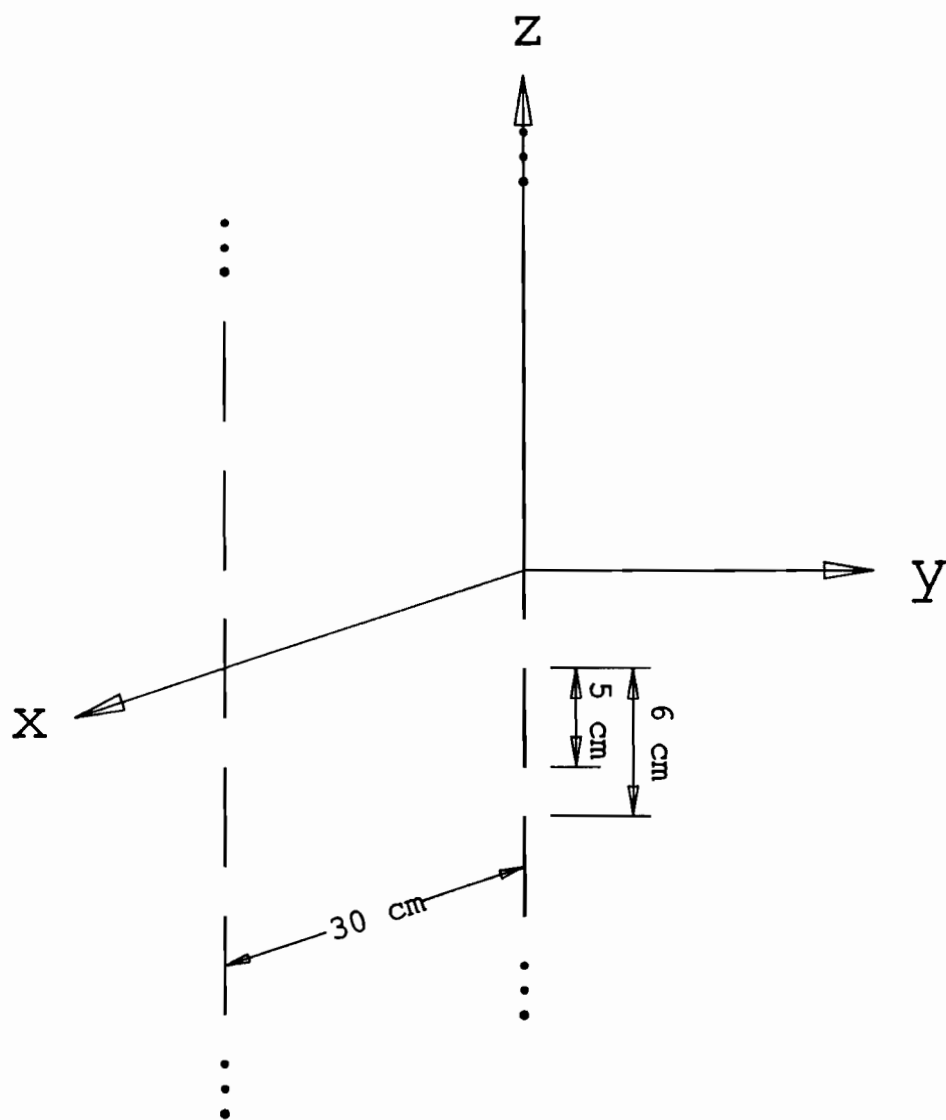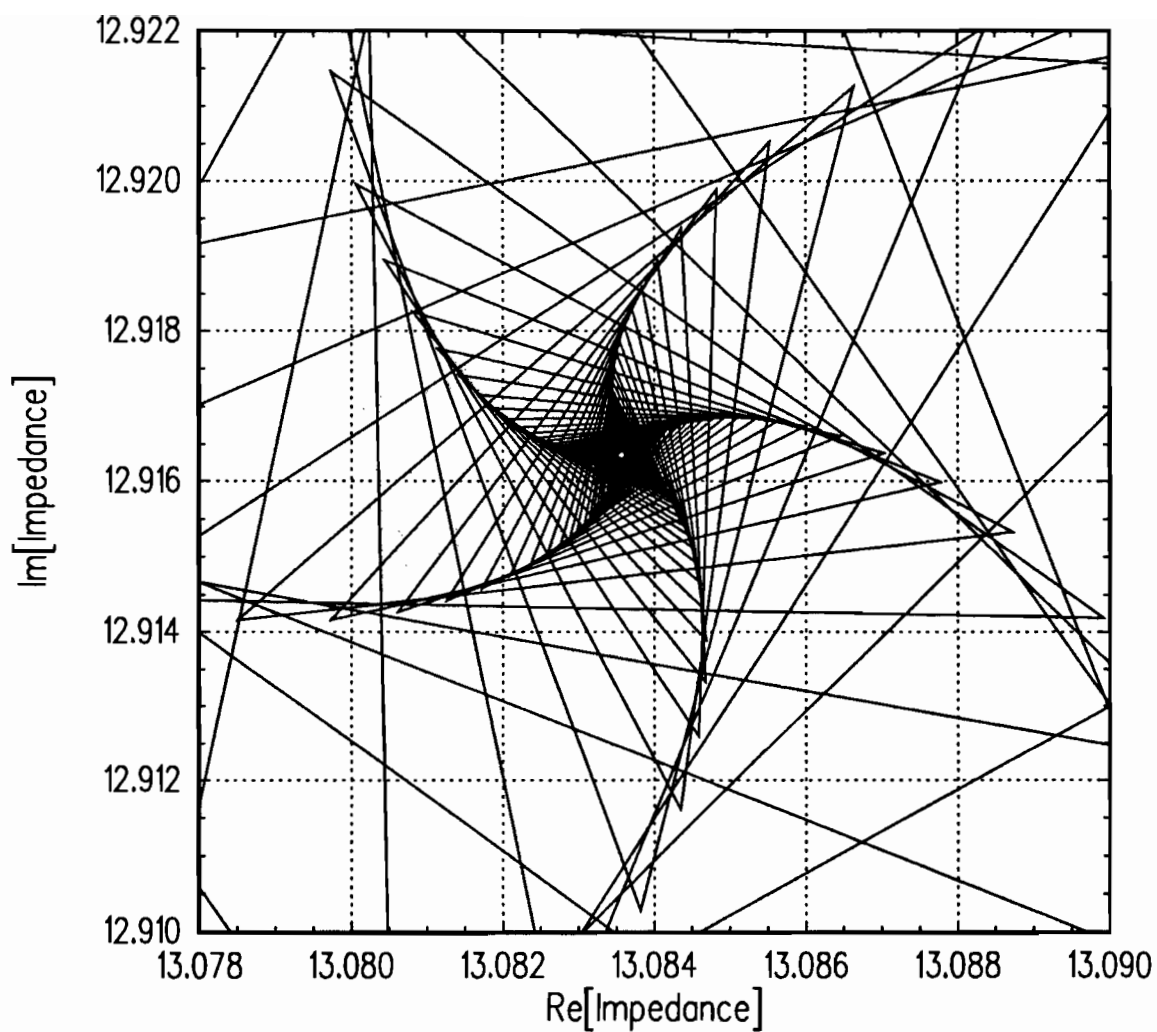
155

Figure 81: Two columns of axially oriented straight dipoles spaced three wavelengths apart at 3.0 GHz.

Figure 82: Convergence of the mutual impedance between two straight axially oriented dipole columns using straight summation in the spatial domain.
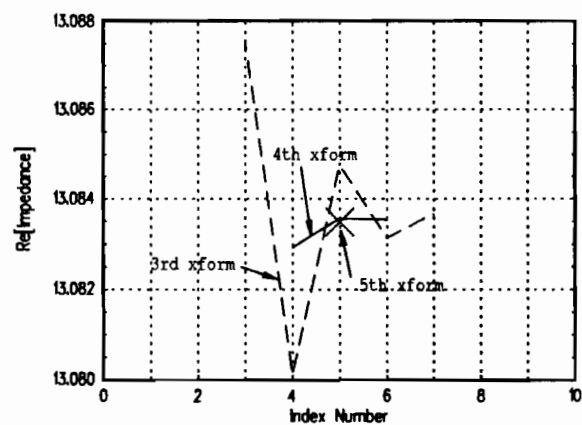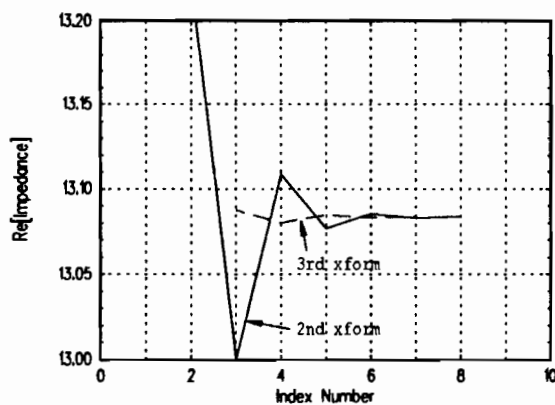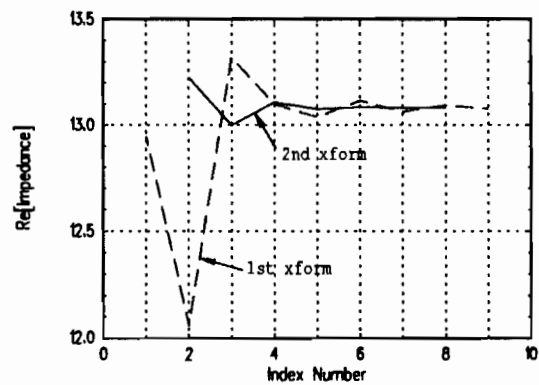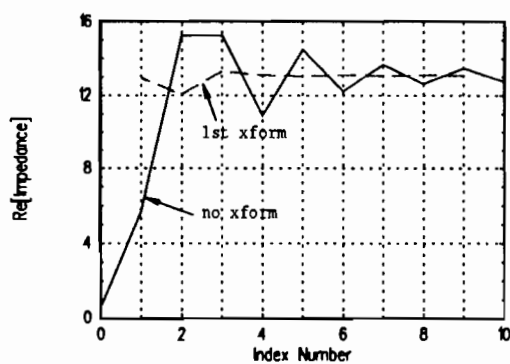
Figure 83: Convergence of the real part of the mutual impedance between two straight axially oriented dipole columns utilizing the Shanks transform in the spatial domain.
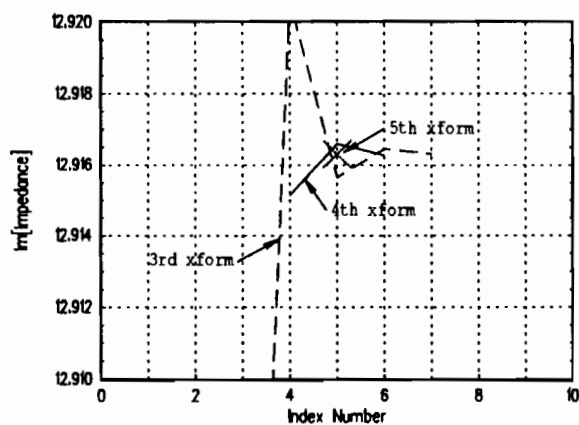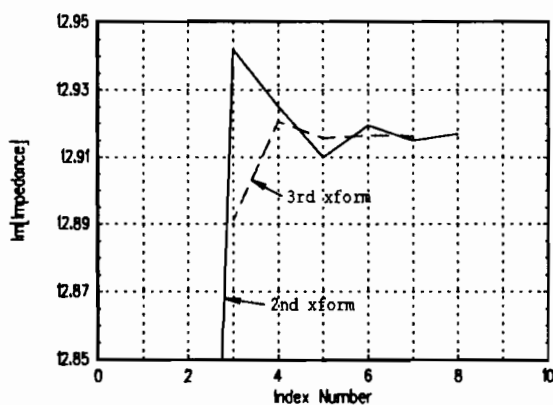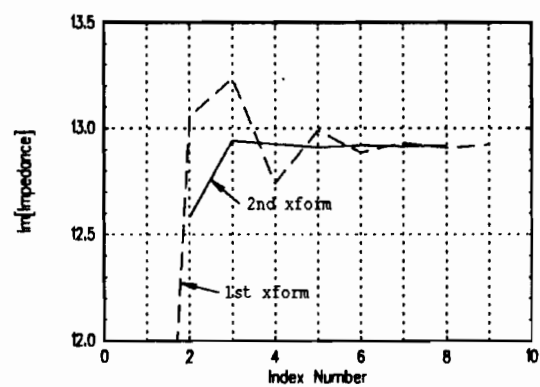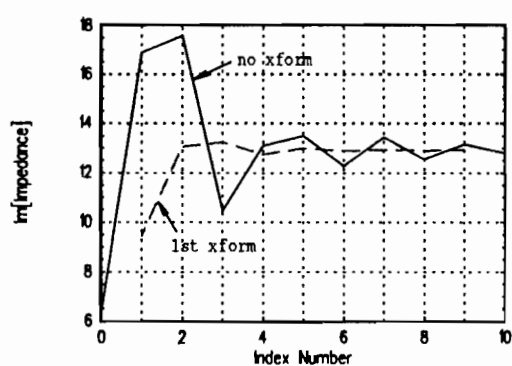
158

Figure 84: Convergence of the imaginary part of the mutual impedance between two straight axially oriented dipole columns utilizing the Shanks transform in the spatial domain.

159

The plot in the upper left hand corner shows the first eleven terms of the summation and the resulting nine terms of a first order transform. The transformed series has a much smaller degree of oscillation. The plot in the upper right shows the nine terms of the first transform and the resulting seven terms of a second transform. The lower left plot shows the seven terms of the second transform and the resulting five terms of a third transform. The lower right plot shows the five terms of the third transform, the resulting three terms of the fourth transform and the last term resulting from a fifth transform. In each case, the transformed series is seen to converge faster than its predecessor.

The spectral domain solution converged immediately for the above geometry however the solution in the spectral domain requires that both the inner and outer integrals be done numerically. For the same degree of accuracy, two terms were calculated (the second one to verify convergence) using .30 cpu seconds, making the spectral approach slower for this case than the spatial domain with the Shanks transform applied.

It should also be noted that the program does not look for special cases such as straight z directed dipoles which greatly simplifies the calculation of the impedance. The spectral domain calculation could be greatly accelerated if advantage were taken of those cases. The programs HOSER [11] and TRANSCAT [15] were written specifically for straight equal leg length dipoles that are either z directed (HOSER) or lie in the x-y plane (TRANSCAT) and should be faster at running these specialized cases.

There has been interest in the Shanks transform in the literature lately [40] and also in a transform by Wynn [41]. The Wynn transform is very similar to the Shanks transform, however I did not find it to be very effective for the problem at hand in either the spectral or spatial domains.

BIBLIOGRAPHY

[1] B. A. Munk, "Reflection from a monoplanar single-tuned periodic surface," Report 2382-9, ElectroScience Laboratory, The Ohio State University, Columbus, OH 43212, October 1968. Prepared under contract F33615-67-C-1507 for the Air Force Avionics Laboratory, Wright Patterson Air Force Base, Ohio.

[2] B. A. Munk, R. G. Kouyoumjian, and L. Peters, "Reflection properties of periodic surfaces of loaded dipoles," *IEEE Trans. Antennas Propagat.*, vol. 19, pp. 612–617, September 1971.

[3] B. A. Munk and R. J. Luebbers, "Reflecton properties of two layer dipole arrays," *IEEE Trans. Antennas Propagat.*, vol. 22, pp. 766–773, November 1974.

[4] B. A. Munk, R. J. Luebbers, and R. D. Fulton, "Transmission through a two layer array of loaded slots," *IEEE Trans. Antennas Propagat.*, vol. 22, pp. 804–809, November 1974.

[5] R. J. Luebbers and B. A. Munk, "Reflection from n-layer dipole array," Report 2989-12, ElectroScience Laboratory, The Ohio State University, Columbus, OH 43212, July 1973. Prepared under contract F33615-70-C-1439 for the Air Force Avionics Laboratory, Wright Patterson Air Force Base, Ohio.

[6] B. A. Munk, R. J. Luebbers, and T. L. Oliver, "Impedance of dipole arrays in various dielectric slab configurations," Report 2989-5, ElectroScience Laboratory, The Ohio State University, Columbus, OH 43212, September 1972. Prepared under contract F33615-70-C-1439 for the Air Force Avionics Laboratory, Wright Patterson Air Force Base, Ohio.

[7] B. A. Munk, G. A. Burrel, and T. W. Kornbau, "A general theory of periodic surfaces in stratefied dielectric media," Report 784346-1, ElectroScience Laboratory, The Ohio State University, Columbus, OH, November 1977. Prepared under contract F33615-76-C-1024 for Aeronautical Systems Division, Wright-Patterson Air Force Base.

[8] B. A. Munk, "A general theory of periodic surfaces in a stratefied dielectric medium," Report 715582-4, ElectroScience Laboratory, The Ohio State University, Columbus, OH, February 1986. Prepared under contract F33615-83-C-1013 for Aeronautical Systems Division, Wright-Patterson Air Force Base.

[9] L. W. Henderson, *The Scattering of Planar Arrays of Arbitrary Shaped Slot and/or Wire Elements in a Stratefied Dielectric Medium.* Ph.D. dissertation, The Ohio State University, Columbus, OH 43210, 1983.

[10] L. W. Henderson, "Introduction to PMM," Report 715582-5, ElectroScience Laboratory, The Ohio State University, Columbus, OH 43212, February 1986. Prepared under contract F33615-83-C-1013 for the Avionics Laboratories (AFWAL/AAWP-3), Wright-Patterson Air Force Base, OH 45433.

[11] J. A. Hughes, "Impedance properties of cylindrical arrays and finite planar arrays," Master's thesis, The Ohio State University, Columbus, OH 43210, 1988.

[12] J. A. Hughes, "FLAT.FOR program." The Ohio State University ElectroScience Laboratory Software, January 1988.

[13] J. I. Simon, *Impedance Properties of Periodic Linear Arrays Conformal to a Dielectric-Clad Infinite PEC Cylinder*. Ph.D. dissertation, The Ohio State University, Columbus, OH 43210, 1989.

[14] K. A. Strickler, "Impedance properties of singly infinite periodic surfaces composed of axially oriented dipoles," Master's thesis, The Ohio State University, Columbus, OH 43210, 1989.

[15] J. P. Skinner, *Scattering from a Finite Collection of Transverse Dipole and Axial Slot Arrays with Edge Effects*. Ph.D. dissertation, The Ohio State University, Columbus, OH 43210, 1991.

[16] R. Mittra, C. H. Chan, and T. Cwik, "Techniques for analyzing frequency selective surfaces - a review," *Proceedings of the IEEE*, vol. 76, no. 12, pp. 1593–1615, 1988.

[17] T. Cwik, R. Mittra, K. C. Lang, and T. K. Wu, "Frequency selective screens," *IEEE Antenna and Propagation Society Newsletter*, pp. 6–10, April 1987.

[18] T. Cwik and R. Mittra, "The effects of the truncation and curvature of periodic surfaces: A strip grating," *IEEE Trans. Antennas Propagat.*, vol. 36, no. 5, pp. 612–622, 1988.

[19] E. K. English, *Electromagnetic Scattering from Infinite Periodic Arrays of Arbitrarily Otiented Dipole Elements Imbedded in a General Stratefied Medium*. Ph.D. dissertation, The Ohio State University, Columbus, OH 43210, 1983.

[20] S. J. Lin, *On the Scan Impedance of an Array of V-dipoles and the Effect of the Feedlines*. Ph.D. dissertation, The Ohio State University, Columbus, OH 43210, 1985.

[21] J. H. Richmond, "Radiation and scattering by thin-wire structures in the complex frequency domain," Report 2902-10, ElectroScience Laboratory, The Ohio State University, Columbus, OH, July 1973. Prepared under contract NGL 36-008-138 for NASA Langley Research Center.

[22] J. H. Richmond, "Computer program for thin-wire structures in a homogeneous conducting medium," Report 2902-12, ElectroScience Laboratory, The Ohio State University, Columbus, OH, August 1973. Prepared under contract NGL 36-008-138 for NASA Langley Research Center.

[23] C. Huygens, *Treatise on Light*. New York: Dover Publications, 1962. Originally published in 1661.

[24] G. Floquet, "Equations differentielles lineaires, a coefficients periodiques," *Annale Ecole Normale Superieur*, pp. 47–88, 1883.

[25] S. A. Schelkunoff, "On diffraction and radiation of electromagnetic waves," *Physical Review*, vol. 56, pp. 1483–1491, August 15 1939.

[26] V. H. Rumsey, "Reaction concept in electromagnetic theory," *Physical Review*, vol. 94, pp. 1483–1491, June 15 1954.

[27] E. H. Newman, "Ee814 course notes." Ohio State University course on the Moment Method, 1991.

[28] S. A. Schelkunoff and H. T. Friis, *Antenna Theory and Practice*. New York: J. Wiley and Sons, 1952.

[29] H. E. Pocklington, "Electrical oscillations in wires," *Proceedings of the Cambridge Philosophical Society*, vol. 9, pp. 324–332, October 1897.

[30] S. A. Schelkunoff, *Electromagnetic Waves*. New York: D. Van Nostrand Company, 1943.

[31] D. Shanks, "Non-linear transformations of divergent and slowly converging sequences," *Journal of Mathematics and Physics*, vol. 34, pp. 1–42, 1955.

[32] P. Wynn, "On a Procrustean technique for the numerical transformation of slowly convergent sequences and series," *Proceedings of the Cambridge Philosophical Society*, vol. 52, pp. 663–671, 1956.

[33] S. Singh and R. Singh, "On the use of ρ-algorithm in series acceleration," *IEEE Trans. Antennas Propagat.*, vol. 39, pp. 1514–1517, October 1991.

[34] G. A. Burrel and B. A. Munk, "Plane wave expansion for arrays of arbitrarily oriented piecewise linear elements and its application in determining the impedance of a single linear antenna in a lossy half-space," *IEEE Trans. Antennas Propagat.*, vol. 27, pp. 331–343, May 1979.

[35] G. A. Burrel and B. A. Munk, "The array scanning method and applying it to determine the impedance of linear antennas in a lossy half space," Report 4460-1, ElectroScience Laboratory, The Ohio State University, Columbus, OH 43212, October 1976. Prepared under contract DAAG53-76-C-0179 for the US Army Mobility Equipment Research and Development Command, Ft. Belvoir, VA 22060.

[36] F. A. Sikta, *UTD Analysis of Electromagnetic Scattering by Flat Plate Structures*. Ph.D. dissertation, The Ohio State University, Columbus, OH 43210, 1981.

[37] J. D. Kraus, *Electromagnetics*. McGraw-Hill Electrical and Electronic Engineering Series, New York: McGraw-Hill, 1992. Pages 556–569 (Figure 12-56f in particular).

[38] R. F. Harrington, *Time-harmonic Electromagnetic Fields*. McGraw-Hill Electrical and Electronic Engineering Series, New York: McGraw-Hill, 1961.

[39] J. Richmond and E. Newman, "Dielectric coated wire antennas," *Radio Science*, vol. 11, pp. 13–20, January 1976.

[40] S. Singh and R. Singh, "Efficient computation of the free-space periodic Green's function," *IEEE Trans. Microwave Theory Tech.*, vol. 39, pp. 1226–1229, July 1991.

[41] S. Singh, W. F. Richards, J. R. Zinecker, and D. R. Wilton, "Accelerating the convergence of series representing the free space periodic Green's function," *IEEE Trans. Antennas Propagat.*, vol. 38, pp. 1958–1962, December 1990.